Antiferromagnetic properties of 3d transition metal oxide nanoparticles

University of Basel

Inauguraldissertation

zur

Erlangung der Würde eines Doktors der Philosophie

vorgelegt der

Philosophisch-Naturwissenschaftlichen Fakultät

der Universität Basel

von

David Bracher

Rüegsau BE, Schweiz

2021

Genehmigt von der Philosophisch-Naturwissenschaftlichen Fakultät auf Antrag von

Prof. Dr. Martino Poggio
Fakulttsverantwortlicher

Prof. Dr. Peddis
Korreferent

Basel, den 17.12.2019

Prof. Dr. Martin Spiess
Dekan

Abstract

Antiferromagnetic (AFM) materials have attracted significant attention in the past years due to emerging fields such as antiferromagnetic spintronics, the development of ultrafast switching magnetic random access memory devices, spin valves, and new ultrahard magnetic materials. In order to scale down such new devices for its technological implementation a fundamental understanding of antiferromagnetism at the nanoscale is of crucial interest. While antiferromagnetic materials have been widely investigated in their respective bulk and thin film forms, only very few attempts were made to understand nanoscaled antiferromagnets. This is mostly due to the fact that probing magnetism of thin films and at the nanoscale usually utilized magnetic stray fields which do not appear in nano-sized antiferromagnetic materials. Although there have been some studies of the antiferromagnetic properties of nanoparticles by means of magnetometry, Mössbauer spectroscopy, neutron scattering etc. Those methods usually integrate over large ensembles of nanoparticles making it very challenging to disentangle effects of sizes and shapes distributions as well as the chemical composition. Further, in typical powder measurements it is extremely challenging to directly separate the influence of intrinsic magnetic properties and eventual magnetic inter-particle interactions.

In this thesis, this issue is overcome using x-ray photoemission electron microscopy utilizing the x-ray magnetic linear dichroism effect. This effect allows one to directly probe the magnetic ordering parameter of a antiferromagnetic material exploiting the fact that linearly polarized x-ray within a antiferromagnetic media show an orientation dependent absorption. Further, scanning electron microscopy is used to investigate the morphology of individual nanoparticles and small agglomerates. In order to be able to correlate the morphology and the chemical and magnetic properties of the nanoparticles, samples with a very low surface concentration on silicon substrates are produced. Since the sil-

icon substrates contain unique gold marker structures it is possible to identify the very same nanoparticles and agglomerates in complementary microscopy measurements. This thesis addresses the magnetic properties of acicular goethite ($\alpha - \mathrm{FeOOH}$) nanoparticles and $\mathrm{CoO}/\mathrm{Co_3O_4}$ core-shell nanooctahedra. In case of the $\mathrm{CoO}/\mathrm{Co_3O_4}$ nanoparticles the emergence of possible uncompensated magnetic surface/interface moments are investigated using the x-ray magnetic circular dichroic effect which directly probes the direction of the magnetic moments.

It is found that the antiferromagnetic spin axis of individual goethite nanoparticle have a tendency to be oriented out of the sample plane. This behavior suggests that an interface effect with the non-magnetic substrate influences the magnetic properties of the goethite nanoparticles.

In case of the $\mathrm{Co_3O_4}/\mathrm{CoO}$ core-shell nanooctahedra it is demonstrated that antiferromagnetic spin axis can be determined without any prior knowledge about the crystal directions. The axis are found to align closely to the crystal direction, as it would be expected for CoO in its bulk form. Additionally, indications for uncompensated magnetic moments are detected. The magnetic moments are found to behave superparamagnetically down to 100 K. Such superparamagnetic behavior is not found for the antiferromagnetic CoO core. Although, it is possible that the antiferromagnetic order in the core can switch its sublattice magnetization by 180 ° which can intrisically not be observed by studying the x-ray magnetic linear dichroism.

Acknowledgments

Dr. Armin Kleibert	I am grateful his supervision, where it was necessary, and for the numerous scientific discussions. Overall Armin's supervision as well as the dealt freedom helped me to advance as a scientist and hopefully also as a person.
Prof. Dr. Martino Poggio	Thanks for your support and always having an open ear if it was useful to me and my work.
SNI PhD School	It was a great opportunity to be a part of the SNI PhD School. I very much enjoyed all the meetings which give an outstanding possibility to talk and exchange with other PhD students.
SNI	For the funding of my project (SNI P1502). Obviously doing science without the necessary financial support would not be impossible.
Dr. Carlos A. F Vaz	I really appreciated your willingness to help when it was needed. Further I deeply appreciated the at the time very challenging scientific questions you posed which always helped me to make my understanding of magnetism more solid. Further, his proof reading and inputs were greatly appreciated.
Magnetism and Microscopy Group	For letting me feel very welcome. The group was a outstanding and supportive environment to do science. A special thank to Dr. Urs Staub, Dr. Cinthia Piamonteze, and Jan Dreiser for their great an critical question during presentations in group seminars and their advice, which always was very helpful and deeply appreciated.
Dr. Manuel Langer and Dr. Max Burian	Many thanks for proof reading my thesis and giving last valuable inputs.

Poggio Lab	I really appreciated how welcome you made me feel when I was around. Unfortunately I missed the chance to get in better contact.
Dr. Marcus Wyss	I really enjoyed the work with your and was always very grateful for your support and advice.
Dr. Tatiana Savchenko	I was very lucky to have someone which always supported me during beamtimes. Also the time on numerous conferences was very enjoyable.
Martín Testa Anta	For providing me with the outstanding CoO nanooctahedra and many scientific discussion. But even more for joining me for beamtimes and in the end of the thesis writing to stand my episodes of upcoming madness. And most importantly for not only being a outstanding co-worker and collaborator but also a friend.
Prof. Dr. Verónica Salgueiriño	For her very spontaneous willingness in the beginning of the CoO nanoparticles project to collaborate. Also the nice scientific and sometimes perhaps not so scientific discussion when we met at ICFPM 2019.
Dr. Shridar Avula, Dr. José Mardegan, and Nazaret Ortiz Hernandez	For being very good colleagues but even more important great friends. Anything is easier with friends around. And specially Shridar for the awesome times at various conference, my conference buddy.
Dr. Thilo Glatzel	For his supervision during my Master thesis which likely caused me wanting to peruse science.

My Family	My mom, dad, brother, my brothers girl friend, and their family for the support and encouragement during all my scientific endeavors.
Friends	Last but not least all my friends which also took part in this journey.

List of abbreviations

AC	Alternating current
$BiFeO_3$ or BFO	Bismuth ferrite
c	Speed of light, $2.998 \cdot 10^8$ m s^{-1}
C2/m	Monoclinic space group
CCD	Charge-coupled device
Co	Cobalt
Co_3O_4	Spinel cobalt oxide
CoO	Rocksalt cobalt oxide
DC	Direct current
DFT	Density functional theory
DLS	Dynamic light scattering
E	Electronic field vector
EELS	Electron energy loss spectroscopy
ESR	Electron spin relaxation spectroscopy
Fe	Iron
Fe_3O_4	Magnetite
Fm3m	Cubic space group
k	X-ray propagation vector
K	Magnetocrystalline anisotropy
κ	Shape factor
k_B	Boltzmann constant, $1.38 \cdot 10^{-23}$ J K^{-1}
$LaFeO_3$	Lanthanum ferrite
MCP	Multi channel plate
Ni	Nickel

NiO	Nickel oxide
NP	Nanoparticle
NV	Nitrogen vacancy
O_h	Octahedrally coordinated atom
$P6_3mc$	Hexagonal space group
$Pnma$	Orthorhombic space group
$\mathbf{q}$	Scattering vector
RHEED	Reflection high energy electron diffraction
SEM	Scanning electron microscopy
SIM	Surface/Interface: ddMicroscopy beamline (X11MA)
SiO_x	Silicon substrate with native oxide layer
SLS	Swiss Light Source
SQUID	Superconducting quantum interference device
STXM	Scanning transmission x-ray microscopy
T_C	Curie temperature
T_N	Néel temperature
T_d	Tetrahedrally coordinated atom
TEM	Transmission electron microscopy
UHV	Ultra-high vacuum
W	Tungsten
$w - CoO$	Wurtzite cobalt oxide
XAS, XA spectroscopy	X-ray absorption spectroscopy
XLD	X-ray linear dichroism
XMCD	X-ray magnetic circular dichroism
XMLD	X-ray magnetic linear dichroism
XNLD	X-ray natural linear dichroism
XPEEM	X-ray photoemission electron microscopy
XPS	X-ray photoelectron spectroscopy
XRD	X-ray diffraction
$\alpha - Fe_2O_3$	Hematite
$\alpha - FeOOH$	Goethite

Contents

Chapter 1

Introduction

Since its discovery antiferromagnetism was rather perceived as "interesting but useless" as Louis Néel expressed quite explicitly in his Nobel Lecture [1]. However, this view had to be changed with magnetic storage based on exchange bias systems where the antiferromagnetic material acts as a passive layer. Moreover, in the last few years antiferromagnetic materials attracted significant attention due to their applicability to antiferromagnetic spintronics [2–8] and the development of spin valves [9, 10], magnetic storage media [11–13], magnetic random access memory devices [8, 14], and a new generation of ultrahard magnetic materials. In such applications antiferromagnetic materials are expected to serve as the main components in devices as opposed to the passive role in exchange bias systems. Recently it was found that antiferromagnetic thin films can be switched by applying laser pulses [15] and voltage pulses [8]. Further antiferromagnetic materials have been demonstrated to possess the potential to show very fast switching up to the terrahertz range [12, 15, 16]. Switching characteristics in that frequency range might pave the way in the future for computing performances not achievable today. While the magnetic properties of many antiferromagnetic oxides such as NiO [10, 17–21], Fe_3O_4 [22–25], $\alpha - Fe_2O_3$ [26, 27], CoO [28–31], $LaFeO_3$ [32–42], $BiFeO_3$ [43–46] in their bulk or thin film form have been well established, the magnetic properties of antiferromagnetic materials at the nanoscale are still poorly understood. However, the miniaturization of potential antiferromagnetic devices will demand a profound understanding of phenomena arising from the nanoscale size of the devices. It would be interesting to study the potential arising of a single domain limit and superparamagnetic relaxation [47] in antiferromagnetic mater-

ials and the physical mechanism behind. The single domain limit in ferromagnets arises due to the competition of the minimization of the magnetostatic energy and the energy, which is needed to break the spin orientation preferred by the exchange coupling. In a compensated antiferromagnet the magnetostatic energy vanishes and thus the mechanism of the antiferromagnetic domain formation is still an open question [48, 49]. Usually it is expected that magnetoelastic contribution play a crucial role. Concerning a single domain limit one could speculate that an antiferromagnetic nanoparticle has to exhibit a single domain state if the size of the nanoparticle is smaller than the size of a domain wall. For example in NiO single crystals the domain wall width has been determined to be around 150 nm [50]. In contrast it has been found that the domain walls of an antiferromagnetically coupled Fe monolayer on W(001) can be as narrow as 6-8 atomic rows [51]. This suggests that the dimensionality of a system might have an influence on the domain wall size in antiferromagnets. First theoretical steps in order to understand superparamagnetism in antiferromagnets have been taken and it was found that the switching frequency is enhanced and thus the thermal stability significantly decreased compared to their ferromagnetic counterparts [16]. The use of synthetic chemistry allows to control many nanoparticle parameters, such as chemical composition, shape, monodispersity [52–58]. Moreover, it is now possible to produce hollow or core-shell nanoparticles systems. The latter might even make nanoscale artificial multiferroics systems accessible [52, 53, 59–62]. Multiferroics are materials, which exhibit coupled magnetic and ferroelectric ordering parameters. This potentially to manipulate the magnetic properties directly by applying electric fields and vice versa. There are intrinsic multiferroic (e.g. $BiFeO_3$) and artificial multiferroic systems (Co/PMNPT). Using nanoparticles with a core-shell morphology could allow to access artificial multiferroics for example by growing a magnetic material on a ferroelectric core.

Antiferromagnetic nanoparticles were widely investigated. AC and DC magnetometry [52, 63, 64] yield the dynamic and static susceptibility. Mössbauer spectroscopy [65–69] reveals the fine structure splitting. Electron spin resonance spectroscopy [70] can directly access information about unpaired electrons. Neutron scattering [71, 72] and muon spin relaxation [73] provide information of the local magnetic fields in a solid state object at the atomic scale. However, those methods measure the averaged magnetic properties of

a large ensemble of nanoparticles which are composed of a certain distribution of properties like the size, shape, chemical composition, and crystallinity. Thus, the influence of microstructural defects such as antiphase boundaries, stacking faults, and point defects on the magnetic properties are still widely unexplored. The effect of antiphase boundaries in magnetite nanoparticles was investigated by correlating DC magnetometry data of ferrimagnetic magnetite nanoparticles with high resolution transmission electron micrographs [74]. Such studies are helpful but are still not able to directly correlate the relation between the magnetic properties of individual nanoparticles and their respective morphology or microstructure.

It is very challenging to disentangle the contribution of inter-particle interactions from the intrinsic magnetic properties of individual nanoparticles, such as magnetic ordering temperature, blocking temperature, the orientation of the spin axis, and uncompensated magnetic moments originating from the small size of the nanoparticles. In order to access the intrinsic magnetic properties of antiferromagnetic nanoparticles, those have to be probed on the level of individual nanoparticles. It would certainly be possible to study the magnetic properties of individual ferro- and ferrimagnetic nanoparticles by means of magnetic force microscopy (MFM) or scanning NV-magnetometry. However, those methods rely on measuring stray fields and further need extensive modeling to retrieve the magnetic ordering direction of individual nanoparticles. Further, it is not clear if the magnetic properties of a 3D object can be properly assessed since those methods are usually very accurate in order to investigate atomically flat thin films but are less reliable for systems with a strong topography, such as many nanoparticle systems have. However, the major challenge for investigations of antiferromagnetic nanoparticles by means of MFM and scanning nitrogen vacancy magnetometry is the absence of a macroscopic stray field. Thus, antiferromagnetic nanoparticles can only be studied by assessing the antiferromagnetic ordering parameter directly.

In this thesis the magnetic properties of individual and agglomerated antiferromagnetic nanoparticles are studied using a methodology which was used similarly for ferromagnetic nanoparticles [75]. Specifically x-ray photoemission electron microscopy (XPEEM) is combined with complementary scanning electron microscopy (SEM) on highly diluted nanoparticle samples. The combination of highly diluted nanoparticles and the use of

gold marker structures on the silicon substrates allows us to identify the very same nanoparticles in both microscopes [76–79]. Hereby, the chemical properties of the nanoparticles are studied using x-ray absorption spectromicroscopy. The antiferromagnetic properties and eventual uncompensated magnetic moments are observed utilizing the x-ray magnetic linear (XMLD) and circular (XMCD) dichroic effects using linearly and circularly polarized x-rays, respectively. Those effects arise from polarization dependent x-ray absorptions at the $L_{2,3}$ edges of $3d$ transition metal oxides [18, 19, 31, 80–84]. Whereas the XMLD is sensitive to the orientation of the spin axis with respect to the polarization vector of the x-rays, the XMCD effect indicates the relation between the propagation direction of the x-rays and the magnetic moments.

So far antiferromagnetic nanoparticles were typically investigated in form of powder samples. In order to obtain an acceptable signal to noise ratio for nanoparticles on a substrate, the nanoparticles have to be stacked in thick multilayer samples. However, for applications such systems are not well suited since in this case self-assembled monolayers or individual nanoparticles might be favorable. In those systems the interaction between the nanoparticles and the substrate might become very important since the substrate-particle interactions profoundly affect the orientation of the antiferromagnetic spin axis of individual antiferromagnetic nanoparticles. The approach used in this thesis allows investigating individual nanoparticles and their agglomerates, which form islands of quasi-monolayers on the substrates. The reason for this is that drop casting antiferromagnetic nanoparticles from highly diluted solutions always yield individual and agglomerated nanoparticles. Thus, it becomes possible to investigate the importance of interface effects on antiferromagnetic nanoparticles.

Firstly, goethite ($\alpha - \mathrm{FeOOH}$) nanoparticles are investigated using scanning electron microscopy (SEM), transmission electron microscopy (TEM), x-ray diffraction (XRD), reflection high energy electron diffraction (RHEED), x-ray absorption (XA) spectroscopy, and x-ray linear dichroism (XLD). The TEM micrographs reveal that the goethite nanoparticles consist of grains and contain numerous holes and voids. However, the individual grains are found to be misaligned by low angle boundaries ($< 1°$). The SEM images confirm that the highly diluted samples contain individual nanoparticles as well as agglomerated nanoparticles, which form quasi-monolayers. The XRD data of goeth-

ite nanoparticles solved in ethanol suggest phase-pure goethite. In contrast to this the RHEED measurements and XA spectroscopy under ultra-high vacuum (UHV) condition suggest that the nanoparticles consist of a goethite and hematite. This indicates that the nanoparticles are metastable under UHV. This strongly suggests that the experimental condition under which goethite nanoparticles are investigated are important. The temperature dependent XLD measurements indicate a magnetic phase transition of individual and agglomerated nanoparticles close to the Néel temperature (400 K) of goethite in its bulk form. Further, it is found that agglomerated display a almost orientation independent XLD, while the individual nanoparticles reveal an orientation dependent XLD. The orientation dependent XLD contribution of individual goethite nanoparticles is attributed to the crystal structure of the individual nanoparticles. The magnetic dichroism in agglomerates and individual nanoparticles suggests that the spin axis of the nanoparticles preferentially is oriented perpendicular the the sample. The data indicates the occurrence of a interface effect between the SiO_x substrates and the nanoparticles, which is able to reorient the spin axis perpendicular to the substrate.

Secondly, CoO/Co_3O_4 core-shell nanoparticles are investigated by SEM, XA spectroscopy, XMLD/XMCD spectromicroscopy. It is found that the nanoparticles exhibit a regular octahedral shape using SEM. The core shell morphology is studied using XA spectroscopy, which reveals no significant amount of Co_3O_4 in the XA signal indicating that the shell is likely very thin, completely absent, or consists of highly deffective Co_3O_4. The defective nature of the shell is indicated by the almost no traces of Co^{3+} found in the XA spectra. A phase transition from paramagnetic to antiferromagnetic is found very close to the Néel temperature (290 K) of bulk CoO. The azimuthal XMLD spectroscopy and XMLD contrast images reveal a pronounced orientation dependent XMLD effect. From the orientation dependent XMLD contrast images the antiferromagnetic spin axis of individual CoO nanoparticles is determined suggesting that at least a part of the nanoparticles exhibit a spin axis which is consistent with the direction known in CoO in its bulk form. Additionally, XMDC contrast images show the existence of uncompensated magnetic moments in individual CoO nanoparticles. By studying the time dependence of the XMCD contrast it is revealed that those magnetic moments behave superparamagnetically at 100 K. Such superparamagnetic relaxations cannot be observed by means of

the XMLD contrast images. However, due to the intrinsic insensitivity of the XMLD to 180 ° sublattice inversion it cannot be excluded that such inversion are happening.

Antiferromagnetism at the nanoscale is a very exciting topic. In order to make the experimental results understandable the known magnetic properties of goethite, rocksalt CoO, wurtzite CoO, and Co_3O_4 will be discussed in **Chapter 2**. In **Chapter 3** an introduction to the generation of polarized synchrotron radiation will be provided. Moreover, it it will be explained how such radiation is used in order to chemically and magnetically characterize $3d$ transition metal oxide nanoparticles. For this the fundamental principle of XA spectroscopy and the x-ray linear and circular dichroic effects at the $L_{2,3}$ edges are introduced. Further in **Chapter 4** the experimental details are introduced including the preparation of the sample, analytical techniques (XA/XMLD/XMCD spectromicroscopy, RHEED, XRD, SEM and TEM), and the applied data analysis. After those fundamental considerations the experimental results for individual and agglomerated goethite nanoparticles are presented in **Chapter 5** and then the results of the CoO/Co_3O_4 core shell nanooctahedra will be discussed in **Chapter 6**. Finally, **Chapter 7** and **Chapter 8** present an overall conclusion and an outlook, respectively. **Chapter 8** provides information about different nanoparticle systems which could potentially be explored as well as a new state of the art microscopy method in order to study antiferromagnetism on the nanoscale with largely improved spatial resolution potentially allowing to investigate magnetic substructures of individual nanoparticles.

Chapter 2

Magnetic properties of goethite and cobalt oxides

In this chapter, the structural and magnetic properties of goethite ($\alpha - \mathrm{FeOOH}$) and three cobalt oxides are discussed. In case major discrepancies are known between the bulk and nanoscale properties, they will be addressed. In the case of cobalt oxide, the rocksalt CoO and Co_3O_4 are discussed as they are primarily expected to appear in the investigated cobalt oxide nanoparticles [52, 85]. Additionally the wurtzite CoO phase is shortly reviewed, since this is in particular a metastable phase, which is known to be stabilized at the nanoscale. In the following, if there is no specification made, CoO refers exclusively to the rocksalt CoO, whereas the wurtzite phase is specified as $\mathrm{w} - \mathrm{CoO}$.

2.1 Magnetic properties of goethite

Goethite ($\alpha - \mathrm{FeOOH}$) is a very abundant iron oxide in the earth crust. Among the many iron oxide which appear naturally, goethite is one of the most stable ones. Goethite has an orthorhombic ($Pnma$) unit cell with lattice parameters a=9.956 Å, b=3.022 Å, and c=4.608 Å [86]. Usually, goethite appears in nature in form of microscale pseudo single crystals or in a nanogranular phase [87]. Synthetic goethite is most commonly nanogranular [87, 88]. While nanosized single crystals are often found to be elongated along their b-axis [68, 73, 89–92] larger polycrystals are elongated along their a-axis [86]. The elongation along the a-axis of polycrystalline goethite is promoted by the tendency

of crystallites to attach to each other at the $b-c$ plane [86]. This attachment favors the formation of low angle grain boundaries [86, 87]. Additionally, goethite nanoparticles are often found to exhibit voids and holes [89, 93].

Goethite transforms to hematite ($\alpha - Fe_2O_3$) starting at 520 K under ambient conditions [94–96]. The onset temperature of the structural phase transformation is known to be affected by the conditions under which the material is heated, for example, in a vacuum of 6×10^{-5} mbar the structural phase transition from goethite to hematite can happen as low as 420 K [97].

In its bulk form, goethite is well known to be antiferromagnetically ordered below 400 K [72, 98]. The magnetic spin axis of goethite is along the crystal b-axis [98]. Thus, the magnetic spin axis is on the cross section of nanoparticles, which are elongated along the a-axis. However, there are some indications found by neutron scattering experiments suggesting that the magnetic spin axis can be reoriented from the b-axis into the c-axis by 13-52 ° [71, 72].

Goethite nanoparticles are often found to exhibit superparamagnetic behavior down to low temperatures [69, 73, 89, 90]. This is attributed to the small volume found for grains in goethite nanoparticle. There is still some ambiguity about the origin of the superparamagnetism in goethite nanoparticles since it is not clear if the superparamagnetic relaxation is driven by the superparamagnetic relaxation of individual grains [90] or by a collective superparamagnetic relaxation of a nanoparticle as a whole [89].

2.2 Magnetic properties of cobalt oxides

2.2.1 Magnetic properties of rock salt cobalt oxide

T_N of bulk CoO is usually around 290 K [17]. In the paramagnetic high temperature phase ($T > T_N$) CoO exhibits a cubic unit cell ($Fm3m$) with a=4.258 Å [17, 99]. Below the T_N, in the antiferromagnetic phase the lattice undergoes a Jahn-Teller like lattice deformation to a monoclinic unit cell ($C2/m$) with a=5.180 Å, b=3.015 Å, and c=3.017 Å [100–102]. In both configurations the octahedrally coordinated Co^{2+} ion exhibits a high spin state with three unpaired $3d$-electrons. The monoclinic cell can be projected on a nearly cubic unit cell with a=b=4.265 Å and c=4.217 Å and $\alpha = \beta = \gamma = 89°58'$ [99, 102].

There is still some debate on the magnetic structure of CoO. However, most likely CoO exhibits a collinear spin structure along the tetragonal distortion axis within the nearly cubic unit cell below T_N [103]. Thus, the antiferromagnetic spin axis is along [001]. The spins are generally canted out of the [001] direction by about 11° since the spins point actually along $[\bar{1}\bar{1}7]$ [17, 104, 105]. This is a consequence of the competition between the dipolar interaction favoring the orientation of the spin within a (111) plane and the exchange interaction, which tries to align parallel to the tetragonal axis [17].

CoO nanoparticles with sizes between 5 - 100 nm are routinely found to exhibit uncompensated magnetic moments [52, 85, 106–110]. Reports on the influence of annealing in N_2 [107] and vacuum [108] suggest that the formation of oxygen vacancies or potentially metallic vacancies might give rise to effective magnetic moments within nominally antiferromagnetic CoO nanoparticles. Additionally, it has been speculated that the lowered coordination at the particles surfaces might allow the establishment of an uncompensated multi-sublattice configuration [109] instead of just two antiferromagnetic sublattices. Further, the magnetic moments within CoO nanoparticles have been described to contain a large orbital contribution at low temperatures [110], which might even allow for a spin reorientation at low temperatures.

2.2.2 Magnetic properties of wurtzite cobalt oxide

Wurtzite CoO has a hexagonal unit cell ($P6_3mc$) with $a = b$ =3.244 Å, and c =5.203 Å. The Co^{2+} ions are tetrahedrally (T_d) coordinated. The tetrahedrally coordinated Co^{2+} ions exhibit a high spin state and couple ferromagnetically within the $a - b$ plane, while adjacent $a - b$ planes coupled antiferromagnetically along the c-axis. There is still some ambiguity about the magnetic ground state of wurtzite. It has been show that a collinear and a spin frustrated trigonal spin orientation within the $a - b$ planes potentially could form the magnetic ground state [111–113].

w − CoO so far has been observed only in small nanoparticles and ultra-thin films [114, 115], since it is found to be unstable and to spontaneously reorganize to rocksalt CoO at larger volumes. In nanoparticles, w − CoO is often found together with zinc blend CoO [116] indicating that the two phases exhibit a codependency. In this chapter zinc blend CoO is not discussed further since it only seems to appear as a parasitic phase within

small nanoparticles of w-CoO [114, 116].

The Néel temperature of w − CoO is usually reported to be between 200 - 250 K [29]. However, there are studies which find a ferromagnetic response for w − CoO nanoparticles even above room temperature [116–119]. At this point it is in fact not clear where the room temperature magnetic moments originate from. One explanation is that in fact the formation of vacancies at the surface of w − CoO nanoparticles gives rise to this unusual parasitic magnetic behavior, which seems not necessarily to depend on the magnetic order within the nanoparticles.

2.2.3 Magnetic properties of spinel cobalt oxide

Co_3O_4 crystallizes in a cubic ($Fd\bar{3}m$) unit cell with a=8.082 Å. It consist of tetrahedrally coordinated Co^{2+} ions and octahedrally coordinated Co^{3+} sites which are arranged in a normal spinel structure which is noted as $[Co^{2+}]^{tet}[Co_2^{3+}]^{oct}O_4^{-2}$. It has been reported that the octahedral Co^{3+} ions appear in a low spin state which yields S=0, thus the octahedral sides behave diamagnetic [120]. The tetrahedral Co^{2+} sides are in a high spin state and thus carry a spin of S=3/2. Thus, the magnetic order within Co_3O_4 is entirely promoted by the exchange interaction between neighboring Co^{+2} sides. However, the exchange interaction between those sides is weak which explains that the magnetic ordering transition for Co_3O_4 is at $T_N = 40K$ [120].

Co_3O_4 nanoparticles have been synthesized in various sizes and shapes, such as spheres, wires, flower-like structures [64, 121, 122]. In a study on spherical nanoparticles in a size range between 3-30 nm, a significant increase of the magnetic moment as well as the blocking temperature was found for nanoparticles below 10 nm [123, 124]. The magnetic moments of nanoparticles with a size of about 3 nm have been found to be $8\mu_B$ [123], which is more than double of what is expected by Co_3O_4 in its bulk form. This observation has been attributed to Co^{3+} ions with possible oxygen vacancies as well as symmetry breaking in crystals of such a small sizes [123]. The same magnetic properties have been confirmed for nanoparticles with sizes between 2-3 nm [125] and further no significant decrease of the Néel temperature of Co_3O_4 nanoparticles of such small sizes was found. In contrast, Co_3O_4 nanoparticles with a size of about 30 nm were found to exhibit a significant exchange bias effect [126]. The appearance of the exchange bias has been attributed to the formation of a

spin core-shell structure. Overall, it becomes clear that the magnetic properties of Co_3O_4 nanoparticles vary significantly depending on the size, shape, and even the synthesis route chosen to produce the nanoparticles.

Chapter 3

Probing the chemical and magnetic properties using synchrotron radiation

X-rays are widely used to study various system in fields such as condensed matter physics, chemistry [127], biology [128], archaeology [129], art history [130] etc. In this thesis the chemical, structural, and magnetic properties of individual $3d$ transition metal oxide nanoparticles are investigated. Specifically $\alpha - \mathrm{FeOOH}$ nanoparticles and $\mathrm{CoO}/\mathrm{Co_3O_4}$ core-shell nanooctahedra are studied using spatially resolved x-ray absorption spectroscopy to determine their respective chemical and magnetic properties [131]. In order to study magnetic properties of those two types of $3d$ transition metal oxide nanoparticles the x-ray magnetic linear (XMLD) and circular (XMCD) dichroic effects are employed. Such investigations require highly intense, tunable, and polarized synchrotron radiation which the Swiss Light Source (SLS) provides. Thus, in this chapter the fundamental working principles of synchrotron sources are discussed. Further x-ray absorption spectroscopy, the x-ray linear dichroism (XLD) effect, and the XMCD effect at the resonant $L_{2,3}$ edges of $3d$ transition metals are introduced. In case of the XLD the XMLD and the x-ray natural linear dichroism (XNLD) arising from the crystal structure are discussed separately.

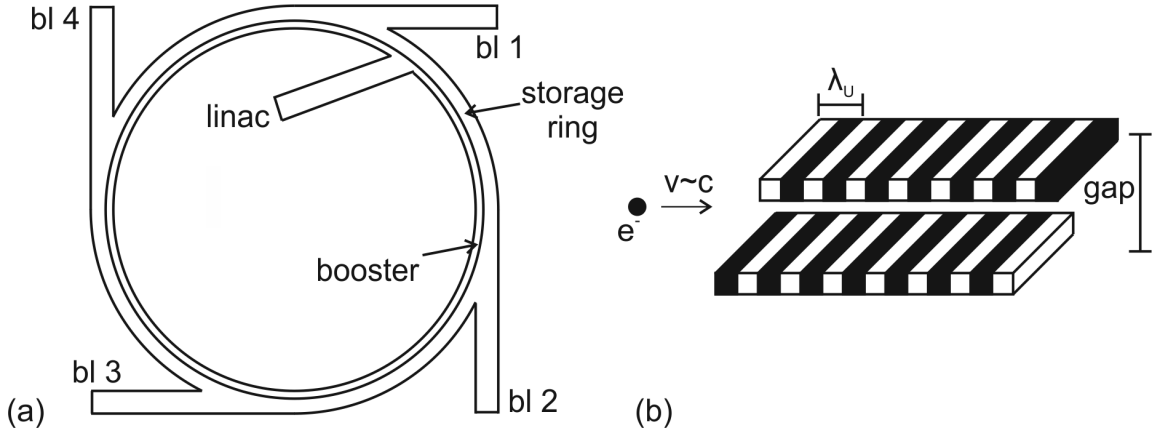

FIG. 3.1: (a) Schematics of a synchrotron radiation facility with a linear accelerator (linac), the booster ring (booster), the storage ring, and the beamlines (bl1 - bl4). (b) schematics of a linear undulator.

3.1 Synchrotron radiation and polarized X-rays

Synchrotrons are cycloidal particle accelerators, which are used to accelerate electrons very close to the speed of light c. As seen in Fig. 3.1(a) typical synchrotron facility consists of an electron source, a linear accelerator, a booster ring, and a storage ring. In the following the focus is put on the Swiss Light Source [132], since this is the only synchrotron facility utilized in this thesis. The electrons are generated by an injector consisting of an solid state target which is excited by a pulsed laser. The extracted electrons enter the linear accelerator (linac) from which the electrons are kicked to the booster ring at a energy of 100 MeV (0.9974 c). As soon as the electrons reach an energy between 2.4-2.7 GeV (0.99999996 c) the electron bunches are kicked into 'buckets' of the storage ring [132].

X-rays are generated using insertion devices (ID). Three common types of IDs are bending magnets, wigglers, and undulators [133]. In this chapter only undulators are discussed since this type of ID is the only one used in this thesis. In Fig. 3.1(b) the schematics of a linear undulator is shown, which consists of two arrays of permanent magnets. A linear undulators allows to generate only linearly polarized x-rays. Thus, in practice elliptical undulators are used allowing to access variable x-ray polarizations. The polarization of the emitted x-rays is controlled adjusting the shift between the two arrays of permanent magnets. This allows to choose linear polarization for angles between 0°and 90°as well as circular ($C^{+/-}$) polarizations. The emitted synchrotron radiation is in the x-ray range due to the relativistic speed of the electrons in the storage ring. The photon

energy of the synchrotron radiation can be controlled tuning the width of the undulator gap as shown in Fig. 3.1(b). The emitted x-rays are cast into the beamline passing a series of optical element which are used to get a well defined x-ray ray beam. Since the radiation emitted from a undulator displays a relatively wide energy distribution additionally monochromators are used consisting of a dispersive grating and an x-ray mirror. In the end highly intense, monochromatic, and polarized x-rays are obtained which is of profound interest for employing XA spectroscopy and consequently utilizing the XLD and XMCD effects in order to study the chemical and magnetic properties of the goethite (Chap. 5) and CoO (Chap. 6) nanoparticles.

3.2 Resonant soft x-ray absorption spectroscopy

X-ray absorption spectroscopy is based on exciting electrons from the occupied core levels into unoccupied states above the Fermi edge. In order to probe the chemical and magnetic properties of $3d$ transition metal oxides soft x-rays are used, which have a photon energy between 700 - 810 eV. Specifically, electrons from the occupied $2p$ bands are excited to empty states above the Fermi edge of the $3d$ bands. The electronic transition is described by Fermis golden rule as $\mathrm{P_{i\to f}} \propto |\langle \mathrm{f}|\mathrm{H'}|\mathrm{i}\rangle|^2 \rho_\mathrm{f}$, where f are the final states in the partially filled $3d$ bands, i the initial state in the filled $2p$ bands, H' the dipole transition operator, and ρ_f the density of states of the final states. The transitions are governed by optical selection rules where $\Delta \mathrm{l} = \pm 1$ and $\Delta \mathrm{s} = 0$. Due to the strong spin-orbit coupling in the $2p$ levels the degeneracy is lifted and the $2p$ levels split into the $2p_{1/2}$ and $2p_{3/2}$. The splitting of the $2p$ bands gives rise to the appearance of the L_3 ($2p_{3/2} \to 3d$) and L_2 ($2p_{1/2} \to 3d$) absorption edges. By probing the empty states in the $3d$ bands of $3d$ transition metals it is possible to investigate the magnetic properties since the magnetism in those materials is contained in the $3d$ bands. The magnetic contribution to the absorption at the $L_{2,3}$ edges is discussed further in Chaps. 3.3 (XMCD) and 3.4.2 (XMLD).

The transition energy diagram for an $L_{2,3}$ absorption is shown in Fig. 3.2(a). The diagram reveals that the $2p_{1/2}$ is lower in energy that the $2p_{3/2}$. This yields that the transition energy at the L_2 edge is larger than at the L_3 edge. Figure 3.2(b) displays the XA spectra at the $L_{2,3}$ edge of iron revealing that the L_2 edge appears indeed about

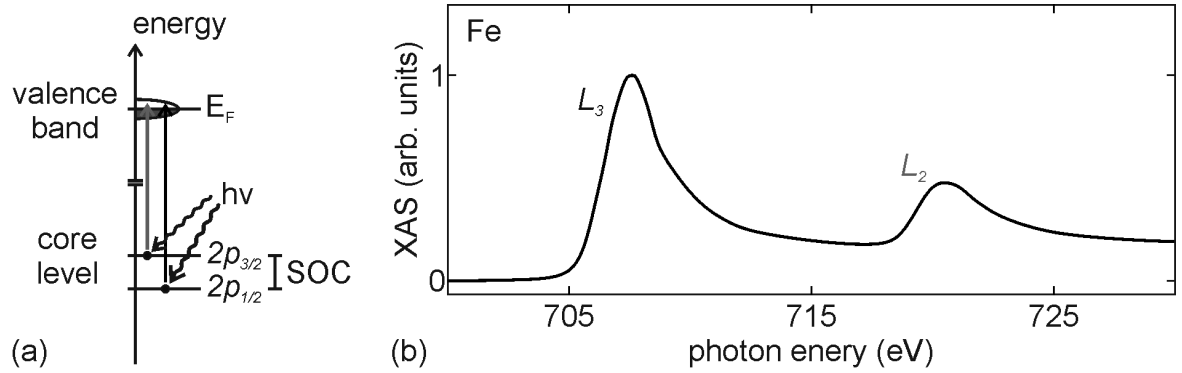

FIG. 3.2: (a) Schematic of the excitation from the $2p$ core levels to the $3d$ levels above the Fermi energy E_F. The schematic is adapted from Stöhr *et al* [18]. (b) XA spectra of a metallic iron recorded across the resonant Fe $L_{2,3}$ absorption edges.

13 eV higher than the L_3 edge. At both edges the spectrum shows a single peak which is typical for metallic compounds. In contrast to this the XA spectra of $3d$ transition metal oxides exhibit so called multiplet structure due the the presence of a crystal field splitting. The crystal field splitting of XA spectra can be seen in the goethite and CoO spectra displayed in Chap. 5 and Chap. 6 as well as in the discussion of the XMLD effect on LFO in Chap. 3.4.2.

3.3 X-ray magnetic circular dichroism

In the following, ferromagnetically ordered cobalt is considered with its magnetic moments oriented parallel to the propagation directions of the x-rays. Figure 3.3(a) displays a schematics of the transition energy diagram if this sample is illuminated by circularly polarized x-rays giving rise to the XMCD effect.

The $3d$ bands are split into spin up and spin down states. The imbalance of the filling of those states results in different transition probabilities for C^+ (black) and C^- (gray) polarized photons. This is the origin of the XMCD effect. The spectra displayed in Fig. 3.3(b) reveal that the XMCD sign is inverted if the L_3 and L_2 edges are compared. In another approach it is possible to measure the sample with a single circular polarization but inverting the directions of the magnetic moments for example by first applying a magnetic field parallel and then antiparallel to the propagation direction of the x-rays [18, 134–136]. Those two approaches are expected to yield the same XMCD spectrum.

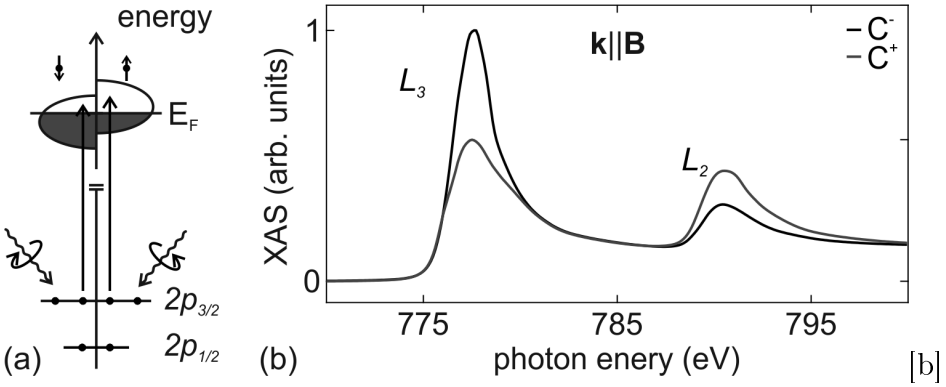

[b]

FIG. 3.3: (a) Circularly polarized x-ray excitation from the $2p$ core levels to empty states in the $3d$ bands of a magnetic media. The C^+ and C^- polarized x-rays are absorbed differently depending on the magnetization of the material. (b) the XA absorption spectra recorded with C^+ (gray) and C^- (black) polarized x-rays at the Co $L_{2,3}$ edges with magnetic field applied parallel to the propagation direction of the x-rays.

Since the magnetic moment has a direction the magnitude of the XMCD effect depends on an angle α between $\mathbf{k}$ and the magnetic moment $\mathbf{M}$ of the sample as $I_{XMCD} \propto \mathbf{k} \cdot \mathbf{M} = \mathbf{M} \cdot \cos(\alpha)$. Thus, the XMCD effect can be used to determine the direction of magnetic moments with element specificity. Probing the XMCD effect allows to probe magnetic moments as small as $0.01\,\mu_B$/atom [137].

3.4 X-ray linear dichroism (XLD)

The absorption of linearly polarized x-rays in a medium depends on various factors. In the most general case, those factors can give rise to birefringence or dichroic effects [138]. The focus here is on the magnetic and structural dichroism. The two dichroic effects are the XMLD and XNLD. Both of them have been extensively studied before on other systems [19, 31, 32, 80, 81, 139]. It can be challenging to disentangle both contributions to the total XLD. Generally, it can be noted that the XLD arises from the so-called 'search light' effect, which manifests itself as an increased absorption of the x-ray when $\mathbf{E}$ of the linearly polarized x-rays is parallel to the empty states in the $3d$ bands.

3.4.1 X-ray natural linear dichroism (XNLD)

In a cubic crystal field the XNLD vanishes due to the high crystal symmetry with the empty states in the $3d$ bands are distributed within a nearly spherical potential [31].

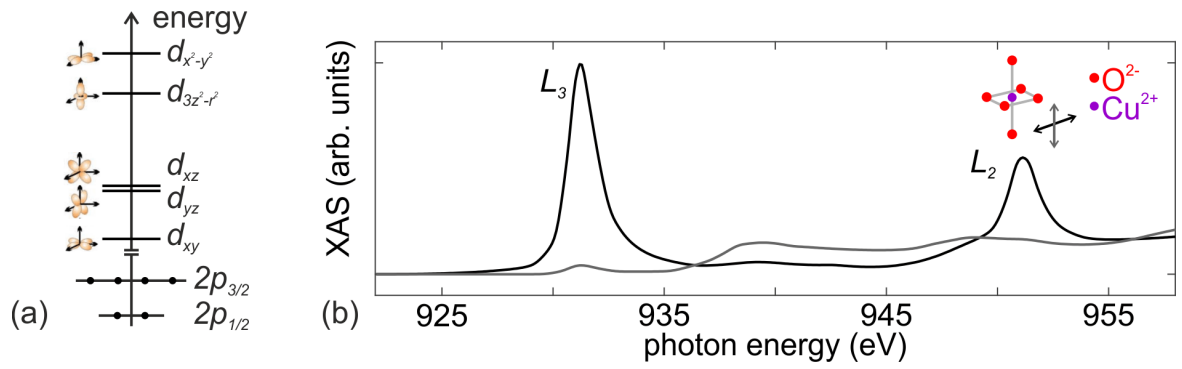

FIG. 3.4: (a) Splitting of the 3*d* shells of Cu^{2+} ion in a tetragonal crystal field. (b) the XA spectra for **E** ∥ $d_{x^2-y^2}$ (black) and E ∥ $d_{3z^2-r^2}$ (gray). The figure is adapted from Chen *et al.* [139]

Here, the polarization dependent x-ray absorption of $La_{1.85}Sr_{0.15}CuO_4$ with a tetragonal distortion of the crystal field [139] is discussed. Figure. 3.4(a) the $L_{2,3}$ energy level diagram of the $L_{2,3}$ edge of Cu^{2+} is shown visualizing the splitting of the five 3*d*-orbitals.

The electronic configuration of a Cu^{2+} ion is [Ar]$3d^9$, consequently there is only one empty state in the 3*d* band located in the $d_{x^2-y^2}$ orbital. From the schematic representation of the orbital it can be easily seen that the half filled $d_{x^2-y^2}$ and fully occupied $d_{3z^2-r^2}$ are oriented orthogonally to each other. Thus, the x-ray absorption should be high if **E** $\|d_{x^2-y^2}$ and low for **E** $\|d_{3z^2-r^2}$. This expected behavior is clearly demonstrated by the XA spectra displayed in Fig. 3.4(b). This case is the most simple case imaginable, since there is only one empty state in the 3*d* bands. In a more general case this usually is more complex. Especially, the analytical understanding of the behavior of the XNLD gets increasingly complicated if the symmetry of the crystal field is lowered further [82]. Consequently, the orientation dependent behavior of the total XLD in a magnetic system might also get more complex.

3.4.2 X-ray magnetic linear dichroism (XMLD)

XMLD arises from an non-spherical charge distribution in the *d*-orbital caused by the spin orbit coupling when the spins become axially aligned due to the exchange interaction [138]. The spin and orbital moments couple to the crystal field. This leads to a multiplet splitting of the XA spectrum since degeneracies are lifted. It has been observed that the XMLD can become relatively large in multiplet split systems compared to simple metallic

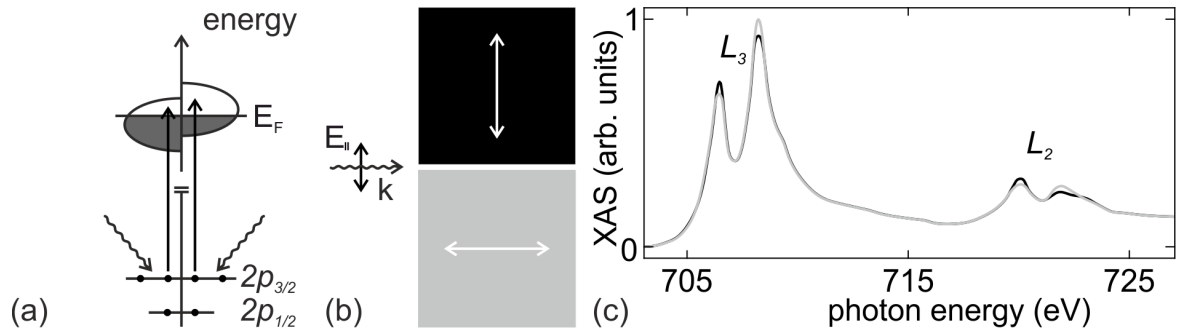

FIG. 3.5: (a) Diagram of the electronic $2p \rightarrow 3d$ transitions using $\mathbf{E}_\perp$ and $\mathbf{E}_\parallel$ polarized x-rays. (b) X-ray absorption spectra recorded at the Fe $L_{2,3}$ edges using $\mathbf{E}_\perp$ (gray) and $\mathbf{E}_\parallel$ (black) polarized x-rays. The difference

systems [138]. The XA spectra of $3d$ transition metal oxides display multiplet split $L_{2,3}$ edges.

The XMLD probes the orientation of the axis formed by the distorted sub-orbital population with respect to $\mathbf{E}$ [18, 80, 138]. Using the XMLD it is only possible to determine the orientation of the magnetic moments in a ferromagnetic system, since this effect is insensitive to an inversion of the magnetic moments by 180°. However, the XMLD effect allows to study antiferromagnetic, ferrimagnetic, and ferromagnetic ordered materials. The origin of this is that on the integration length scale (in x-ray photoemission electron microscopy usually about 50 nm) antiferromagnetic materials exhibit no spin polarization in the $3d$ bands. Thus, no net XMCD effect is obtained. However, the sub-orbital population of an antiferromagnetic material above and below the magnetic ordering temperature is different. The XMLD effect is suitable to probe the antiferromagnetic spin axis of a material [36, 38, 140]. The magnitude of the XMLD is proportional absolute projection of the antiferromagnetic spin axis ($\mathbf{M^2}$) onto the linear polarization vector ($\mathbf{E}$) of the x-rays. In its most general form the x-ray absorption of linearly polarized x-rays can be written as :

$$\mathrm{I} = \mathrm{I}_0 + \mathrm{I}_2 \cos^2(\alpha) \tag{3.1}$$

Where I_0 is the isotropic absorption intensity, I_2 the anisotropic absorption intensity, and α the angle between $\mathbf{E}$ and $\mathbf{M^2}$.

Figure 3.5 displays an XMLD measurement on $LaFeO_4$. Panel (a) shows the schematics

of the transition energy diagram of the $L_{2,3}$ edge of iron. Panel (b) displays the orientation of two antiferromagnetic domains, one where the spin axis ($\mathbf{S}$) is parallel to $\mathbf{E}_{\parallel}$ (black) and the second where $\mathbf{S} \perp \mathbf{E}_{\parallel}$ (gray). In panel (c) the according XA spectra are shown. At both absorption edges the x-ray absorption depends clearly on the orientation of $\mathbf{S}$. In the experiments reported in this thesis the orientation dependent XMLD of individual nanoparticles will be studied in order to determine the spin axis of the nanoparticles.

Chapter 4

Experimental details

In this chapter the sample preparation and the XPEEM setup are discussed in depth. Further, the data analysis steps needed for processing the data are introduced in this chapter. Further scanning electron microscopy [141] (SEM), transmission electron microscopy [142] (TEM), reflection high energy electron diffraction [143] (RHEED), and x-ray diffraction [144] (XRD) are also discussed very briefly. However, for additional information about those methods the mentioned references should be visited.

4.1 Sample preparation

4.1.1 Goethite nanoparticles

Goethite nanoparticles suspended in ethanol with a concentration of 20 %wt. (Product Nr. 720712) were purchased by Sigma-Aldrich (Merck). The nanoparticles are obtained by ball milling microsized goethite crystals. After ball milling the nanoparticles are partly covered by 3,6,9-trioxadecanic acid to improve their solubility in ethanol. The goethite nanoparticles are found to have nominally a mean length of l=110 nm and a mean width of w=30 nm using dynamic light scattering (done by Sigma-Aldrich). The stock solution is diluted to a concentration of 10^{-2} %wt. (low density samples) and 1 %wt. (high density samples).

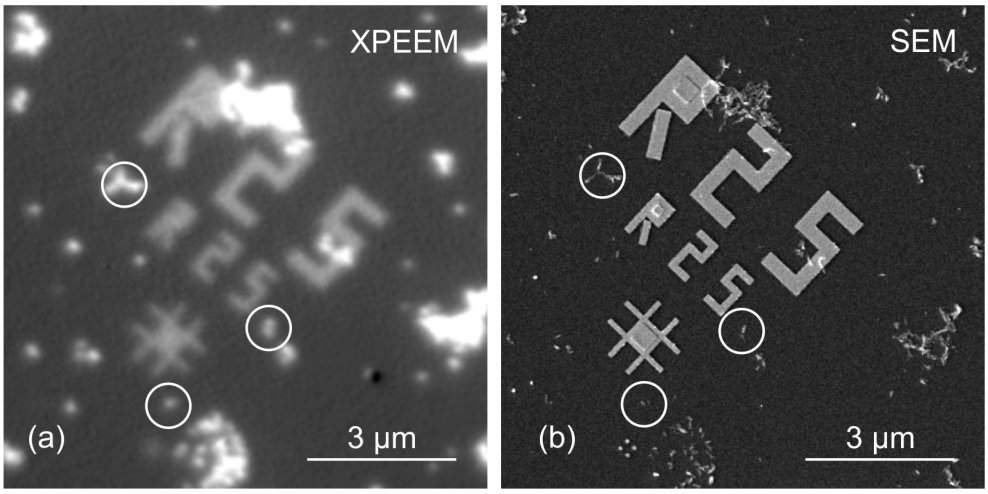

FIG. 4.1: (a) and (b) the respective elemental contrast image at the Fe L_3 edge recorded by XPEEM and a SEM image of the very same spot on a silicon substrate with gold marker structures (R25). The three white circles in the micrographs indicate the very same features

4.1.2 Cobalt oxide core-shell nanoparticles

The CoO/Co_3O_4 core-shell nanooctahedra were provided by collaborators at the University of Vigo, Spain [52]. The CoO nanooctahedra are synthesized by thermal decomposition from cobalt(II) acetate. The details of the synthesis are reported elsewhere [52, 145]. After synthesis, the nanoparticles are washed three times by ethanol and dried before being dissolved in ethanol at a concentration of 1 %wt. in order to obtain a stock solution. Before dispersing the nanoparticles on substrates the stock solution is further diluted to a concentration of 10^{-2} %wt.

4.1.3 Nanoparticle deposition

As substrates silicon [001] substrates with a native oxide layer and silicon nitride (SiN) membranes (SiMPore Inc., Product Nr. SN100-A10Q33) are used. The silicon substrates have a size of $1 \times 1\,\mathrm{cm}^2$ a contain gold marker structures produced by means of electron beam lithography, which are shown respective XPEEM and SEM in Figs. 4.1(a) and (b). (a) is a elemental contrast image at the Fe L_3 edge recorded by XPEEM and the respective SEM micrograph around the marker structure R25. The white circles highlight the very same nanoparticles in both images. The SiN membrane chips have a size of $3\,\mathrm{mm} \times 3\,\mathrm{mm}$. In the center region are nine windows with each having a size of $100 \times 100\,\mu\mathrm{m}^2$. The silicon

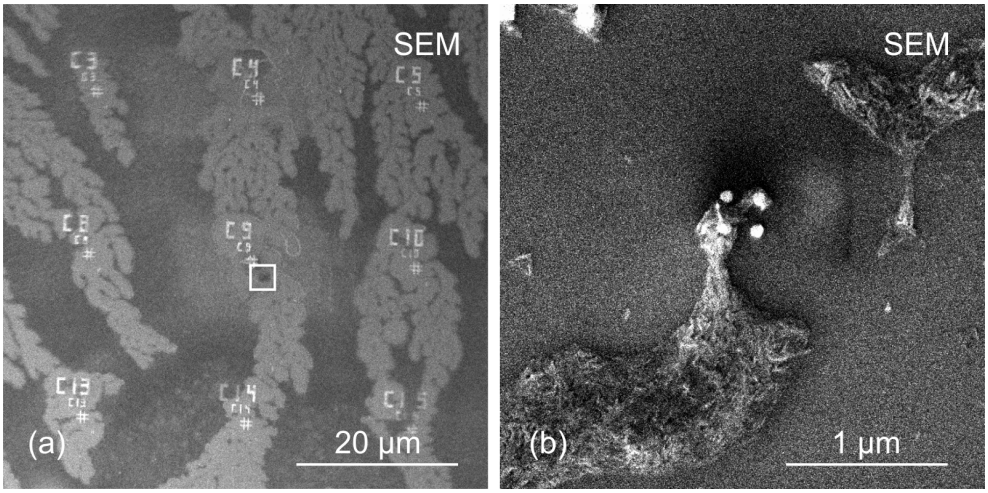

FIG. 4.2: (a) SEM image of a spot on a typical RHEED sample after the particle deposition. The white square highlights the area which is displayed in (b).

substrates are used for the XPEEM, XAS/XMCD, SEM, and RHEED measurements while the SiN membranes are used for TEM investigations.

Before dispersing the nanoparticles on the substrates the nanoparticle solution is placed in a ultrasonic bath for at least 30 min in order to prevent agglomeration of the individual nanoparticles, then the nanoparticle solution is drop cast on the substrates, and spin coated at a moderate speed of 8 Hz for about a minute. Finally, the samples are left to dry for a few minutes under ambient conditions. The final samples display some individual nanoparticles as well as agglomerates.

In case of samples for the RHEED measurements on sample with a high surface coverage are used in order to obtain a suitable signal. In this case the highly concentrates goethite nanoparticle solution is just drop cast onto silicon substrates. Figure 4.2(a) displays an overview of a typical RHEED sample and (b) a zoomed in view of the part of the sample indicated by the white square in (a). Especially from Fig. 4.2(b) becomes evident that the goethite nanoparticles rather appear in patches rather than as an closed monolayer.

4.2 Characterization

4.2.1 X-ray photoemission electron microscopy

The spatially resolved x-ray absorption spectroscopy and magnetic contrast imaging is performed using XPEEM in ultra high vacuum (UHV) at base pressure around p=5×10^{-10} mbar. Figure 4.3 shows a schematic representation of a XPEEM. The x-rays propagate ($\mathbf{k}$) along the x-direction and impinge at Θ_k =16 °. The coordinate system is given as an orthogonal system where x and y form the sample plane and z is the surface normal of the sample. Additionally, the angles Θ_s and Φ_s are defined according to the spherical coordinates. The polarization vector $\mathbf{E}_\perp$ is tilted from the z direction by Θ_k into the x-direction, while the $\mathbf{E}_\parallel$ is parallel to the y direction. The notations $\mathbf{E}_\perp$ and $\mathbf{E}_\parallel$ are used for the investigation of the goethite nanoparticles in Chap. 5. In Chap. 6 a different notation is used in the form of $\mathbf{E}_{(\Theta_s,\Phi_s)}$, where $\mathbf{E}_{(0,\Phi_s)}$ refers to $\mathbf{E}_\perp$ and $\mathbf{E}_{(90,\Phi_s)}$ to $\mathbf{E}_\parallel$. The sample can be rotated around the surface normal by an angle Φ_s. The polarization angle Θ_s can be freely rotated from 0 ° to 90 ° and azimuthal angle Φ_s from 0 ° to 360 °, which allows to record azimuthal and polarization dependent measurements. In Chap. 5 only azimuthal dependent experiments are reported while in Chap. 6 azimuthal and polarization dependent measurements. Additionally, the temperature of the microscope can be varied between 100 K and 500 K allowing temperature dependent measurements. The sample is cooled using a helium cryostat and the sample can be heated using a filament located at the backside of the sample.

In order to perform XPEEM measurements the sample is illuminated by x-rays. For the measurements a PEEM setup provided Elmitec GmbH is used. All measurements are carried out at a base pressure of about 5×10^{-10} mbar. As discussed in Chap. 3.1 the x-rays are produced by undulators which are inserted in the storage ring of the Swiss Light Source. The x-rays are used to excite electrons in the sample. Here, the secondary electrons are used to measure the absorption, which are generated by a decay cascade of the initially excited primary electrons. This mode of detection is commonly referred to as total electron yield. In order to extract the secondary electrons from the sample a high-voltage of -10 kV or -15 kV is applied to the sample. The extracted electrons then pass through the object lens into the electron optics containing a series of electromagnetic

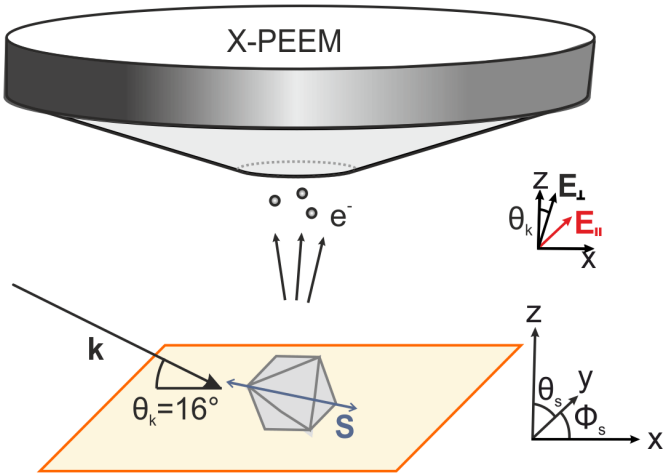

FIG. 4.3: (a) Schematics of a XPEEM with the propagation direction $\boldsymbol{k}$, the spin axis $\boldsymbol{s}$, the sample coordinate system, azimuthal rotation angle Φ_s indicated, the orientation of $\mathbf{E}_\perp$ and $\mathbf{E}_\parallel$ indicated as described in the text.

lenses and an energy analyzer, which is of fundamental importance in order to select only electrons within a small energy band. The energy range of the electrons is further narrowed down inserting a energy slit allowing to select electrons with a certain trajectory in the energy analyzer. This effectively reduces chromatic aberrations allowing to image samples with a spatial resolution as low as 50 nm. After passing the electron column the signal is amplified by an multi channel plate (MCP). The image is generated on a fluorescent screen and recorded by a CCD camera.

Utilizing synchrotron radiation with tunable photon energy it is possible to study the properties of the samples with very high intensities which allows to reduce the integration time. In this thesis the resonant absorption edges $L_{2,3}$ edges of Fe and Co are used. In order to obtain XA spectra the photon energy is tuned in steps of 0.1-0.2 eV across the absorption edges and at each energy an image is recorded and saved to a stack of raw images.

It is also possible to record elemental contrast maps. In order to achieve this one records XPEEM images at the resonant absorption edge and another in the pre-edge region. Dividing those two images pixel by pixel constructs a map where locations containing the probed atom type (e.g. Fe or Co) appear bright and the empty parts of the substrate dark.

In order to study the magnetic properties of nanoparticles one can apply XMLD and

XMCD contrast imaging. In case of XMLD images two images at two energies with one linear polarization of the x-rays are recorded. The chosen photon energies refer to parts on the spectrum where a strong XMLD signal can be observed. Preferentially the two energies should carry a inverted XMLD signs. The images acquired at one linear polarization with two photon energies are then divided pixelwise in order to obtain the XMLD contrast. This method is used in Chap. 6, since in this case only maps where all nanoparticles appear either with white or black contrast are obtained it is necessary to extract the XMLD contrast values for a quantitative analysis, which is discussed latter in this chapter.

In a similar way XMCD contrast maps can be recorded using C^+ and C^- polarized x-rays at a single photon energy where the XMCD is large. Those two image are divided pixel by pixel yielding the XMCD maps where nanoparticles appearing white or black have their respective magnetic moments oriented parallel or antiparallel to **k** of the x-ray. The shades of grays which can also be seen refer to the angle α between the magnetic moment **M** of the nanoparticles and **k** since $I_{XMCD} \propto \mathbf{M}\cos(\alpha)$ as it is discussed it detail in Chap. 3.3.

XPEEM images are recorded in a certain statistics noted as $(t_{acq} \times N) \times R$, with t_{acq} the acquisition time, N the number of averaged images, and R the number of repetitions. The statistic is of crucial importance since it determines the actual time resolution of XPEEM images which is of profound interest for XMLD and XMCD contrast images as it is further discussed in Chap. 6 on the example of the CoO nanooctahedra. Further it is important to keep the acquisition statistics in mind since each XPEEM image has to be corrected pixelwise by a so called flat field image which has to be recorded in the very same statistics in order to avoid to pick up artificial statistical noise on the data. A flat field image is recorded by means of detuning the objective lens of the microscope by 100 mA. This image then contains information about inhomogeneities of the multi channel plate (MCP). The subtraction of the flat field image from acquired XPEEM raw images should always be performed as the first processing step.

After the flat field correction of the raw data possible mechanical drifts of the images during the measurements have to be corrected. This is done by home built macros for ImageJ. In order to automate this step the, home built macros are used. In case of

spatially resolved spectroscopy, the spectra are then extracted from the stacks of images in order for further processing in Matlab. This is done by means of defining region of interests (ROI) around the nanoparticles and a close lying spot on the empty substrate. After choosing the pairs of ROIs the spectra are extracted.

The XMLD and XMCD contrast images are generated by dividing the drift corrected stacks of images recorded at two photon energies at one linear polarization respectively at two circular polarizations at a single photon energy. In case of the XMLD images it is further necessary to export the XMLD contrast data of the nanoparticles in order to analyze the data quantitatively and plotting it using Matlab.

After the spectroscopy or contrast data is exported, it is further processed and plotted in Matlab. First, the data of the particles is normalized by ROI containing the signal of the empty substrate. In case of the spectroscopy measurements usually 5 spectra at one polarization are recorded in order to improve the signal to noise ratio. Those 5 spectra are averaged. After averaging the spectra of one polarization the baselines of the spectra recorded with $\mathbf{E}_{\parallel}$ and $\mathbf{E}_{\perp}$ are corrected with respect to each other applying a least square fit. Finally the normalized dichroic spectra are calculated as $(\mathrm{I}_{\mathrm{E}_{\parallel}} - \mathrm{I}_{\mathrm{E}_{\perp}})/(\mathrm{I}_{\mathrm{E}_{\parallel}} + \mathrm{I}_{\mathrm{E}_{\perp}})$. The same procedure can also be done for XMCD spectra with recorded C^{+} and C^{-} polarized x-rays. [1]

4.2.2 Reflection high energy electron diffraction

Reflection high energy electron diffraction (RHEED) is used to investigate the crystal structure, phase stability, and eventual preferential orientations of the nanoparticles on the surface within ultra high vacuum conditions. RHEED is performed at a base pressure of about p=5×10^{-8} mbar. The experiments are conducted using electron with a wavelength λ =0.067 Å (corresponding to E=30 kV). The temperature of the sample is controlled *in situ* by means of a heating element behind the sample and is read out by a thermocouple. The diffraction patterns are projected on a fluorescence screen and images using a CCD camera. Further information on the geometry of the experimental setup as well as the calculation in order to translate the data into the usually shown q vs. intensity plots are

[1] All scripts used for the analysis of the XA, XLD, XMLD, and XMCD data can be found at `https://github.com/bracdav/portfolio/blob/master/xmld_xmcd_scripts.zip`.

found in Appendix A.

4.2.3 X-ray diffraction

X-ray diffraction measurements are carried out with a Mo K_α source (λ =0.709 Å) under ambient conditions. The samples are measured in ethanol solution at a concentration of c=20 %wt.

4.2.4 Scanning electron microscopy and Transmission electron microscopy

In order to correlate the chemical and magnetic properties of the nanoparticles with their morphology the very same spots measured by XPEEM are investigated by means of SEM. A Helios NanoLab 650 SEM is used to record the micrographs. The microscope uses a field emission source and allows to image using a secondary electron detector, a backscattered electron detector, or an in-lens detector. For high resolution imaging the in-lens detector is used. Usually a high voltage of 5 kV and a emission current of 25 pA were used to record images. With this instrument it is possible to reach a resolution of about 1 nm.

TEM images are recorded using a FEI Tencai F30 instrument at the ScopeM facilities at ETH Zürich. The instrument is run with an acceleration voltage of 200kV in the bright field mode. The spatial resolution is smaller than 1 nm and thus allows to image the lattice fringes of the nanoparticles. Images are obtained on a fluorescence screen, which is captured by a CCD camera. The obtained images are shown as raw data.

Chapter 5

Goethite nanoparticles on silicon substrates

Goethite ($\alpha - \mathrm{FeOOH}$) is one of the abundant minerals in soils, earth crust, and iron ores [86, 87, 146]. While many of the iron hydroxy-oxides are thermally unstable, goethite is thermally stabilized under ambient conditions [87]. It exhibits a close structural relation with hematite with a one step structural phase transition from goethite to hematite [94]. It is known that hematite is the most stable naturally occurring iron oxide [86, 87, 94]. Due to its structural relation to hematite, goethite is used as a marker in geopalaeontology and palaeoclimatology [147, 148]. The appearance of goethite in sediments can be directly linked to the humidity of the climate during certain geological periods. In nature goethite can be found as micrometer sized quasi-single crystals and granular nanoparticles [87]. Single crystals usually appear if the goethite has been able to crystallize within a geological timespan. Regardless of its appearance as bulk-like micro-crystals or as granular nanoparticles, goethite commonly appears in an acicular shape [87]. In its bulk phase goethite crystallizes in a orthorhombic unit cell ($Pnma$) with lattice parameters a=9.956 Å, b=3.022 Å, and c=4.602 Å [86, 96]. Goethite single crystals can exhibit a pseudo spherical morphology [69, 71] or are elongated along the b-axis [68, 73, 89–92]. Although, goethite nanoparticle are frequently found containing multiple crystalline domains [87]. Typically the crystalline domains are formed when individual single crystalline grains attach along the a-axis and form low angle grain boundaries ($<1°$) [86, 87, 149]. Hence, crystalline multi domain goethite nanoparticles are found to be elongated along

their a-axis [87].

In its bulk phase goethite is antiferromagnetically ordered with a Néel temperature (T_N) around 400 K [98]. The antiferromagnetic spin axis is oriented along the crystals b-axis [98]. However, spin axis of goethite at the nanoscale has been reported to be rotated relatively freely within the crystals $b-c$ plane [71, 72]. Since goethite has its Néel temperature (T_N) close to room temperature (RT) thermal manipulation of goethite might be easily accessible. This makes goethite a promising candidate for antiferromagnetic spintronics at RT. It is known that the purity of goethite can affect the magnetic properties. For instance trace amounts of aluminum and vanadium can lower T_N significantly [98, 150]. Thus, it is preferable to investigate synthetic goethite nanoparticles since synthetic chemistry allows to precisely control the chemical properties and purity of the goethite nanoparticles. Further, such nanoparticles can be expected to exhibit more uniform structural, chemical, morphological, and thus magnetic properties than naturally occurring goethite nanoparticles.

The magnetic properties of synthetic nanoparticles have been intensely investigated over the last 40 years. The nuclear fine splitting of goethite has been studied by means of Mössbauer spectroscopy [68, 69, 72, 73, 89–91, 93, 151], the static and dynamical magnetic properties by DC and AC magnetometry [70, 73], electron spin resonance spectroscopy [70, 73] , and muon spin relaxation [73] have been used in order to determine T_N and the blocking temperature (T_B) of goethite nanoparticles. Neutron scattering has been utilized to determine the preferred spin axis of goethite nanoparticles [71, 152]. A study combining all the previously mentioned methods on the very same goethite nanoparticle sample revealed the dynamic magnetic properties of goethite nanoparticles from the order of seconds down to nanoseconds [90]. Further the influence of the concentration of oxygen vacancies on the magnetic properties has been studied using positron annihilation lifetime spectroscopy [92] revealing that T_N of goethite nanoparticles is correlated with the concentration of Fe^{3+} vacancies. Mössbauer spectroscopy studies on goethite nanoparticles with similar volumes sometimes yield inconsistent values for T_N and T_B indicating that factors such as the synthesis route, natural origin, purity etc. [98] can play a major role.

Another origin of the large scattering of the magnetic properties is likely that goethite nanoparticles have usually been probed in form of powder samples. Such measurements

integrate over a large amount of nanoparticles regardless the morphology and the structure of the individual goethite nanoparticles. However, in order to employ nanoparticles for antiferromagnetic spintronics one has to understand the antiferromagnetic properties of the individual nanoparticles. Although, powder measurements have been successful on discussing phenomena such as superparamagnetic behavior [69, 90, 92, 98], uncompensated magnetic moments [91], and inter-particle interactions [65, 67, 68] it has not been possible to determine definitely their origin. Further one has to study effects of the interactions between nanoparticles and substrates on the magnetic properties since those will become very important in device applications. Lastly, to fully understand the magnetism of goethite nanoparticles the influence of the chemical composition, shape, and microstructure of individual goethite nanoparticles has also to be considered. This study addresses the influence of the chemical composition and morphology on the magnetic properties of individual goethite nanoparticles and their agglomerates.

In this chapter individual and agglomerated goethite nanoparticles deposited on SiO_x substrates are investigated by means of x-ray photoemission electron microscopy (XPEEM), scanning electron microscopy (SEM), transmission electron microscopy (TEM), x-ray diffraction (XRD), and reflection high energy electron diffraction (RHEED). The structural and chemical properties are examined by means of XRD, RHEED, and x-ray absorption (XA) spectroscopy. Additionally, the temperature dependence of the RHEED patterns is used to investigate the thermal stability of goethite nanoparticles within UHV. The morphology of individual goethite nanoparticles is studied by means of TEM and SEM. XPEEM is used in order to record polarization dependent XA spectra of individual goethite nanoparticles and agglomerates. In order to study the magnetic properties the XMLD effect is utilized.

The XRD measurements on the nanoparticles dispersed in ethanol reveal phase pure goethite. However, upon dispersion and insertion into UHV for the RHEED measurements and XA spectroscopy may suggest a partial transition from goethite to hematite. Temperature dependent RHEED patterns indicate the on set of the goethite-hematite phase transition around 520 K as reported previously [94, 95, 97]. When the acicular nanoparticles are deposited on the SiO_x substrate they orient their long axis parallel to the sample. This is found for individual and agglomerated nanoparticles. Thus, the a-axis

of the crystals is parallel to the sample plane. An effective XLD effect is revealed by integrating over agglomerates of randomly oriented nanoparticles. This phenomenon is further investigate by studying the temperature dependence of the XLD spectra which display a distinct and reversible change close to T_N [98]. This behavior is attributed to a the transition of goethite from its antiferromagnetic to its paramagnetic phase. Additionally the azimuthal dependence of the XLD of agglomerated goethite nanoparticles is investigated. In contrast, the orientation dependent XLD of individual reveal a XLD anisotropy with respect to the azimuthal orientation, which is likely due to the crystal structure of the nanoparticles. However, in case of the XMLD contribution to the XLD no distinct angular dependence can be found for agglomerated and individual goethite nanoparticles. This observation is explained by a preferential orientation of the spin axis of individual goethite nanoparticles perpendicular to the sample plane. This is understood as a consequence of a relatively freely rotatable spin axis within the $b-c$ plane [71] and an interface effect between the goethite nanoparticles and the non-magnetic SiO_x substrate. Hence, the XLD study yields first evidence of an influence of nanoparticle-interface interactions on the orientation of the spin axis of antiferromagnetic nanoparticles as it has been found in ferromagnetic nanoparticles and in ferromagnetic and antiferromagnetic thin films. [153, 154].[1]

5.1 Morphology, structure, and chemical stability

5.1.1 XRD and RHEED

Figure 5.1(a) shows the micrograph of two attached goethite nanoparticles recorded by TEM. The length l of the two nanoparticles is about 70-80 nm and the width w is about 12 nm. Those values are slightly below the specification provided by Sigma-Aldrich which were found using dynamic light scattering (DLS). Note, that DLS measures the hydro-

[1]Sample preparation and SEM characterization of the samples was performed by me with help of Dr. M. Wyss and D. Mathys (Nano Imaging Lab, University of Basel). XPEEM characterization was performed by me, Dr. T. Savchenko, and Dr. A. Kleibert at the Surface/Interface (X11MA) beamline at the Swiss Light Source (SLS). RHEED measurements were done by me and Dr. C. A. F. Vaz. TEM measurements are carried out by Mrs. Savchenko and Dr. F. Gramm. The goethite nanoparticles were provided by Dr. M. A. Brown and the XRD measurements were performed by G. Olivieri and G. Alok. Code development and data analysis was done by me.

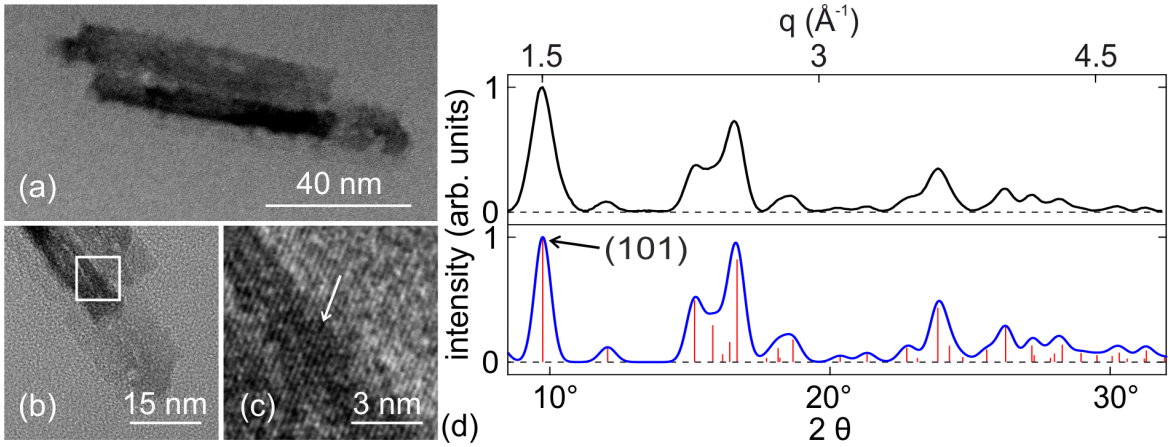

FIG. 5.1: (a) TEM image of two close-lying goethite nanoparticles. (b) High-resolution TEM image of a part of a goethite nanoparticle. Panel (c) the part highlighted in the white square in (b) is magnified. The white arrow points to a low angle grain boundary. (d) Upper part: Experimental x-ray diffraction pattern of the nanoparticles in ethanol suspension. Lower part: simulated goethite XRD diffraction lines (red lines). The blue curve is obtained by convoluting the diffraction lines by a Gaussian according to the mean grain size of 4 nm as calculated using the Scherrer equation with the experimental line width at the (101) reflection (black arrow).

dynamic size which often is larger than the actual size of nanoparticles [155]. The TEM micrograph in Fig. 5.1(a) reveal defects and voids as frequently reported for goethite nanoparticles in literature [68, 69, 87, 89, 93]. However, it is possible that the illumination by the electron beam can as well damage the nanoparticles over time[2] and the compromised areas can appear as void-like defects in the TEM images. Figure 5.1(b) displays a high resolution TEM image of a goethite nanoparticle and (c) the magnified image of the section highlighted by the white square in (b). The nanoparticles exhibit a number of grain boundaries. The almost uninterrupted continuation of the lattice fringes is consistent with the low angle grain boundaries ($<1°$) reported in the literature [87, 149].

The upper panel of Fig. 5.1(d) displays the experimentally obtained XRD data (black line) for goethite nanoparticles dissolved in ethanol. The lower panel shows the expected powder diffraction lines (red) as calculated by VESTA 3 [156] using a crystal model for goethite as listed in the *Inorganic Crystal Structure Database (ICSD)* [150, 157]. The x-ray powder diffraction calculation is based on kinematic scattering theory. From the experimental data the grain size is estimated applying the Scherrer equation [158] as

[2]Private communication with T. Savchenko, who took the TEM micrographs of the goethite nanoparticles.

$\tau = (\kappa\lambda)/(\beta cos\Theta)$, with κ being the dimensionless shape factor (0.9), λ the wavelength of the used x-rays (Mo $K_\alpha = 0.709$ Å), β the full width at half maximum (FWHM) in radians of a diffraction peak, and Θ half the angle at which the diffraction peak appears in the $\Theta - 2\Theta$ scan. First, a Gaussian profile is fitted to the isolated (101) peak. The fit yields $\beta = (1.57 \pm 0.07) \times 10^{-2}$ rad. The position of the (101) peak taken from the calculated XRD lines reads Θ =4.87 °. The Scherrer formula gives then a grain size $\tau = 4.1 \pm 0.2$ nm. For comparison with the experimental data the calculated diffraction lines are broadened using τ. The resulting curve is shown in the lower panel in Fig. 5.1(d) and matches well with the experimental data in the upper panel. Note, that the instrumental broadening has not been subtracted from the data which means that the grain size might be slightly underestimated. Additionally it is likely that a part of the broadening is caused by strain within the nanoparticles.

The stability of the goethite nanoparticles under UHV conditions as well as with respect to the sample temperature is studied using RHEED, which is suitable to probe the structural properties of a submonolayer of goethite nanoparticles. The sample preparation for those experiments is discussed in Chap. 4.1.3. The RHEED pattern give insight in weather the nanoparticles display a preferential orientation on the SiO_x substrates [78, 159]. The RHEED setup has a base pressure of 1.5×10^{-8} mbar and provides the possibility to heat the sample. The investigated temperatures ranges from 300 K to 520 K. In Fig. 5.2(a) the RHEED pattern from the fluorescence screen as recorded by the CCD camera is shown. The raw RHEED image reveals Laue rings without any texture indicating a random distribution of the nanoparticles on the SiO_x substrate.

The white circle in Fig. 5.2(a) shows the position of the direct beam, which defined q=0 Å^{-1}. The full line profile across the white dashed line is shown as the inset in Fig. 5.2(a) and the white rectangle highlights the part on the line profile between 2.7 Å^{-1} and 5.5 Å^{-1} where detailed analysis of the data is performed. This interval is chosen to avoid the beam imprint present around 2.5 Å^{-1}. For higher q-values than 5.5 Å^{-1} the signal decreases bellow the noise level. The extracted line profiles for 300 K is shown in Fig. 5.2(e). For comparison the calculated diffraction lines (red) for goethite [150, 157], hematite [160, 161], and maghemite [162, 163] are displayed in Figs. 5.2(b)-(d). In order to simulate the actual RHEED curves the diffraction curves are convoluted with

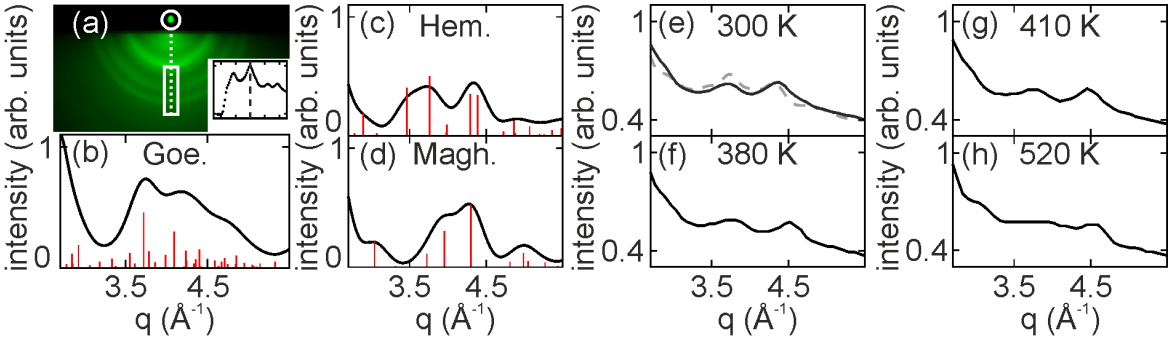

FIG. 5.2: (a) RHEED pattern as of goethite nanoparticles on SiO_x. The white circle indicates the direct beam, the dashed white line the full line profile corresponding to the inset, and the white rectangle the part where the RHEED curves are extracted. (b)-(d) Calculated powder diffraction patterns for goethite, hematite, and maghemite obtained from kinematic diffraction theory. (e) - (h) The line profiles as extracted from the RHEED data recorded at 300 K, 380 K, 410 K, and 520 K, respectively. The dashed gray line in (e) displays a fit t the data, where the simulated RHEED curves of goethite, hematite, and maghemite are superimposed as discussed in the text.

$\beta_{\mathrm{tot}} = \sqrt{\beta_{\mathrm{inst}}^2 + \beta_{\mathrm{grain}}^2} = (2.7 \pm 0.2) \times 10^{-3}\,\mathrm{rad}$, with an instrumental broadening calculated from the lateral broadening of the direct beam $\beta_{\mathrm{inst}} = (2.2 \pm 0.12) \times 10^{-3}\,\mathrm{rad}$ and the broadening due to the grain size $\beta_{\mathrm{grain}} = (1.5 \pm 0.07) \times 10^{-3}\,\mathrm{rad}$ as calculated from the XRD data applying the Scherrer equation. The errors result from the Gaussian fit of the width of the (101) peak of the experimentally obtained XRD curve in Fig. 5.1(d). The simulated powder diffraction curves are displayed as the black lines in Figs. 5.2(b)-(d). When comparing the experimental curves to the simulated curve a only a relatively weak match is found. If a mixture of goethite, hematite, and maghemite is taken into account a better agreement is found. A function $I_{fit}(q) = a \cdot I_{goe}(q) + b \cdot I_{hem}(q) + c \cdot I_{magh}(q) + d \cdot q^2 + e \cdot q + f$ is fitted to the experimental data with a, b, and c the amplitude parameters and d, e, and f the parameters of a polynomial background. A similar polynomial fit has been applied by Bartling *et al.* [164] in previous RHEED study on CoO nanoparticles. The fit yields the gray dashed line in Fig. 5.2(e).

From the fitted amplitudes relative weights for goethite, hematite, and maghemite are obtained as $\mathrm{w_{goe}} = 0.43 \pm 0.04$, $\mathrm{w_{hem}} = 0.29 \pm 0.03$, and $\mathrm{w_{magh}} = 0.28 \pm 0.02$. However, as discussed later a maghemite contribution is unlikely since no trace of maghemite is detected in the XA spectra. Yet, a mixed goethite-hematite phase is compatible with the XA spectra but still contrasts the XRD measurements in Fig. 5.1(d) where the nan-

oparticles are found to consist of pure goethite. A possible explanation could be that the RHEED measurements are done in UHV. Goethite is likely to loose excess surface water, oxygen, and hydroxyl groups in UHV which might cause a restructuring in the surface near region of the nanoparticles.

Another possible reason for the discrepancies between the simulated and experimental RHEED curves might be that the simulation assumes a fully randomized sample. However, as shown later by means of the SEM micrographs the a-axis of the nanoparticles are oriented parallel to the surface of the substrate and thus do not present a randomized sample. It is well known that preferred orientations have impact on the intensity and texture of electron diffraction patterns [165]. Hence, it is expected that the preferred orientation of the goethite nanoparticles with their long axis parallel to the surface lead to significant deviations from the calculated powder diffraction curves. However, the high background and the broadening (β_{inst} and β_{grain}) prevent to resolve the individual diffraction rings. This also limits the possibility to apply Rietveld refinement tools. Attemps to perform synchrotron and laboratory x-ray diffraction on similar samples were not successful due to the low signal.[3]

Yet, RHEED is used to detect relative changes of the curves when increasing the temperature in order to follow possible structural phase transitions of the nanoparticles. In Figs. 5.2(e)-(g) the RHEED curves while increasing the temperature stepwise from 300 K to 410 K are shown. No significant change of the RHEED curves is observed in this temperature range besides a slight shift to higher q-values. The shift likely arises due improper readjustment of the diffractometer during the thermal expansion of the sample. This suggests that no structural phase transition happens between 300 K and the Néel temperature (400 K) of goethite in its bulk form. The experimental RHEED curves start to change significantly as the sample is heated to 520 K. The change of the diffraction curve persists when the sample is cooled down to 300 K. This data shows that the goethite nanoparticles undergo a irreversible change starting at 520 K. This observation can be compared to previous literature, where the beginning of a structural phase transition

[3]Similar samples as in the RHEED experiments have been investigated by means of lab and synchrotron based x-ray diffraction. However, the signal has not been large enough in order to conclude anything. I kindly acknowledge Dr. N. Casati (PSI), P. Pzepka (ETHZ), A. Beck (PSI), and Zimmermann (PSI) for their help with the XRD measurements and helpful discussions.

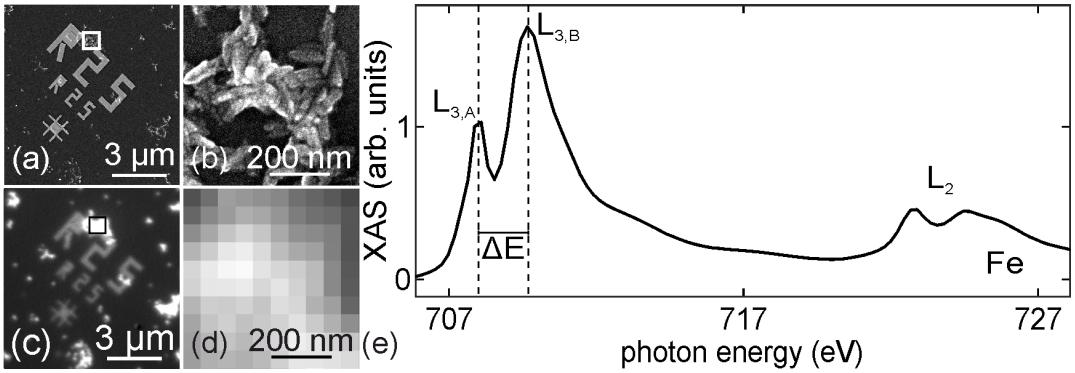

FIG. 5.3: (a) SEM image and (c) XPEEM image of the very same spot on a silicon substrate with gold markers. The white/black squares display the areas which are shown in (b) and (d), respectively. (e) XA spectrum of agglomerated goethite nanoparticles. The spectrum is averaged over 10 agglomerates and the two linear polarizations. $R = I(E_{L_{3,A}})/I(E_{L_{3,B}})$ and $\Delta E = E_{L_{3,B}} - E_{L_{3,A}}$ are indicated in (e) as they are defined in the text.

from goethite to hematite was found to be set on around the same temperature by means of in-situ synchrotron XRD measurements at ambient conditions [96]. The same transition temperature has been further found using thermogravimetry [95, 152].

5.1.2 XPEEM and SEM

Further the chemical properties and morphologies of goethite nanoparticles are studied by means of XPEEM and SEM, respectively. Figs. 5.3(a) and (c) display a SEM micrograph and a XPEEM elemental contrast image recorded at the Fe L_3 edge of the very same spot. The white/black squares highlight the area on the sample which is enlarged in Figs. 5.3(b) and (d). Those micrographs demonstrate the capability to identify the very same features in consecutive microscopy measurements. The SEM images show that the goethite nanoparticles orient their long axis parallel the substrate. According to previous reports the long axis of goethite nanoparticles in this size range usually corresponds to the crystals a-axis [86, 87]. In order to characterize the chemical state of the goethite nanoparticles under UHV conditions XA spectra are recorded. Figure 5.3(e) shows the XA spectrum averaged over 10 agglomerates. The XA spectra recorded with $\mathbf{E}_{\parallel}$ and $\mathbf{E}_{\perp}$ polarized x-rays are also averaged. In order to obtain an isotropic XA spectrum which contains predominantly chemical information. The two main features at the Fe L_3 edge are indicated as $L_{3,A}$ and $L_{3,B}$ (vertical dashed lines). The two features at photon

	R	ΔE(eV)
Goethite ($\alpha - FeOOH$)	0.52 ± 0.04	1.54 ± 0.02
Hematite ($\alpha - Fe_2O_3$)	0.66 ± 0.06	1.52 ± 0.06
Maghemite ($\gamma - Fe_2O_3$)	0.55 ± 0.07	1.43 ± 0.06
Magnetite (Fe_3O_4)	0.72 ± 0.04	1.14 ± 0.04
as prepared sample	0.58 ± 0.02[1]	1.52 ± 0.01
thermally treated sample	0.65 ± 0.02[1]	1.52 ± 0.01

Table 5.1: Typical R and ΔE values reported by van der Heyden et al. [166] [1] Marked values refer actually to R*-values as discussed in the text.

energies $E_{L_{3,A}}$ =709 eV and $E_{L_{3,B}}$ =710.5 eV are used to define $R = I(E_{L_{3,A}})/I(E_{L_{3,B}})$ and $\Delta E = E_{L_{3,B}} - E_{L_{3,A}}$, which are often used to assess the chemical state of iron oxides [166–170]. According to literature R is very sensitive to the crystal field and ΔE to the oxidation state of the material.

In Tab. 5.1 values for R and ΔE as reported by von der Heyden *et al.* [166] are shown. The *as prepared* sample[4] has a R=0.58 and a $\Delta E = 1.52$eV suggesting a mixed phase of goethite and hematite according to Tab. 5.1. However, it is important to note that the measurements by von der Heyden *et al.* [166] are carried out by means of STXM measuring directly the photon absorption in transmission. In contrast XPEEM measurements detect the secondary electrons, which are released upon x-ray excitation, which have a finite electron escape depth λ_e. In case of hematite the escape depth is λ_e=35 Å [171, 172]. As shown in Ref. [172] the detection of secondary electrons suffer from saturation effects, which result in a deviation of the detected electron intensity from the expected photoabsorption cross section. In general, the effect leads to an attenuation

[4]XA and XLD measurements are performed on an *as prepared sample*, which is used for the temperature dependent measurements and on a sample which has been thermally treated up to 460 K in UHV prior to the measurements was used for the orientation dependent measurements. The thermal treated was done to get rid of potential residues of the solvent. The impact of the thermal cycling is discussed later in this thesis. Both samples are prepared according to the procedure described in Chap. 4.1.3.

of features with higher intensity, such as absorption peaks.While saturation effects can be easily corrected in thin films or bulk data with the help of analytic expressions [173], the correction of nanoparticle data requires numerical simulations as discussed in Refs. [174, 175]. The STXM data by von der Heyden *et al.* [166] are not affected by saturation effects. In order to compare the XA spectra obtained by XPEEM it is necessary to simulate the impact of saturation effects. Figure 5.4(a) shows the XA spectra as reported by von der Heyden *et al.*, which are fitted by scaling and subtraction a linear background to the data of agglomerated goethite nanoparticles. Without considering saturation effects the measured spectrum of the goethite nanoparticles match quite well with the reported XA spectrum of hematite. In order to estimate the impact of saturation effects the correction factors reported in Ref. [175] for the escape depth λ_e =22 Å and spherical nanoparticles with a diameter of 30 nm is assumed and applied them to the the XA spectra of hematite and goethite as reported by von der Heyden *et al.*. The results reveal that the goethite XA spectrum matches better when compared to the hematite spectrum with the data obtained by XPEEM.

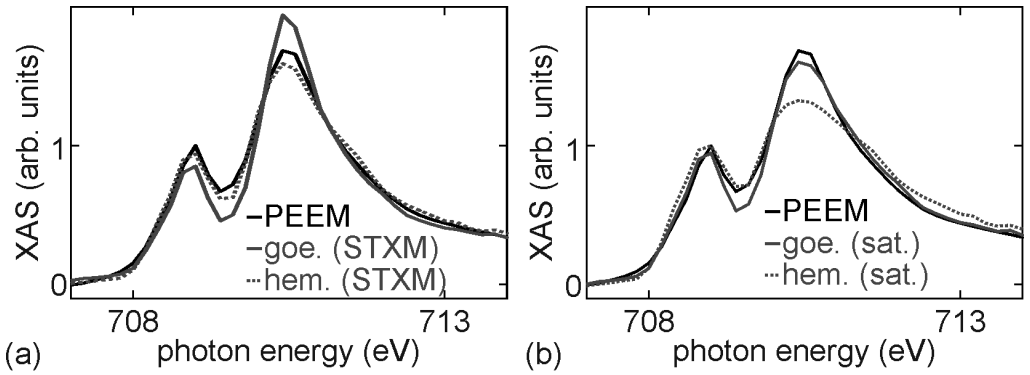

FIG. 5.4: (a) XA spectra obtained from XPEEM (black), XA spectrum of goethite (solid gray), and hematite (dashed gray) as obtained from the STXM measurements reported by von der Heyden *et al.* [166]. In (b) the saturation effects on the XA spectra of goethite (solid gray) and hematite (dashed gray) are simulated assuming a electron escape depth λ_e= 22 Å and a diameter of the nanoparticles of 30 nm

.

Here, it is noted that λ_e for goethite is not known, but might be close to that of hematite. The saturation effects decrease the relative intensities of the A and B feature and thus increase R. Hence, the goethite nanoparticles would exhibit a lower R-value in the absence of saturation effects. As seen in Tab. 5.1 the R-value found by von der Heyden

et al. for goethite is about 0.52 while in our experiments a R of 0.58 for an *as prepared* sample is found. Thus, it is likely that the nanoparticles contain a dominant of goethite. Although, the presence of hematite in the surface near region as indicated by the RHEED measurements can not be excluded. Although, the saturation effects make it difficult to compare our data directly to the reference data reported by von der Heyden *et al.* the R-values are later used to monitor the chemical stability of the nanoparticles over time. To indicate that those values suffer from saturation effects the ratio $I_{L_{3,A}}/I_{L_{3,B}}$ is denoted as R*.

5.2 XLD of agglomerated nanoparticles at room temperature

Figure 5.5(a) displays XA spectra recorded using $\mathbf{E}_\perp$ (black) and $\mathbf{E}_\parallel$ (red) averaged over the 10 agglomerates. The spectra reveal differences in the absorption at the $L_{2,3}$ indicating the presence of a resulting XLD. Figure 5.5(b) displays the normalized XLD of the then agglomerates obtained as $\mathrm{I_{XLD}} = (\mathrm{I_{E_\parallel}} - \mathrm{I_{E_\perp}})/(\mathrm{I_{E_\parallel}} + \mathrm{I_{E_\perp}})$. The shape of the spectrum is is consistent with other reported XLD spectra of Fe^{3+} containing materials such as hematite and $LaFeO_3$ [176–178]. The maximal amplitude of the XLD for the goethite nanoparticles is about 3.1% at the L_3 and 1.9% at the L_2 edge. This corresponds to a reduction by about a factor of two when compared to results obtained for hematite [177] and $LaFeO_3$ [32, 176] where the amplitudes have been reported to be around 7% and 4% at the L_3 and

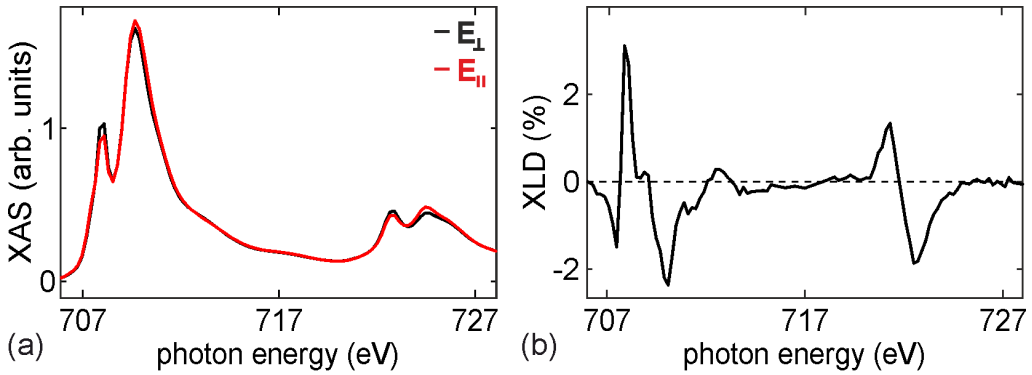

FIG. 5.5: (a) XA spectra recorded at $\mathbf{E}_\perp$ (black) and $\mathbf{E}_\parallel$ at the Fe $L_{2,3}$ edges of the same agglomerates as shown in Fig. 5.3(e). (b) The corresponding XLD spectrum.

L_2 edges, respectively. As discussed in Chap. 3.4 the XLD contains a structural (XNLD) and a magnetic contribution (XMLD). The reduction of the XLD signal of goethite could be linked magnetic moments at the surface of the nanoparticles, which display a different orientation as the spin axis of the nanoparticles as previously reported [179].

The discussion is begun with the structural contribution (XNLD). Considering the orthorhombic cell of goethite the occurrence of an XNLD is expected to arise for individual nanoparticles. The SEM images in Fig. 5.3 (b) show that the goethite nanoparticles orient their elongated axis parallel to the surface of the sample, which is the a-axis of the nanoparticles [87]. As a result the electron density along the a-axis is predominantly probed by $\mathbf{E}_{\parallel}$ while being very weakly probed by $\mathbf{E}_{\perp}$ due to the gracing incidence of the x-rays. Thus, the appearance of the XLD only based on the XNLD can be explained. At this point it is not yet obvious if the XLD contains additionally a magnetic contribution. This issue will be discussed in the following chapter first regarding temperature and orientation dependent XLD spectromicroscopy on agglomerated nanoparticles. Later the orientation dependent XLD of individual goethite nanoparticles will be discussed and compared to the findings of the agglomerated nanoparticles. The comparison of the two cases finally will aim to understand the magnetic structure of agglomerated and individual goethite nanoparticles.

5.3 Temperature and orientation dependent XLD of agglomerated goethite nanoparticles

Next the magnetic contribution to the XLD of agglomerated goethite nanoparticles is addressed by means of temperature dependent XLD spectroscopy. The XMLD is expected to be significantly reduced when approaching and vanishes above T_N of a antiferromagnetic material [18, 32, 37, 177, 178]. T_N of goethite in its bulk form is usually around 400 K [98]. Thus, goethite nanoparticle sample is thermally cycled from 300 K to 410 K and back in order to investigate the magnetic contribution to the XLD. Figure 5.6(a) shows the XA spectra of the sample recorded with $\mathbf{E}_{\parallel}$ (red) and $\mathbf{E}_{\perp}$ (black) polarized x-rays. The resulting XLD spectra are shown in Fig. 5.6(b)-(d). The black dots refer to the experimental data while the red lines are a phenomenological fit to guide to the eye.

The error bars correspond to the statistical error of the XA measurements and are fully propagated.

The spectrum significantly changes as the sample is heated from 300 K to 410 K. The largest change occurs at the second peak located at 709 eV which is indicated with a red arrow. The amplitude of the peak collapses upon heating from initially 3.2 % to 1.7 %. As soon as the sample is brought back to 300 K the magnitude of the peak returns to about 3.2 %. Additionally, the amplitude of the peak centered around 710 eV changes its amplitude. While the peak at 709 eV decreases the one at 710 eV increases indicating an opposite XMLD sign. As discussed above the RHEED data indicates no structural phase transition between 300 K and 410 K in agreement with the literature [96]. Thus the change of the XLD spectra is attributed to the magnetic phase transition from the antiferromagnetically ordered to the paramagnetic phase in the goethite nanoparticles [32, 80, 177, 178] and thus the peak at 709 eV is referred to as the magnetic peak in the following. Moreover the presence of a finite XMLD contribution in the agglomerates shows that the spin axes are not be fully randomly oriented in the agglomerates, since the signal would vanish for randomly oriented spin axis [131].

In order to determine the preferred spin axis of the agglomerates the orientation dependence of the XLD is investigated. The orientation dependence of the XLD is studied rotating the sample around the surface normal by an angle Φ_s as indicated in Fig. 4.3(a). The sample is rotated from Φ_s=0 ° to 90 ° in steps of 30 °. The results are shown in Fig. 5.6(e)-(h). In particular the behavior of the magnetic peak is studied upon the rotation. The magnetic peak is almost unchanged at all measured angles. This indicates that the spin axis cannot be oriented fully random. However, at this point it is not yet clear if the preferential orientation is perpendicular or parallel to the sample plane. This issue will be further addressed later on by studying the orientation dependent XLD of individual goethite nanoparticles (c.f. Chap. 5.4). Further, small fluctuations at the other feature of the XLD spectra can be observed (black arrows). Those variation might arise from a not fully randomized orientation in plane, which could be a consequence of the deposition process of the nanoparticles by spin coating. In first approximation the nanoparticles are spread on the substrate radially. However, it can be imagined that the drop placed on the substrate has not been placed fully in the center of rotation or that the substrate has not

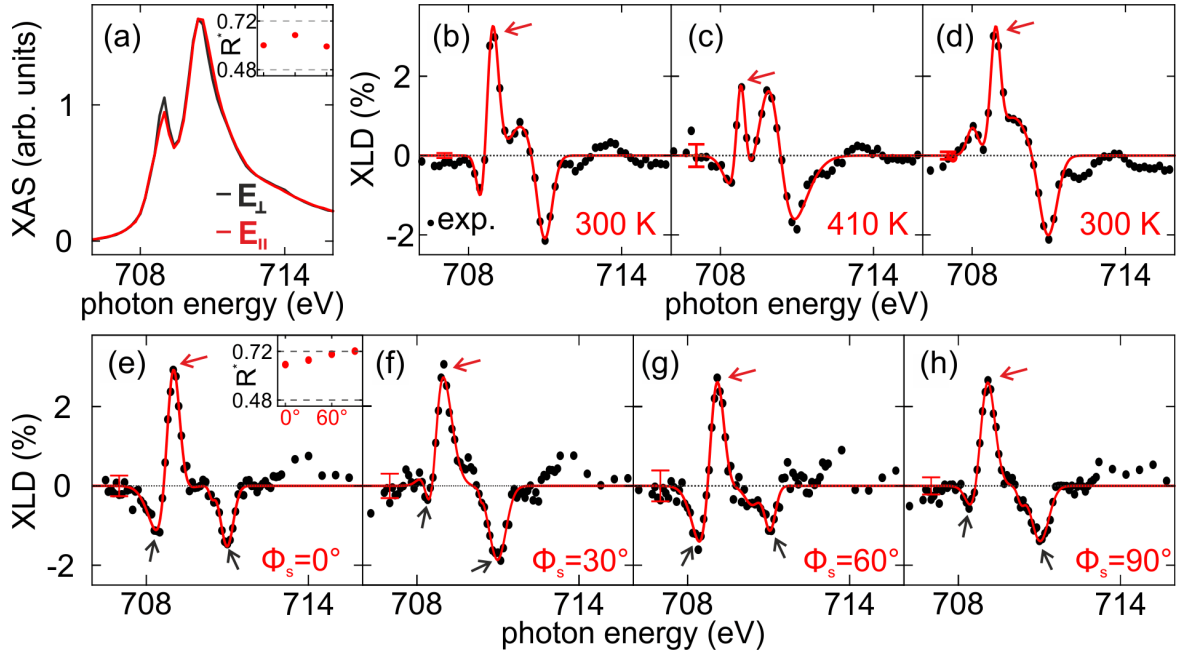

FIG. 5.6: (a) XA spectra recorded with $\mathbf{E}_{\parallel}$ (red) and $\mathbf{E}_{\perp}$ (black) polarized x-rays. (b) - (d) XLD spectra of an *as prepared* sample, at 410 K, and again at 300 K after cycling the temperature. (e) - (h) Results of the measurements at various azimuthal angles from Φ_s =0-90 °. Experimental XLD data in (b)-(h) are represented by the black dots while the solid colored line acting as a guide to the eye. The insets in (a) and (e) display the change of R^* during the respective experiments. The two experiments are performed on two separate samples with different thermal histories. The dashed gray lines in the insets refer to the lower value of goethite and the upper value of hematite as found by von der Heyden *et al.* [166]. All spectra shown here are averages of ten agglomerates.

been placed perfectly in the center of rotation. Thus, the deposition of the nanoparticles is not radially anymore but would become dependent of the position of the substrate, which could give rise to a local preferential orientation of the nanoparticles. This would probably give rise to a weak orientation dependence of the XLD.

The results of the temperature and orientation dependent measurements indicate a magnetic phase transition from the antiferromagnetic to the paramagnetic phase in the nanoparticles close to T_N of goethite in its bulk phase. Further, evidence is found that the goethite nanoparticles preferentially display a preferential orientation either perpendicular or parallel to the SiO_x substrate.

Lastly the chemical stability of the nanoparticles during the measurements is assessed monitoring the R*-values. First, it is noted that the ΔE-value constant for both samples. Thus, a transformation of Fe^{3+} ions Fe^{2+} ions in the goethite nanoparticles is not expected

to happen. The insets in Fig.5.6(a) and (e) illustrate the changes of the R*-values. The agglomerates used for the temperature dependent measurements display a change of R* at 410 K which might be connected to the magnetic phase transition. But the measurements before and after heating the goethite nanoparticles clearly indicate that no significant chemical change happen over the 30 hours the experiment took. In contrast the R*-value in the orientation dependent measurements steadily increases. This is understood as the loss of water, oxygen, or hydroxyl groups of the goethite nanoparticles in their surface near region due to the UHV. According to the XLD measurements the changes are small enough in order not to change the magnetic properties of the nanoparticles significantly, since the XLD signal is not significantly decreased over time.

5.4 Orientation dependent XLD of individual goethite nanoparticles

The XLD in Chap. 5.3 is found to exhibit a magnetic (XMLD) and a structural contribution (XNLD). Specifically the nanoparticles on the SiO_x substrate have a preferential crystallographic orientation parallel to the substrate and a significant component perpendicular to the substrate of the spin axis. The properties of individual goethite nanoparticles are discussed in the following by means of XLD spectromicroscopy. XPEEM and SEM are combined in order to compare the azimuthal dependence of the XLD with the morphology of the individual goethite nanoparticles. This part of the study aims to understand the XNLD and XMLD contribution in more depth and tries to determine the orientation of the spin axis of isolated nanoparticles and compare then to the orientation of the spin axis of the agglomerated goethite nanoparticles. Here it shall be noted that the azimuthal dependence of the agglomerated and individual goethite nanoparticles are recorded during the very same experiment. Thus, the experimental conditions are identical and the results directly comparable.

Figures 5.7(a) and (f) display the XA spectra recorded using $\mathbf{E}_{\parallel}$ (red) and $\mathbf{E}_{\perp}$ (black) polarized x-rays at $\Phi_s = 0\,^\circ$ and the insets show the SEM micrograph of the respective individual goethite nanoparticles with the propagation direction of the x-rays (white arrow) and the direction of $\mathbf{E}_{\parallel}$ indicated. While the nanoparticle in (a) has its a-axis oriented

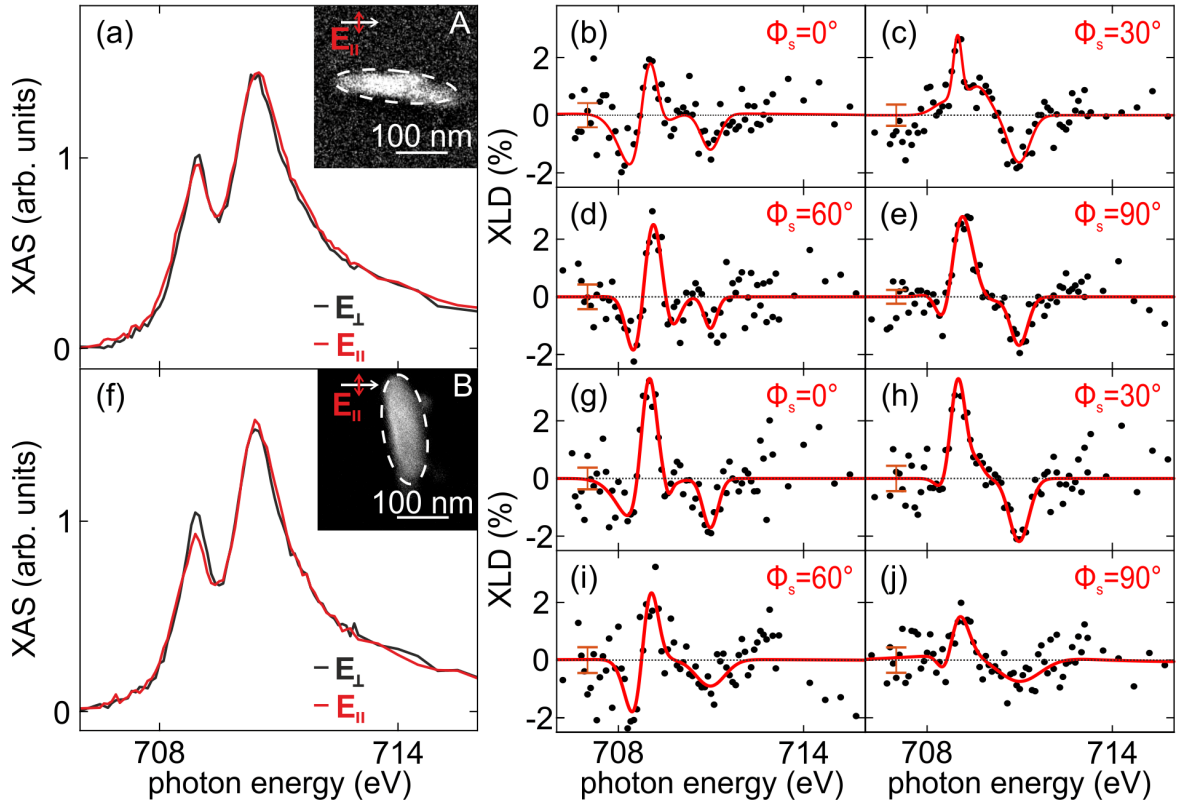

FIG. 5.7: (a) and (f) XA spectra of the individual goethite nanoparticles shown in the inset recorded at $\mathbf{E}_{\parallel}$ (red) and $\mathbf{E}_{\perp}$ (black) polarization. The individual nanoparticles in (a) is elongated along $\mathbf{k}$ while the nanoparticle in (f) is elongated along $\mathbf{E}_{\parallel}$ at $\Phi_s = 0\,^\circ$. (b) - (e) and (g) - (j) XLD spectra for four azimuthal rotation angles for the respective nanoparticles. The black dots correspond to the experimental data and the red line is a guide to the eye indicating the spectral shape.

perpendicular to $\mathbf{E}_{\parallel}$ the nanoparticle in (f) has its a-axis parallel to $\mathbf{E}_{\parallel}$ at $\Phi_s = 0\,^\circ$. The two nanoparticles are referred as NP A and NP B as indicated in Figs. 5.7(a) and (f), respectively. Comparing the XA spectra reveals that the difference at $L_{3,A}$ feature is significantly lower for NP A than NP B. At this point it could be speculated that this difference might arise since the a-axis is not effectively screened for the NP A, while the screening is close to being maximized for NP B at $\Phi_s = 0\,^\circ$.

Further evidence for this is found comparing pairwise the XLD spectra in displayed in (b) and (j) as well as in (e) and (g). The XLD spectra in (b) and (j) results if the a-axis of NP A and NP B are perpendicular to $\mathbf{E}_{\parallel}$. In this situation the a-axis is almost not screened by the x-rays. In both cases the magnetic peak has a relatively low intensity. In contrast, the structurally dominated features are quite different. The very same trend is found when comparing the XLD spectra in (e) and (g) when the a-axis is parallel to $\mathbf{E}_{\parallel}$

and thus is strongly screened. The height of the magnetic peaks for both nanoparticles is more or less the same, while there are also some differences in the structural peaks. It is likely that the differences of the structurally dominated features arise from the relative orientation of the $b-c$-plane within the cross section of the nanoparticles.

In principle it should be possible to form similar pairs for the measurements at Φ_s =30 °,60 °. Due to the symmetry it would expected that the XLD spectrum on NP A at 30 ° is very similar to the XLD spectrum of NP B a 60 ° and vice versa. However, besides the generally similar amplitudes of the magnetic peaks no similarities are found. Actually, it seems like the two XLD spectra at 30°[(c) and (h)] and 60°[(d) and (i)] exhibit more similarities. This behavior can be attributed to the relative orientation of the $b-c$-planes of the two nanoparticles, which are not precisely known.

As a last note it is found that the XLD spectra of both individual goethite nanoparticles indicate a 60 ° symmetry since the (b) and (d) as well as (c) and (e) for NP A and consequently (g) and (i) look very similar considering the structurally dominated features. In contrast, the XLD spectra for particle B at 30 ° and 90 ° do not share much similarities. Although, it is observed that R* of NP A is over the whole experiment around 0.67, while R* of continuously increases from initially 0.66 to 0.76 in the end of the measurements. This observation suggests that NP B suffers of a chemical degeneration during the experiment. However, the decrease of the XLD signal between Figs. 5.7(g) and (j) cannot be fully attributed to the chemical change, since in this case the increase in R* would be reflected in a continuous decrease of the XLD signal, which is not indicated since the amplitudes of Figs. 5.7(g)-(i) appear to be relatively consistent.

The observations suggest that the azimuthal changes in the XLD spectra of individual goethite nanoparticles are dominated by the structural contribution, which in fact is present on all the XLD features while the magnetic contribution seems to be strongly linked to the feature centered at 709 eV and 710.5 eV. Thus, it is concluded that the magnetic contribution in individual goethite nanoparticles is almost uniform with respect to the azimuthal orientation of the nanoparticles. It is observed additionally that the maximal amplitude of the magnetic peak are almost the same for individual and agglomerated goethite nanoparticles. Since the azimuthal dependence of the XLD of goethite nanoparticles has been more closely studied in this chapter, the next chapter will focus

on discussing the spin axes of the individual nanoparticles.

5.5 Spin axes of individual goethite nanoparticles on a silicon support

The experimental data for the agglomerated nanoparticles (c.f. Fig. 5.6) and the individual goethite nanoparticles (c.f. Fig. 5.7) suggest that the magnetic contribution to the XLD is largely invariant, if the sample is rotated around the surface normal. Such a rotation can only leave **S** unaffected, if **S** nearly perpendicular to the sample. This is unexpected, since one would not expect that nanoparticles distributed from a solution by means of spin coating would exhibit a strong preferential orientation of the spin axis. Further, the XLD spectra of individual goethite nanoparticles suggest a non-uniform orientation of the *b*- and *c*-axes on the sample. Figure 5.8(a) - (c) display three scenarios in order to explain the findings. Figure 5.8(a) shows the case, where the nanoparticles preferentially adhere with one of their (101) facets to the substrate such that the *b*-direction is oriented perpendicular to the sample plane. Since the spin axis if found parallel to the *b*-axis [89, 93, 98] this could explain an spin axis orientation perpendicular to the sample. However, considering that the nanoparticles are covered with a organic surfactant (c.f. Chap. 4.1.1) a strict orientation with the (101) or (001) facets seems unlikely. Further the random distribution of the nanoparticles on the substrates makes such an attachment rather unlikely. Finally, the data for the individual goethite nanoparticles also do not suggest a strong preferential orientation of the nanoparticles along their (101) facets on

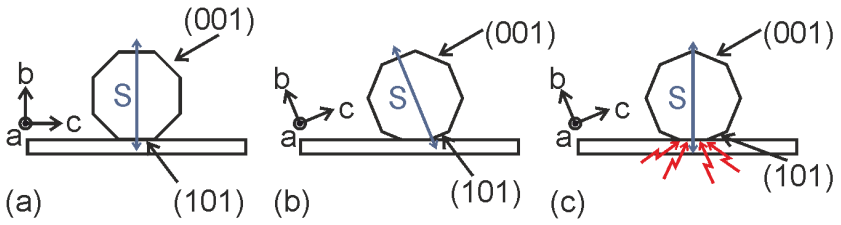

FIG. 5.8: (a) Model where the b-axis and the spin axis are perpendicular to the substrate. (b) and (c) the b axis of the nanoparticle is not perpendicular to the substrate. Thus in (b) the spin axis is contains an in-plane component where in (c) the spin axis is perpendicular to the substrate due to a changed magnetic anisotropy arising from an interface effect at the interface between the goethite nanoparticles and the SiO_x substrate.

the substrate.

Figure 5.8(b) illustrates a situation where the *b*-axis and thus **S** can be tilted to a certain extend from the surface normal. In this scenario one would expect depending on the projection of **S** along the sample plane, that the at least the individual nanoparticles would exhibit an orientation dependent XMLD contribution. Considering that the spin axis contain a significant contribution parallel to the sample plane, one would expect that the XMLD amplitude of the agglomerates would be significantly reduced compared to the maximal amplitude of the individual goethite nanoparticles. However, such a significant decrease of the XLD amplitudes can not be observed in the data. Thus, it seems very likely that if the spin axis can only be tilted by small angles from the surface normal.

Thus, the data suggests that the spin axis are almost perpendicular to the sample. It is not intrinsically clear why randomly distributed goethite nanoparticles should display this behavior. Figure 5.8(c) shows a model, where the nanoparticles do not exhibit a preferential orientation of the *b*- and *c*-axis with respect to the substrate. However, the red arrows shall indicate the presence of van der Waals force or interfacial strain at the interface between the nanoparticles and the substrate. Such forces could reorient the spin axis perpendicular to the sample as it was demonstrated for $LaFeO_3$ thin films [37] as well as for ferromagnetic clusters on substrates [180, 181]. This model is further supported by the observation, that the spin axis of goethite nanoparticles can relatively easily be rotated from the *b*-axis into the *c*-axis [71, 72]. Thus, the results presented here could for the first time indicate the crucial impact of nanoparticle-interface interactions on the antiferromagnetic properties of nanoparticles deposited on substrates.

5.6 Conclusion

The structural, morphological, chemical, and magnetic properties of goethite nanoparticles on SiO_x substrate are studied by means of XRD, RHEED, SEM, TEM, spatially resolved XA spectroscopy, and temperature and orientation dependent XLD spectromicroscopy. The XRD measurements reveal that the nanoparticles in solution consist of pure goethite without indication of any other phases such as hematite. In contrast to this the RHEED measurements suggest that the goethite nanoparticles might change their chemical state

upon insertion into UHV conditions and develop a certain hematite character due to the loss of hydroxyl groups and water at the surface of the nanoparticles. Similar indications are found using XA spectroscopy. Further, thermal cycling goethite nanoparticles up to about 460 K can decrease the chemical stability significantly. Thus, it is of crucial importance to know the thermal history of goethite nanoparticle samples in order to properly interpret experimental data.

The nanoparticles exhibit a acicular morphology similar to other reports in the literature [67, 72, 86, 87, 89]. Further, high resolution TEM data reveal a significant amount of defects and voids in the nanoparticles such as for example low angle grain boundaries. However, it can not be excluded that some of the found voids might arise due to damages during the TEM measurements.

The XLD investigations of the nanoparticles indicate that agglomerated goethite nanoparticles display a certain preferential orientation. This is in contrast to the RHEED measurements where textureless Laue rings are found indicating no preferential orientation of the nanoparticles. However, this instance is mostly attributed to the limited resolution of the RHEED instrument in combination with the relatively complex diffraction pattern goethite exhibits. Further the presence of a preferential orientation is found using SEM, where the nanoparticles predominantly orient their long axis parallel to the sample plane. Commonly, goethite nanoparticles are found to be elongated along the crystalline a-axis [86, 98]. Thus, it is reasonable to assume that the a-axis displays a preferential orientation parallel to the sample plane which alone already explains the emergence of an XNLD contribution since only $\mathbf{E}_{\parallel}$ is able to effectively probe the a-axis of the nanoparticles.

The temperature dependence of the XLD is studied by cycling a goethite nanoparticle sample from 300 K to 410 K back to 300 K. It is observed that the XLD spectra of agglomerated nanoparticles reversibly change dominantly at features centered at 709 eV and 710.5 eV. The reversibility of the change in the XLD spectra of the agglomerated nanoparticles is attributed to magnetic phase transition from the antiferromagnetic to the paramagnetic phase as expected to happen around 400 K for goethite in its bulk. Thus, it is indicated that the T_N of the here investigated goethite nanoparticles is close to the Néel temperature of bulk goethite.

The orientation dependent XLD measurements on the agglomerated goethite nan-

oparticles reveals a small anisotropy, which is not yet fully understood. However, as expected the azimuthal dependence of individual goethite nanoparticles is found to be much more pronounced. It is found that the magnetic features centered at 709 eV and 710 eV only show a minor angular dependence while the other features which dominantly arise from the XNLD display a much more pronounce angular dependence. Some evidence is found that the XNLD exhibits a 60 ° symmetry. However, in order to determine the azimuthal dependence of the XNLD one should aim to determine the azimuthal dependence of the XNLD of individual goethite nanoparticles above T_N. Since the XNLD of goethite might display a 60 ° symmetry one would have to measure the XNLD probably in steps of 10-15 °. Finally, combining the observations for individual and agglomerated goethite nanoparticles allows to conclude that the spin axis of the nanoparticles have a tendency to be oriented perpendicular to the substrate. Since no strong preferential orientation of the $b - c$ plane is indicated, it is concluded that the preferential orientation of the spin axis arises from an interface effect which reorients the spin axis of individual goethite nanoparticles.

Chapter 6

Cobalt oxide core shell nanooctahedra on silicon substrates

In the following chapter the results of the investigation of individual CoO/Co_3O_4 core-shell nanooctahedra are discussed. When compared to goethite the Co/Co_3O_4 core-shell nanoparticles have a well defined shape and are terminated by (111) facets. Three particular orientations of the nanoparticles on a TEM substrate were observed [52]. Figure 6.1(a)-(c) show the resulting projections found by TEM. Figure 6.1(a) shows a rhombic, Fig. 6.1(b) a rectangular, and Fig. 6.1(c) a hexagonal shape arising from nanoparticles being oriented with the respective [011], [112], and [111] directions perpendicular to the surface of the substrate [85]. The shapes of the projections are consistent with the nearly ideal octahedra in the same orientations as shown by the yellow schematics in the insets of the figure.

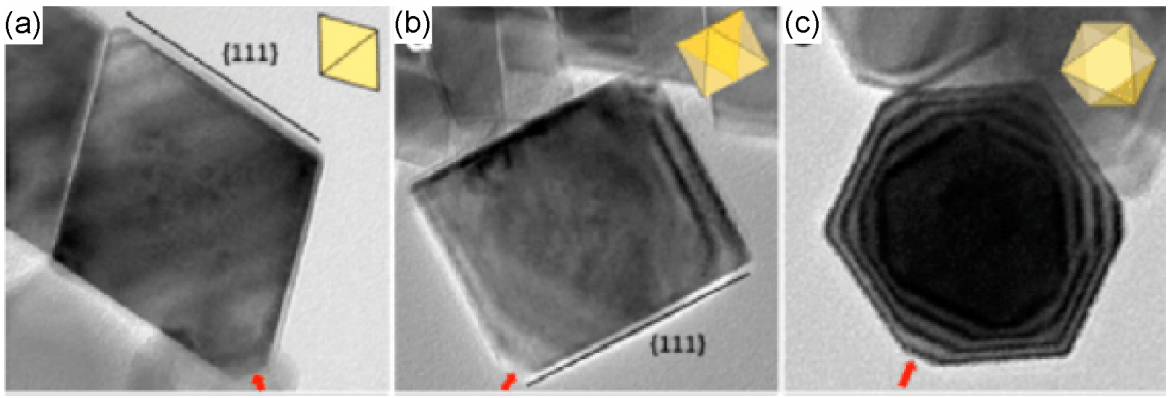

FIG. 6.1: Fontaíña-Troitiño *et al.* reported three possible projections, shown in (a)-(c), which appear for CoO/Co_3O_4 core-shell nanooctahedra on flat TEM membranes. [52].

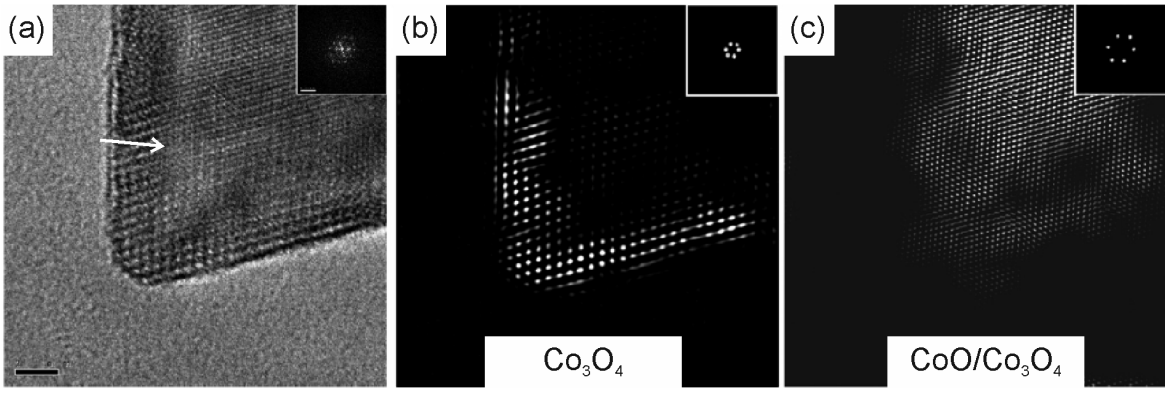

FIG. 6.2: (a) Atomically resolved TEM image of a part of a CoO/Co_3O_4 core-shell nanooctahedra with the phase boundary indicated (white arrow). (b) and (c) show the same image but are Fourier filtered by the lattice constant of Co_3O_4 and once with CoO and Co_3O_4, respectively. Adapted from Fontaíña-Troitiño *et al.* [52]

Figure 6.2(a)-(c) display the core-shell structure of the CoO/Co_3O_4 nanooctahedra [52]. Figure 6.2(a) shows an atomically resolved TEM image with the phase boundary between CoO and Co_3O_4 indicated by the white arrow. Additionally the image has been Fourier filtered by the lattice parameters of Co_3O_4 in Fig. 6.2(b) and by the parameters of CoO and Co_3O_4 in Fig. 6.2(c). These data suggest a clean phase separation of CoO in the core and Co_3O_4 in the shell. While the XRD patterns and electron energy loss spectroscopy (EELS) at the Co $L_{2,3}$ edges display now clear presence of a well crystallized Co_3O_4 shell, some evidence was found by means of EELS at the O K edge.

The magnetic properties of the CoO/Co_3O_4 core-shell nanoparticles were studied using a superconducting quantum interference device (SQUID) and high field DC magnetometry. The Néel temperature of the core of nanoparticles was found regardless the particle size to be around 285 K which is in good agreement with T_N of CoO in its bulk form [17]. But no indications for a magnetic phase transition associated with Co_3O_4 was found down to 5 K. However, the SQUID measurements revealed the presence of magnetically ordered moments which persist up to 400 K well above the Néel temperature of the CoO core. Density functional theory (DFT) calculations suggested that the magnetic moments arise from strain at the Co_3O_4/CoO core-shell interface [85]. However, a number of questions remain unanswered yet. For instance the orientation of the antiferromagnetic spin axis with respect to the crystal lattice was not addressed in Ref. [52]. Further, the role of possible inter-particle interactions in the investigated samples as well as the distribu-

tion of sizes, defects, and their role for the magnetic properties remain unclear. Also whether the observed ferromagnetic moments can be assigned to Co ions and whether the nanoparticles are in a magnetic single domain state. Finally, it is also unclear if the antiferromagnetically ordered spin system of the nanoparticles is magnetically blocked or in a superparamagnetic state at certain temperatures needs to be investigated. Addressing these questions will help to better understand the observed properties of cobalt oxide nanoparticles and will shed further shed light in antiferromagnetism at the nanoscale in general.

The aim of this work is to correlate the chemical, magnetic and morphological properties of individual non-interacting Co_3O_4/CoO core-shell nanooctahedra combining of temperature, orientation, and polarization dependent XA spectromicroscopy by means of XPEEM with SEM. In particular this study aims to determine the spin structure of individual antiferromagnetic CoO nanoparticles. Further, the spin structure (magnetic single- or multi-domain states) of the nanoparticles is addressed. The orientation of the spin axes will be correlated with the crystal axes. These investigations are performed utilizing the XMLD effect which is sensitive to the orientation of the spin axis. In order to investigate the presence of uncompensated magnetic moments in individual nanoparticles the XMCD effect is employed. In this case the element specificity of the XMCD effect will allow to detect if magnetic moments are located at the cobalt ions in the crystal lattice. Additionally, spatially and temporally resolved XMCD contrast imaging in remanence allows to determine if the uncompensated magnetic moments are in a superparamagnetic state or magnetically blocked state. Finally, by combining XMLD and XMCD spectromicroscopy might allow to investigate the relation between the antiferromagnetic spin lattice in the CoO core and the uncompensated magnetic moments. [1]

[1]The CoO/Co_3O_4 core-shell nanooctahedra were provided by M. Testa Anta and Prof. Dr. V. Salgueiriño. Sample were prepared by me. SEM characterization was performed by me, Dr. M. Wyss, and D. Mathys (Nano Imaging Lab, University of Basel). XPEEM characterization was done by me, Dr. T. Savchenko, M. Testa Anta, and Dr. A. Kleibert at the Surface/Interface (SIM) beamline at the Swiss Light Source (SLS). Dr. A. Kleibert contributed the code to fit the XA spectra. Code development and data analysis was done by me.

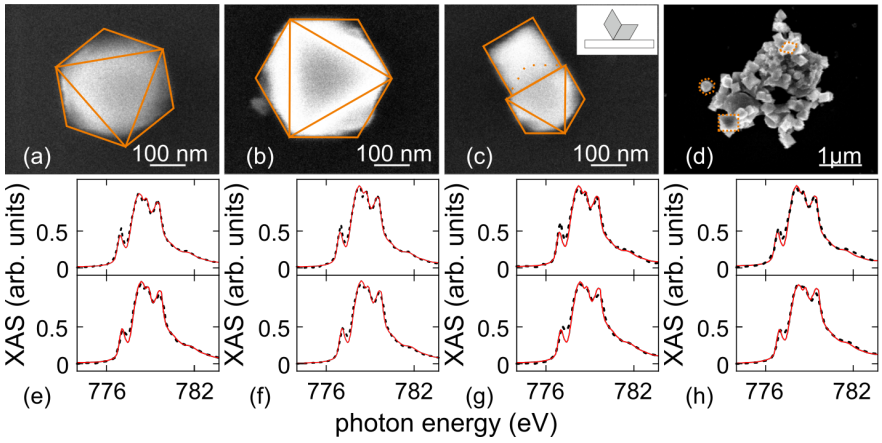

FIG. 6.3: (a) and (b) show the SEM images of two individual CoO nanoparticles, while (c) shows two attached nanoparticles and (d) a agglomerate of CoO nanoparticles. (e) - (h) display the isotropic XA spectra (dashed black line) of the particles in (a) - (d), where the spectrum at the top denotes the state of the *as prepared* sample, while the bottom spectrum refers to the state of the spots after 72 h of continuous x-ray exposure within UHV conditions. Additionally a fits for all spectra (red solid line) are shown in (e) - (h) which are obtained by superimposing a CoO, Co_3O_4, and w – CoO.

6.1 Morphology, chemical properties, and stability of CoO nanooctahedra

Figures. 6.3(a) and (b) show SEM images of two individual nanoparticles. Figure 6.3(c) displays two particles attached to each other, and Fig. 6.3(d) a larger agglomerate of CoO nanoparticles as obtained in SEM. Individual CoO nanoparticles are frequently found with a hexagonal shape. Thus, the energetically favored orientation is achieved if a (111) facet lays flat on the silicon substrate. The orange lines indicate the facets and edges of the nanoparticles. In Fig. 6.3(c) two attached nanoparticles are found. One of them shows a hexagonal shape (lower) and the other a square-like shape. The inset schematically depicts how the two nanoparticles could be attached to each other with their (111) facets. Figure 6.3(d) displays an agglomerate in which essentially all typical projections can be identified (see orange dashed lines). The reason for this is that the nanoparticles in an agglomerate have a large amount of possibilities to attach their respective (111) facets.

In order to assess the chemical composition and stability of the nanoparticles the respective XA spectra (black dashed line) of the four features in Figs. 6.3(a)-(d) are shown in Figs. 6.3(e)-(h). The upper panels show the XA spectra of the first measurements of

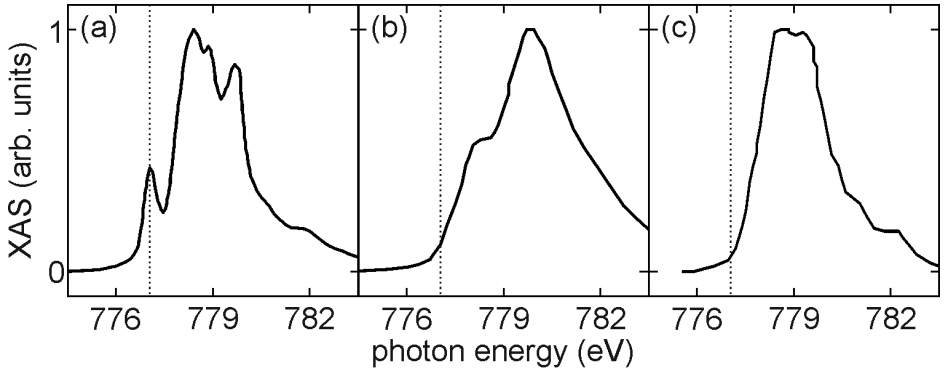

FIG. 6.4: (a)-(c) Reference XA spectra for CoO [172], Co_3O4 [183], and $w-CoO$ [182]. The dashed line in all three panels indicates the energy where the low energy satellite of the CoO spectrum in panel (a) is located.

an *as prepared* sample and the lower panels show the XA spectra after 72 h of continuous measurements. On first glimpse, there are no obvious differences between the individual features nor between the initial and final chemical states. In order to study this more detail the following model $I_{fit}(E) = a \cdot XAS(E)_{CoO} + d \cdot E + e$ is fitted to the experimental data, where a, d, and e the free fit parameters and $XAS(E)_{CoO}$ the reference spectrum as displayed in Fig. 6.4(a), and E the photon energy. The model fits the experimental data very well. Since the nanoparticles are expected to contain a shell of Co_3O_4 and could potentially also contain a $w-CoO$ phase those compounds are also added to the model in a refinement step. $w-CoO$ is also integrated into the fit model since it is known that this phase can be stabilized at the nanoscale. The refined fit model is given as $I_{fit}(E) = a \cdot XAS(E)_{CoO} + b \cdot XAS(E)_{w-CoO} + c \cdot XAS(E)_{Co_3O_4} + d \cdot E + e$, with a, b, and c being the amplitude parameters of the CoO, $w-CoO$, and Co_3O_4, respectively. The parameters d and e correspond to the linear background. The reference spectra for Co_3O_4 and $w-CoO$ are displayed in Fig. 6.4(b) and (c) and the fitted amplitudes for the three compounds are listed in Tab. 6.1. The fits reveal that $w-CoO$ always yields a amplitude of 0 and thus is likely not present in the nanoparticles. Further, in all the initial states the fitted amplitudes of Co_3O_4 is are almost neglectable compared to CoO. After the measurements the fitted amplitudes of Co_3O_4 are generally increased with respect to the CoO amplitudes. Although, this trend seems to reduces for single nanoparticles. Considering, that the Co_3O_4 shell is reported to be 2-4 nm combined with the surface sensitivity of XPEEM with a probing depth of 5-10 nm the contribution of the shell seems

Particle	State	a_{CoO}	a_{Co3O4}	a_{w-CoO}
Fig. 6.3 (a)	initial	1 ± 0.02	0.05 ± 0.02	0
	end	1.02 ± 0.04	0.08 ± 0.02	0
Fig. 6.3 (b)	initial	1.05 ± 0.01	0.01 ± 0.01	0
	end	1.04 ± 0.04	0.06 ± 0.02	0
Fig. 6.3 (c)	initial	1.03 ± 0.02	0.04 ± 0.02	0
	end	0.97 ± 0.05	0.15 ± 0.03	0
Fig. 6.3 (d)	initial	1.02 ± 0.02	0.04 ± 0.02	0
	end	0.9 ± 0.04	0.17 ± 0.03	0

Table 6.1: The amplitude for CoO (a_{CoO}), Co_3O_4 (a_{Co3O4}), and $w - CoO$ (a_{w-CoO}) for the four nanoparticles in Figs. 6.3(a)-(d) are shown here in the initial state and after 72 hours of measurements. The fits are performed using reference spectra of CoO [172], Co_3O_4 [183], and $w - CoO$ [182].

to be to small for the initial as well as the final states. However, this finding is well in line with the reported EELS results at the Co $L_{2,3}$ edges, where also no differences between core and shell regions could be found [52]. This was explained by the presence of a non-stoichiometric and defective shell. The XA data suggests no significant presence of Co species other than octahedrally coordinated Co^{2+} specially in the initial states.

6.2 XMLD of individual CoO nanoparticles

6.2.1 Temperature dependent XMLD spectromicroscopy

Figure 6.5(a) shows the SEM micrograph of an individual CoO nanoparticle referred to as NP A in what follows and (b) the XA spectra recorded at 300 K with $\mathbf{E}_{(\mathbf{90},\mathbf{45})}$ (red) and

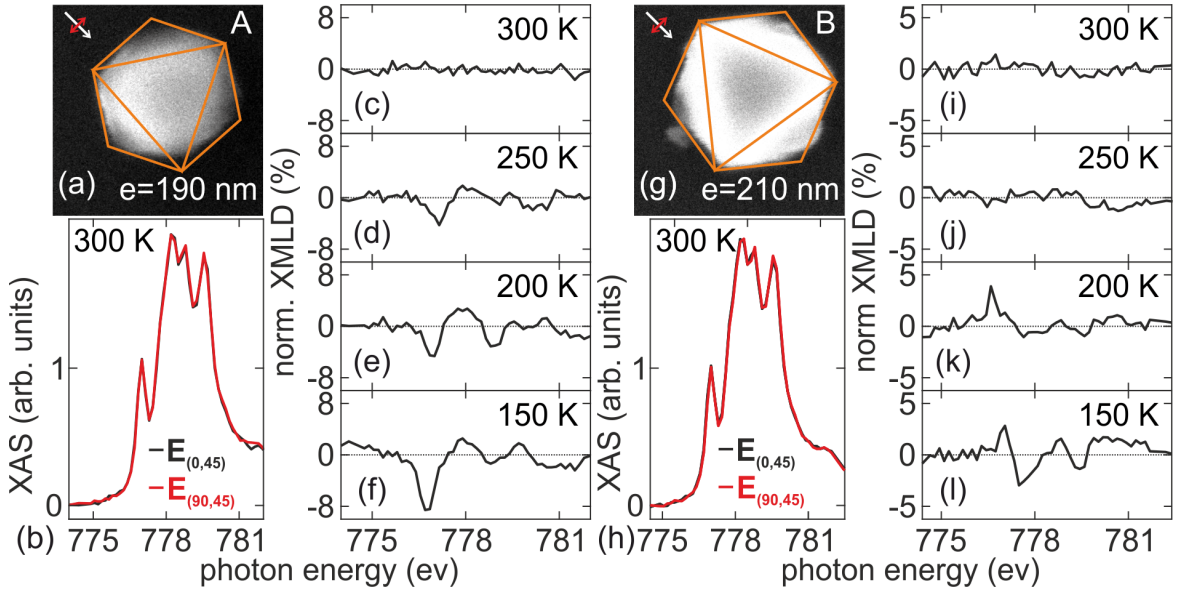

FIG. 6.5: (a) and (g) SEM images two individual nanoparticles, referred to as NP A and NP B in the text, with **k** (white arrow) and $\mathbf{E}_{(90,45)}$ (red arrow) indicated. Further the shape of the nanoparticles and their top facets are highlighted by the orange lines. (b) and (h) XA spectra recorded with $\mathbf{E}_{(90,45)}$ (red) and $\mathbf{E}_{(0,45)}$ (black) at 300 K of NP A and NP B. Further (c)-(f) and (i)-(l) the XMLD spectra at 300 K, 250 K, 200 K, and 150 K for NP A and NP B, respectively.

$\mathbf{E}_{(0,45)}$ (black). The edge length e=190 nm of the octahedron is indicated. In the following the experimental geometry is always according to the scheme discussed in Chap. 4.2.1. Figures 6.5(c)-(f) show the temperature dependent XMLD of NP A. At 300 K no XMLD is found, which is expected since the sample temperature is still above the Néel temperature of CoO in its bulk form. The XMLD spectrum displayed in Fig 6.5(i) of the second individual CoO nanoparticle shown in Fig. 6.5(g) (NP B) is also consistent with this observation. As the temperature is lowered to 250 K a small XMLD effect is observed for NP A while NP B still exhibits no XMLD. In case of NP B the XMLD signal starts arising around 200 K. However, below 250 K and 200 K the magnitude of the XMLD increases for both nanoparticles with decreasing temperature. This is the expected behavior for antiferromagnetic materials below T_N. Thus, it can be concluded that both nanoparticles show a magnetic phase transition from the paramagnetic to the antiferromagnetic state. At this point it seems that the two nanoparticles might exhibit two different magnetic ordering temperatures. However, the observation of different Néel temperatures for the two nanoparticles would be rather unexpected since the two particles have more or less

the same size. Moreover, the data would suggest that the slightly larger NP B exhibits a lower T_N. The amplitude of the XMLD effect for NP A appears to be systematically larger than for NP B. Thus, it seems reasonable to assume that the difference in the temperature dependent behavior arises from the fact that the spin axes of the two nanoparticles are oriented differently with respect to the E-field vectors of the incident x-rays. In order to shed light on this the azimuthal dependence of the XMLD effect on the very same CoO nanoparticles is investigated.

6.2.2 Azimuthal dependent XMLD spectromicroscopy at 100 K

In order to study the orientation of the antiferromagnetic spin axis of individual CoO nanoparticles, the orientation dependence of the XMLD of NP A and NP B is investigated. In Figs. 6.6(a) and (g) the SEM micrographs of NP A and NP B are shown with **k** (white arrow) and $\mathbf{E}_{(\mathbf{90,45})}$ (red arrow) at Φ_s=0 °. When compared to Figs. 6.5(a) and (g) the orientation of the propagation direction and the horizontal polarization vector are now rotated by Φ_s=45 °. The XA absorption spectra of the two CoO nanoparticles recorded with $\mathbf{E}_{(\mathbf{90,45})}$ and $\mathbf{E}_{(\mathbf{0,45})}$ polarized x-rays at 100 K and at a azimuthal angle of Φ_s =45 ° are shown in Figs. 6.6(b) and (h). The orientation dependence of the two CoO nanoparticles is studied rotating the sample stepwise from Φ_s=0 ° to Φ_s =90 °. The XMLD spectra of NP A are displayed in Fig. 6.6(c)-(e). NP A decreases its XMLD signal continuously under a rotation from Φ_s=0 ° to 90 ° and vanishes almost completely at 90 °. The XMLD signal of NP B is large, especially around 777 eV at Φ_s=0 °, vanishes at Φ_s=45 °, and inverts its sign upon a rotation to Φ_s=90 °. This azimuthal dependence suggests that the spin axis of this nanoparticle has a relatively large component in the sample plane. For both nanoparticles a clear XMLD anisotropy with respect to the azimuthal angle is obtained as it has been shown for CoO in its thin film form [30, 31].

The presence of a relatively pronounced orientation dependent XMLD effect for NP A and NP B suggest that the nanoparticles are in a antiferromagnetic single domain state. This is concluded since the largest XMLD amplitudes of both nanoparticles are around 8%, which is in good agreement with XMLD amplitudes of single domain thin films previously measured [184]. If the nanoparticles would exhibit a antiferromagnetic multi domain state it would be expected that the maximum of the experimentally measured XMLD

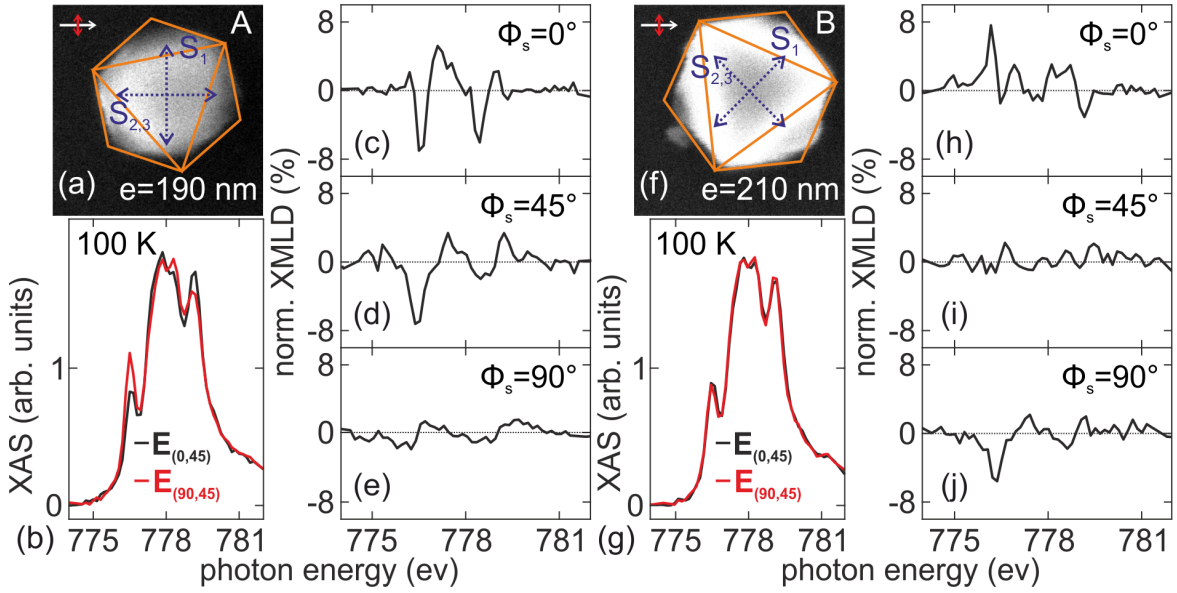

FIG. 6.6: (a) and (g) SEM images of NP A and NP B, respectively. The propagation direction of the x-rays (white arrow) the $\mathbf{E_{(90,45)}}$ (red arrow), the octahedral shape of the nanoparticles (orange lines) are highlighted. (b) and (h) the respective XA spectra at recorded at 100 K with $\mathbf{E_{(0,45)}}$ (black) and $\mathbf{E_{(90,45)}}$ (red) polarized light. (c)-(f) and (i)-(l) show the azimuthal dependent XMLD of NP A and NP B.

amplitudes would be significantly reduced. Additionally, it is observed that the measured XMLD anisotropy with respect to the azimuthal orientation behaves in a seemingly non-continuous way. This behavior is consistent with a single domain state but not necessarily with a multi domain state since in case of a multi domain state one would expect to measure non-continuous changes depending on the orientation the facets, which could exhibit a different orientation of the magnetic moments.

A first assessment of the spin axes is possible by considering the angles at which the XMLD is almost zero. For symmetry reasons the XMLD vanishes if $\mathbf{S} \parallel \mathbf{k}$ or $\mathbf{S} \cdot \mathbf{E_{(0,\Phi_s)}} = \mathbf{S} \cdot \mathbf{E_{(90,\Phi_s)}}$. The second criteria is fulfilled if $\mathbf{S}$ is perpendicular to $\mathbf{k}$ and being titled by 45° out of the sample plane. In this case two non-equivalent spin axis are possible where one is tilted out of the sample plane by +45°and the other by -45°. The symmetry properties of the XMLD are discussed in detail in Ref. [138]. Hence, it is possible to identify three possible spin axis $\mathbf{S_{1-3}}$ which are orthogonal to each other. The in-plane components of the three spin axis for NP A and NP B are shown by the blue dashed arrows. For $\mathbf{S_1}$ is the spin axis is parallel to $\mathbf{k}$ and $\mathbf{S_{2,3}}$ refer to the spin axis perpendicular to $\mathbf{k}$. It is known that the spin axis CoO in its bulk form are along the $[\bar{1}\bar{1}7]$ directions, which are

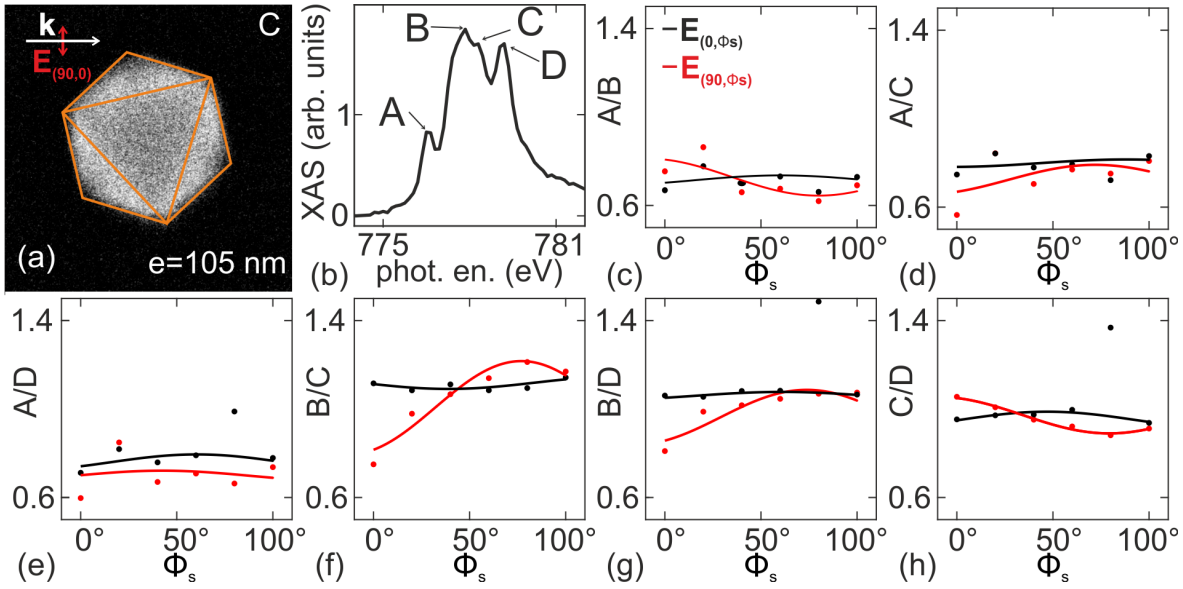

FIG. 6.7: (a) an image of a individual CoO nanoparticle (NP C). (b) displays the XA spectrum of the nanoparticle with the locations of the four multiplet peaks indicated as A, B, C, and D. The plots in (c) - (h) present the azimuthal dependence of the peak ratios A/B, A/C, A/D, B/C, B/D, and C/D recorded with $\mathbf{E}_{90,\Phi_s}$ (red) and $\mathbf{E}_{0,\Phi_s}$ (black). The dots represent the experimental data and the solid lines a phenomenological fit.

tilted out of the [001] direction by 11° [17, 104, 104]. In the CoO nanooctahedra the [001] direction is connecting opposing corners [85]. In case of NP A none of the possible spin axes seem to match the [001] directions particularly well. In contrast to this the spin axis $\mathbf{S}_{2,3}$ of NP B seem to match fairly well. In order to determine the spin axis more precisely one would have to measure in smaller angular steps, since steps of 45° does not allow to identify the angle where the XMLD is exactly zero. However, performing XA spectroscopy at enough azimuthal angles in order to definitely determine the spin axis would be very time consuming. Thus, XMLD contrast imaging is applied, which allows one to study the azimuthal and polarization dependence of the XMLD effect much more efficiently [32, 80, 81, 178].

6.2.3 Azimuthal dependent XMLD contrast at 100 K

In the following the XMLD contrast for individual nanoparticles is quantitatively assessed. Figure 6.7(a) displays the SEM image of a CoO (NP C) nanoparticle and (b) the corresponding XA spectrum. The four main features of the XA spectra exhibit dichroic signals and thus are used used to acquire XMLD contrast data. The four peaks are indicated

in Fig. 6.7(b) as A at 776.6 eV, B at 777.8 eV, C at 778.4 eV, and D at 779.1 eV. The ratios A/B, A/C, A/D, B/C, B/D, and C/D are considered as XMLD contrast. Figures 6.7(c)-(h) show the azimuthal dependence of the six peak ratios for the NP C. The experimental data are shown as the dots for the polarization vector parallel to the sample plane ($\mathbf{E}_{(\mathbf{90},\mathbf{\Phi_s})}$) in red and for the polarization vector pointing out of the sample plane ($\mathbf{E}_{(\mathbf{0},\mathbf{\Phi_s})}$) in black. The solid lines are fits to the data obtained using the following equation as used in Ref. [32]:

$$\mathrm{R_{fit}}(\alpha) = \mathrm{I_0} + \mathrm{I_2} \cdot \cos^2(\alpha + \psi) \tag{6.1}$$

With $\mathrm{I_0}$ being an offset, $\mathrm{I_2}$ the amplitude factor, ψ a phase factor, α the angle between the antiferromagnetic spin axis and the polarization vector of the x-rays. The fits obtained from this qualitative model are only used as a guide to the eye and to determine the variation of XMLD amplitudes with respect to the used peak ratios. The results in Figs. 6.7(c)-(h) are found by independently fitting Eq. 6.1 to the data sets for $\mathbf{E}_{(\mathbf{90},\mathbf{\Phi_s})}$ and $\mathbf{E}_{(\mathbf{0},\mathbf{\Phi_s})}$. All peak ratios containing B or C display a distinct azimuthal dependence [Figs. 6.7(c),(d),(f)-(h)]. The only ratio not showing any azimuthal dependence is A/D indicating that A and D individually do not contain a significant orientation dependent dichroic contribution. The ratio B/C in Fig. 6.7(f) clearly shows the strongest modulation. This is in good agreement with literature where the ratio B/C has been reported to be most sensitive to the antiferromagnetic order within CoO [28]. Thus, in the following R always refers to the ratio B/C.

The peak ratio B/C is used in order to determine the spin axis of individual CoO nanoparticles according to the approach reported by Czekaj *et al.* [32, 178], where α is the angle between the polarization vector of the x-rays and the spin axis:

$$\begin{aligned} \cos\alpha = {} & (\cos\Phi_\mathrm{s} \cdot \cos\Theta_\mathrm{s} \cdot \sin\Theta_\mathrm{k} + \sin\Phi_\mathrm{s} \cdot \sin\Theta_\mathrm{s}) \cdot \sin\Theta \cdot \cos\Phi \\ & + (\sin\Phi_\mathrm{s} \cdot \cos\Theta_\mathrm{s} \cdot \sin\Theta_\mathrm{k} - \sin\Phi_\mathrm{s} \cdot \sin\Theta_\mathrm{s}) \cdot \sin\Theta \cdot \sin\Phi \\ & + \cos\Theta_\mathrm{s} \cdot \cos\Theta_\mathrm{k} \cdot \cos\Theta \end{aligned} \tag{6.2}$$

Here, Φ_s and Θ_s refer to the azimuthal and polar angles as described in Chap. 4.2.1 and

Θ and Φ refer to the coordinates of the antiferromagnetic spin axis in spherical coordinates as defined in Fig. 4.3. The azimuthal dependent XMLD data for $\mathbf{E}_{(\mathbf{90},\mathbf{\Phi_s})}$ and $\mathbf{E}_{(\mathbf{0},\mathbf{\Phi_s})}$ are fitted combining Eq. (6.2) and (6.1) as follows:

$$\begin{aligned} R(\Theta_s, \Phi_s, \Theta, \Phi) = I_0 + I_2 \cdot [\\ (\cos\Phi_s \cdot \cos\Theta_s \cdot \sin\Theta_k + \sin\Phi_s \cdot \sin\Theta_s) \cdot \sin\Theta \cdot \cos\Phi \\ +(\sin\Phi_s \cdot \cos\Theta_s \cdot \sin\Theta_k - \sin\Phi_s \cdot \sin\Theta_s) \cdot \sin\Theta \cdot \sin\Phi \\ +\cos\Theta_s \cdot \cos\Theta_k \cdot \cos\Theta)]^2 \end{aligned} \tag{6.3}$$

Equation (6.3) is applied as a global fit model to the experimentally obtained XMLD curves for $\mathbf{E}_{(\mathbf{0},\mathbf{\Phi_s})}$ and $\mathbf{E}_{(\mathbf{90},\mathbf{\Phi_s})}$. The spherical coordinates Θ and Φ are retrieved from the fit by sharing the fit parameters I_2, Θ, and Φ while I_0 is fitted independently for the data sets obtained with $\mathbf{E}_{(\mathbf{90},\mathbf{\Phi_s})}$ and $\mathbf{E}_{(\mathbf{0},\mathbf{\Phi_s})}$. I_0 needs to be fitted independently since this parameter contains the information about the component of $\mathbf{S}$ which is oriented perpendicular to the sample plane and thus is constant with respect to Φ_s. This means that I_0 is large for $\mathbf{E}_{(\mathbf{90},\mathbf{\Phi_s})}$ and small for $\mathbf{E}_{(\mathbf{0},\mathbf{\Phi_s})}$ if $\mathbf{S}$ points largely out of the sample plane and vice versa. The relation between the orientation and the extrema of the XMLD contrast curves will be discussed later.

Figure 6.8 displays the results of the fits for NP C, NP D, and NP E. Figures 6.8(a) shows the SEM image of NP C with the propagation direction $\mathbf{k}$ (white) and the polarization vector $\mathbf{E}_{(\mathbf{90},\mathbf{0})}$ (red) indicated. The Φ_s and Θ_s dependent curves are displayed in (b) and (c), respectively. The dots with error bars display the experimentally obtained contrast data and the solid lines in (b) are obtained using the fit model in Eq. (6.3) for $\mathbf{E}_{(\mathbf{90},\mathbf{\Phi_s})}$ (red) and $\mathbf{E}_{(\mathbf{0},\mathbf{\Phi_s})}$ (black). The solid black line in (c) is simulated using the obtained fit parameters while holding Φ_s at 20 ° and instead varying Θ_s. The results for NP D [Figs. 6.8(d) (f)] and NP E [Figs. 6.8(g)-(i)] are presented similar to NP A [c.f. Figs. 6.8(a)-(c)].

In order to determine the orientation of the antiferromagnetic spin axis it is fundamental to know if the maximum or the minimum of the XMLD contrast curve corresponds to $\mathbf{E} \parallel \mathbf{S}$. This can be directly derived from the curves for NP C. The curve in Fig. 6.8(b)

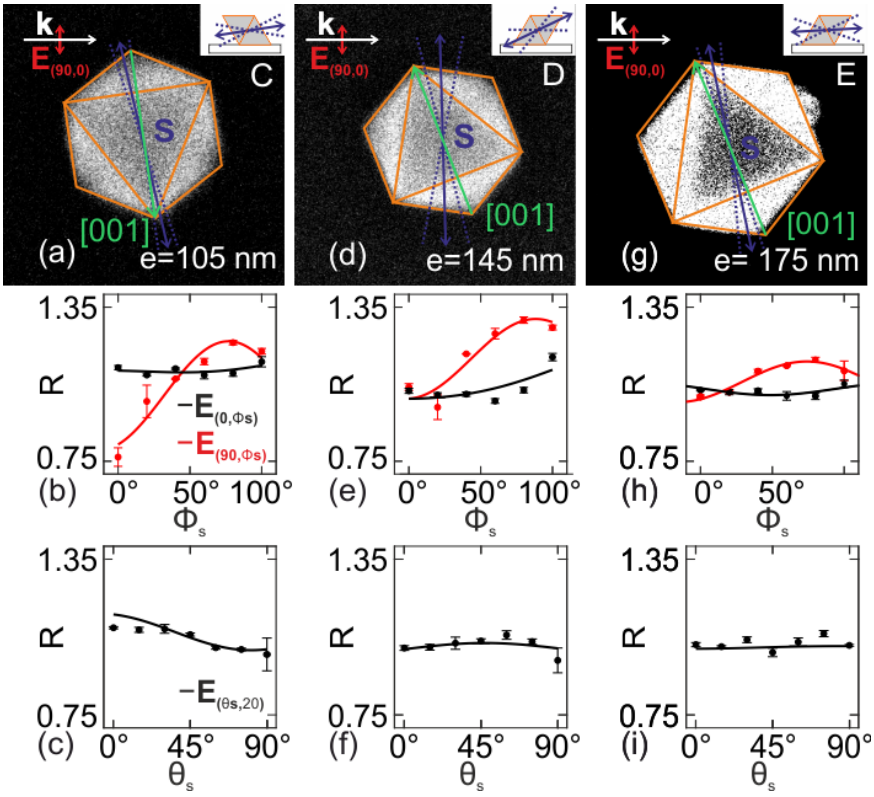

FIG. 6.8: (a), (d), and (g) SEM images of NP C, NP D, and NP E with the propagation direction of the x-rays (white arrow), $\mathbf{E}_{(\mathbf{90,45})}$ (red arrow), the crystals orientation (orange line), and the [001] directions indicated (green arrow). The XMLD vs. the azimuthal angle Φ_s and vs. the polarization angle Θ_s is shown in (b), (e), and (h) respectively in (c), (f), and (i). Additionally the orange dashed lines indicate the azimuthal angle at which the orientation of the nanoparticles is obtained as shown in the SEM images.

for $\mathbf{E}_{\mathbf{90},\mathbf{\Phi_s}}$ shows a large orientation dependence, which suggests that the spin axis has a large component parallel to the sample plane. The polarization dependent curve shown in Fig. 6.8(c) shows that the minimum of the curve is close to Θ_s=90 ° yielding that R exhibits a minimum if $\mathbf{E} \parallel \mathbf{S}$. This factor is implemented to the fitting model to determine the spin axis of individual nanoparticles.

Table 6.2 displays the obtained values for Θ and Φ of the spin axis of NP C, NP D, and NP E. The blue double headed arrows in Fig. 6.8(a), (d), and (e) display the in plane orientation of the spin axis accordingly to the fitted angles Φ and the insets shows the orientation of Θ. In order to compare the determined orientations of the spin axis of NP C-E the expected spin axis as observed for CoO in its bulk form are shown schematically in Fig. 6.9(a) and (b). Theoretically a set of 12 spin axes is possible in bulk CoO [17, 99, 100, 104, 105]. The full set of possible spin axis for all three nanoparticles

	Θ(°)	ΔΘ(°)	Φ(°)	ΔΦ(°)
NP C	99	19	-77	6
NP D	116	26	-88	13
NP E	93	22	-78	7

Table 6.2: Θ and Φ and their according fit errors for all CoO nanoparticles displaying a pronounced azimuthal dependence.

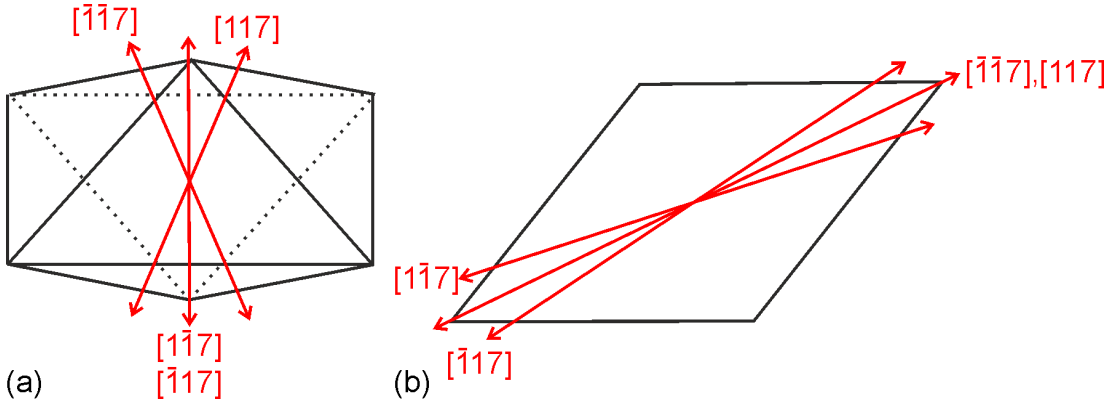

FIG. 6.9: (a) and (b) show the respective component of the spin axis parallel and perpendicular to the sample plane. Here, only the possible orientation with a major component along the [001] direction are shown.

can be found in Appendix B. Here, a limit set of axes are shown. In Fig. 6.8(a), (d), and (g) the [001] direction of the nanocrystals is indicated by the respective green arrows. It is assumed that the crystal direction indicated by the blue arrows correspond to the [001] directions of the nanoparticles, thus the possible spin axis would be described by the set of the $[\bar{1}\bar{1}7]$, $[1\bar{1}7]$, $[\bar{1}17]$, and [117] directions as shown in Fig. 6.9(a) and (b). It is found that NP D and E exhibit their spin axis in a direction which are almost compatible with the [117] and $[1\bar{1}7]$ directions. In case of NP C the spin axis seems to be tilted into the sample plane too strongly. However, in terms of the in plane orientation of the spin axis NP C seems to be most consistent with a $[1\bar{1}7]$ or a $[\bar{1}17]$ direction.

It has been reported that the spins within magnetically ordered CoO point almost

along the direction of the tetragonal distortion of the unit cell due to the magnetostructural transition which takes place across the Néel temperature of CoO [17]. The spins are expected to be tilted from the tetragonal axis by about 11 °. This suggests that the tetragonal deformation of NP D and E are almost parallel to the determined spin axis. NP C indicates that the spin axis of some individual CoO nanoparticles might not reflect the orientation which is expected from CoO in its bulk. Such a behavior could potentially be explained by microstructural defects within the magnetic volume of the nanoparticles. Further, as it is reported in the study of the goethite nanoparticles in Chap. 5 an interfacial interaction or interfacial strain at the nanoparticles-substrate interface could give rise to unexpected orientation of the spin axis of at least a part of the nanoparticles. At this point the mechanism which might lead to the canting of the antiferromagnetic axis of individual CoO nanoparticles out of the direction which is favored by the magnetocrystalline anisotropy is not fully explored. In order to investigate interfacial effects one would possibly have to determine the spin axis of individual CoO nanoparticles on various substrates. This might allow to more precisely understand the importance of interfacial interaction on the magnetic structure of nanoscaled antiferromagnets.

6.3 Uncompensated magnetic moments of individual CoO nanoparticles

Often it is observed that AFM nanoparticles exhibit uncompensated magnetic moments due to their small size. Those magnetic moments usually are expected to arise from uncompensated magnetic moments at the surface of the nanoparticles [106, 108, 109], from a frustrated non-collinear spin structure [111], or vacancies in the lattice of the nanoparticles [116]. Here, the magnetic moments are probed employing the XMCD contrast at the Co L_3 edge. The XMCD contrast is probed for features A-D at 100 K of the XA spectrum as indicated in Fig. 6.7(a). For all photon energies very similar results are obtained, thus only the data recorded at a photon energy of 778.4 eV is displayed, which corresponds to the B feature at the Co L_3 edge. All results are obtained at 100 K. The XMCD contrast images are recorded at $\Phi_s = 0\,°$. At this angle the spin axes of NP C, D, and E are oriented almost perpendicular with respect to $\mathbf{k}$. The results for NP C-E

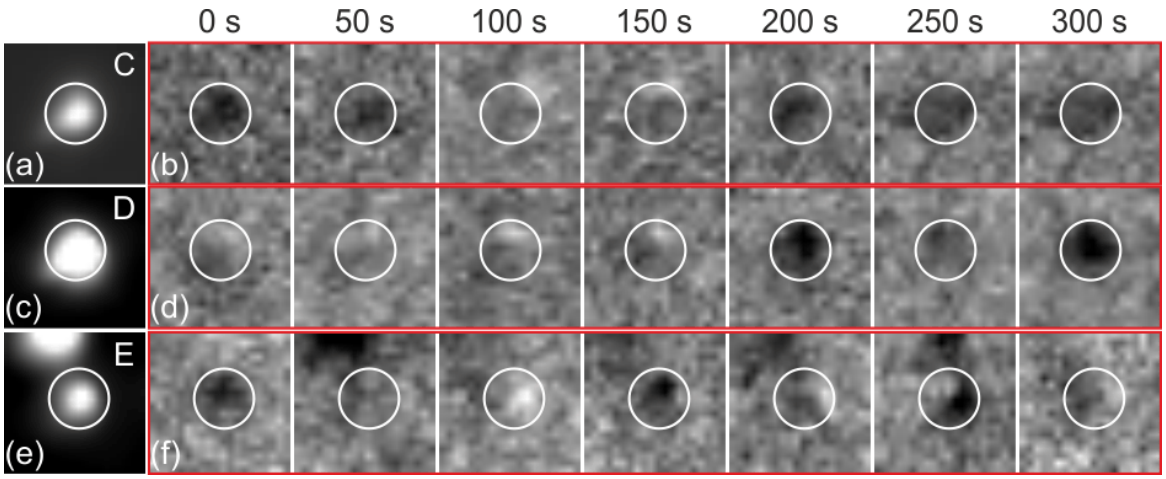

FIG. 6.10: (a), (c), and (e) show the XPEEM images of the nanoparticles shown in Fig. 6.8(a), (d), and (g), respectively. The panels (b), (d), (f), and (h) display the XMCD of the individual nanoparticles as a function of time.

at 100 K are shown in Fig. 6.10. First of all it is found that each nanoparticle exhibits some XMCD contrast suggesting the presence of uncompensated magnetic moments as previously reported [52, 85]. However, the XMCD data reveal switching on the scale of tens of seconds of the individual nanoparticles or of at least the probed magnetic moments indicating that the nanoparticles behave superparamagnetically at temperatures as low as 100 K. This contrasts the finding of open hysteresis loops [52] for nanoparticles in a similar size range up to temperatures well above 300 K. However, in contrast to the SQUID measurements, XPEEM only probes the magnetism up to a depth of about 5 nm. This could mean that the magnetic moments in Ref. [52] are either deeper in the volume of the nanoparticles or at least or they are not located in the probed $3d$ states of the Co ions. The appearance of white, gray, and black XMCD contrast is observed for all three nanoparticles. Of special interest is the black and white XMCD at this particular orientation of the spin axes, because it suggests that the uncompensated magnetic moments can be stabilized perpendicular to the antiferromagnetic spin axis of the individual CoO nanoparticles. This could indicate that the magnetic moment arise from a slight canting of the two sublattices as recently suggested by calculations [16]. Further, the observed switching events can be used qualitatively in order to estimate the energy barrier using the Néel-Arrhenius law as:

$$\tau = \tau_0 \cdot exp\left(\frac{E_m}{k_B T}\right) \tag{6.4}$$

With τ_0 being the inverse attempt frequency, E_m the magnetic energy barrier, k_B the Boltzmann constant, and T the measurement temperature. The relaxation time τ is estimated from the average switching frequency to be roughly about 100 s. Now the equation can be rewritten in order to estimate the magnetic energy barrier as $E_m = log\left((\tau)/(\tau_0)\right) \cdot k_B T$. Assuming an inverse attempt frequency of 10^{-9}s as often done for similar systems [65, 72, 89, 93] yields $E_m = 100\,\mathrm{meV}$. Alternatively, the magnetic energy barrier can be estimated using the magnetocrystalline anisotropy of CoO, which is reported to be $\mathrm{K} = 10^7\,\mathrm{Jm}^{-3}$ [104, 105], and with the volume of a nanoparticle with a edge length $e = 150\,\mathrm{nm}$ this yields $\mathrm{E_m} \approx 10^4\,\mathrm{eV}$. Hence, the effective magnetic energy barrier which is can be deduced from the experimental data is five orders of magnitude lower that what would be expected for CoO nanoparticles of this size. According to the reported value of K a CoO nanoparticle would have to be as small as 2.5 nm in order to be superparamagnetically relaxed at 100 K.

This result could support recent theoretical calculation, which suggest that the thermal stability of antiferromagnetic nanoparticles is significantly reduced with respect to their ferromagnetic counterparts [16]. This is especially the case for antiferromagnetic materials with a low Gilbert damping constant. The damping constant of NiO has been reported to be $\mathrm{g} = 2.1 \times 10^{-4}$ [185], which could be similar in CoO. The calculations found for materials with a low Gilbert damping might exhibit a switching frequency, which is increase up to five orders of magnitude, compared to their ferromagnetic counterpart. The authors explain this by an additional switching mechanism, which allows antiferromagnetic materials with low Gilbert damping to reverse their directions of the sublattices without significantly changing the energy of the system. This mechanism leads to a slight canting of the antiferromagnetic sublattices and thus giving rise to small uncompensated magnetic moments, which are oriented orthogonally with respect to the Néel vector of the system.

As discussed above the appearance of black and white XMCD contrast at $\Phi_\mathrm{s} = 0\,^\circ$ suggest that the magnetic uncompensated magnetic moments have a component perpendicular to the spin axis of the CoO nanoparticles. This could be interpreted as first

evidence for the enhanced switching mechanism described by Rosza *et al.* [16]. Further, the frequent appearance of gray or almost gray contrast could be understood rather as multiple 180 ° switching events of the antiferromagnetic sublattices during the acquisition of an image than a reorientation of the direction of the uncompensated magnetic moments by 90 °.

Another possibility for the occurrence of uncompensated magnetic moments would be that they emerge due to the surface sensitivity of XPEEM, when the XMCD signal is dominated by the ferromagnetically coupled layer at the top of the nanoparticles. In this case the magnetic moments would be parallel to the spin axis of the individual nanoparticles. However, the apparent black and white contrast in the XMCD contrast images shows that at least part of the magnetic moments are oriented perpendicular to **S**. A last possibility would be that the uncompensated magnetic moments arise from uncompensated magnetic sites. In this case one would also expect that the uncompensated couple parallel to the antiferromagnetic lattice. To clarify this orientation dependent XMCD measurements are needed in the future.

In the previous example (NP C-NP E) no changes of the XMLD contrast is observed, although switching in the XMCD signal is observed. This can be understood as a switching of the spin system by 180 °, which reverses the XMCD contrast without any effect on the measured XMLD signal (due to symmetry reasons). Hence, it remains unclear, whether the antiferromagnetic spins engage in thermally induced reversals. Figure 6.11(a) displays the SEM image of NP F. The curve for the azimuthal dependent XMLD is displayed in Fig. 6.11(b) which does not reveal a particular orientation dependence of the XMLD. This can either be understood as an indication for a magnetic multi domain state or that the NP F is able to reorient its spin axis by other angels than 180 °. However, observing the nanoparticle at a fixed orientation should allow to identify changes in time more clearly. Figure 6.11(c) shows the polarization dependence of the XMLD signal at Φ_s =20 °. In these measurements the orientation of the nanoparticle is kept fixed, and thus, the XMLD signal should be continuous function of the polarization angle Θ_s. However, the data reveal a clear jump in the data at Θ_s=45 °. Such abrupt change is not compatible with the polarization dependency given by Eq. 6.3, and thus, is assigned to a thermally induced switch of the spin axis. Actually, the nanoparticle switches the

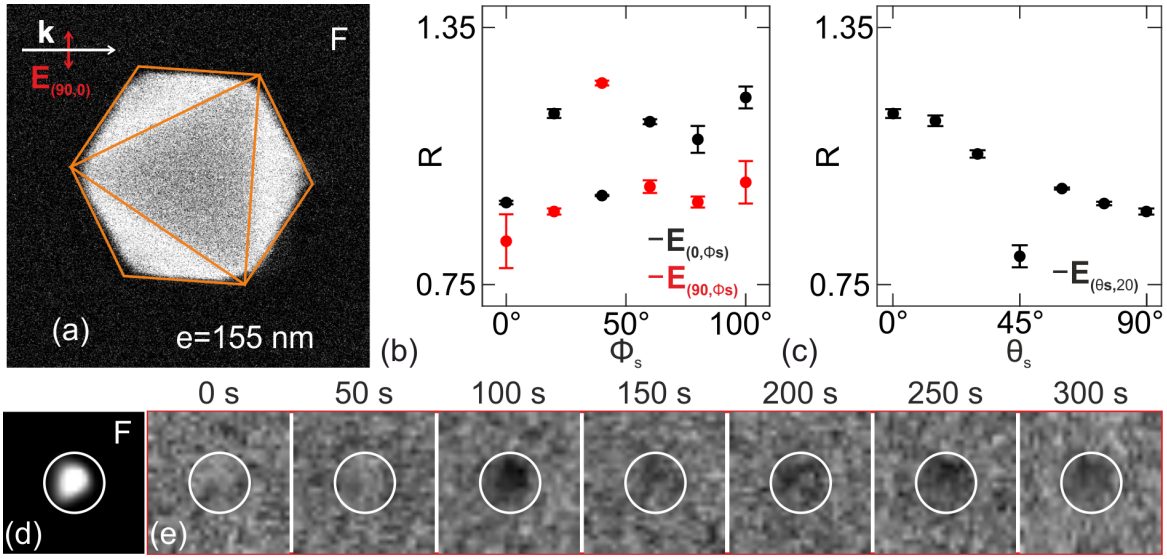

FIG. 6.11: (a) SEM image of a individual CoO nanoparticle (NP F). (b) the orientation dependent XMLD contrast curves recorded with $\mathbf{E}_{(\mathbf{90},\mathbf{\Phi_s})}$ and $\mathbf{E}_{(\mathbf{0},\mathbf{\Phi_s})}$ and (c) the polarization dependent XMLD contrast curve of NP F. (d) and (e) display the XPEEM elemental contrast and the time dependent XMCD contrast of NP F recorded at Φ_s.

orientation of its antiferromagnetic axis two times (forth and back) during the course of the polarization dependent measurements, which lasted for two hours. Another possibility is that the nanoparticle switches between different complex domain structure. However, without intra-particle spatial resolution it is difficult prove such mechanism. The XMCD signal of NP F is also investigated. Figures 6.11(d) and (e) display the elemental contrast image and the time dependence of the XMCD contrast of NP F. The XMCD contrast of NP F displays more frequently gray contrast at NP C, D, and F in Fig. 6.10(b), (d), and (f). This indicates that NP F has a higher likely hood of multiple switching events over the acquisition time of one XMCD contrast image. Thus, the relaxation time τ is lower than for the other three nanoparticles. Thus, it can be speculated that E_m for NP F is lower than for the other three.

6.4 Conclusion

The chemical state in the surface-near region (ca. 5 nm) of the CoO nanoparticles is addressed by employing spatially resolved XA spectroscopy. The data reveal that this surface region is dominated by Co^{2+} in agreement with previously reported EELS data. Cobalt ions in Co^{3+} oxidation state, as expected for Co_3O_4, provide only a weak contribution to the XA data, if present at all. The appearance of XMLD around the Néel temperature of bulk CoO in the temperature dependent XMLD spectromicroscopy experiments for the CoO nanoparticles, indicate a magnetic phase transition from the paramagnetic to the antiferromagnetic state in individual CoO nanoparticles. Angular-dependent XMLD contrast data suggest single domain states in about two third of the cobalt nanoparticles. The spin axes of the nanoparticles do not necessarily coincide with the $[\bar{1}\bar{1}7]$ directions, which are known as the spin axes of bulk CoO. This could be due to microscopic defects within the nanoparticles or due the interaction with the substrate. Among the 11 investigated nanoparticles, a size-dependent trend was not observed. The sizes range from 100 to 200 nm. The other particles show a less regular angular-dependent XMLD contrast, which is assigned either to multi-domain states or to thermally induced switches of the spin structure within the nanoparticles.

XMCD measurements revealed direct evidence for thermally induced magnetization dynamics in the nanoparticles at 100 K. Such dynamics is not expected based on the Arrhenius law with the commonly assumed inverse attempt frequency $\tau_0 = 10^{-9}$ s and the high magnetic anisotropy known from bulk CoO. Indeed, we find a discrepancy in the estimated magnetic energy barrier of about five orders of magnitude, when comparing the experimentally observed with the expected switching rate. Thermally induced magnetic switching also observed in XMLD data at a slightly lower rate. These observations could confirm recent theoretical predictions, that antiferromagnetically ordered nanoparticles with low Gilbert damping can exhibit strongly enhanced switching rates, when compared to their ferromagnetic counterparts. Further, our observations demonstrate that the previously found ferromagnetically blocked magnetic moments at room temperature, are not situated in the surface near region probed in our experiments or not associated with the Co 3*d* states probed by XMCD.

Chapter 7

Conclusion

In this thesis goethite and CoO/Co_3O_4 core-shell nanooctahedra are investigated. The focus is put on the correlation of the morphological, chemical, and magnetic properties of those two antiferromagnetic $3d$ transition metal oxide nanoparticles systems. This is achieved utilizing SEM, TEM, RHEED, and XRD in order to investigate the morphology, potential preferential orientation of the nanoparticles, and the crystallinity of the nanoparticles. The chemical and antiferromagnetic properties investigated by means of XA spectromicroscopy, azimuthal and polarization dependent XLD spectromicroscopy and XMLD contrast imaging. Additionally the emergence of uncompensated magnetic moments is studied using XMCD contrast imaging.

It is found using XA spectromicroscopy and additionally in case of goethite RHEED measurements that the two nanoparticle systems display different chemical behaviors. While the goethite nanoparticles are found to suffer from slight chemical change upon the insertion into UHV, the CoO nanoparticles usually do not change their composition significantly. However, it is found that the sensitivity to the Co_3O_4 shell of the CoO nanooctahedra is surprisingly weaker than expected for a shell which nominally should be around 2-4 nm. This is attributed to a non-stoichiometric and potentially defective shell. Further it is shown that the stability of goethite nanoparticles is reduced if the nanoparticles have been thermally treated to 460 K within UHV. This indicates that the selection of the $3d$ transition metal oxide nanoparticle system is crucial and also that the thermal history of a sample is a very important parameter to investigate in order to understand the thermal and potentially the magnetic behavior of the nanoparticles.

The XLD of agglomerated goethite nanoparticles is studied at RT, where an effective XLD can be measured. This is unexpected since the nanoparticles are expected to be randomly distributed which should let the XLD vanish. On the first level this XLD is attributed to an preferential orientation of the long axis of the acicular nanoparticles which orients it self parallel to the sample plane. The emergence of the XLD in the agglomerates is attributed to the alignment of the long axis of the nanoparticles since it is routinely reported that the length axis of goethite nanoparticles corresponds to the crystalline a-axis. Thus, a elementary symmetry breaking arising form the crystal structure can be explained.

In order to identify the magnetic phase transitions from antiferromagnetic to paramagnetic both systems are measure by means of temperature dependent XLD spectromicroscopy. It is found that the goethite and CoO nanoparticles exhibit a Néel temperature which is very close to the ordering temperature of the respective bulk materials. This indicates that goethite nanoparticles with a l=110 nm and w=30 nm and CoO nanoparticles with a edge length l=150 nm do not exhibit signs of significant size effects which might lower the magnetic ordering temperatures. Thus, the both nanoparticles display almost bulk-like behavior in terms of their respective Néel temperatures.

The second important question which is addressed for both systems is how the magnetic **S** spin axis can be determined. For this the goethite and CoO nanoparticles are investigated by means of orientation dependent XLD spectromicroscopy. The XMLD of goethite nanoparticles is predominantly uniform with respect azimuthal orientation of the sample, while the XNLD displays an azimuthal dependence which can be interpreted as a 6 fold symmetry of the crystal. However, more experiments would be necessary in order to completely address the exact azimuthal behavior of the XNLD. The surprising emergence of a orientation independent XMLD suggest, that the spin axis of goethite nanoparticles are oriented almost perpendicular with respect to the sample surface. This is concluded since a strong in-plane component would significantly reduce the XMLD of agglomerates with respect to the individual goethite nanoparticles. This finding is rationalized by an interfacial van der Waals force or interfacial strain, which reorient the spin axis of goethite nanoparticles preferentially perpendicular to the sample plane.

The results of the orientation dependent XMLD spectromicroscopy on individual CoO

nanoparticles reveals a strong anisotropy of the XMLD with respect to the azimuthal rotation angle of most investigated majority of the investigated nanoparticles. It is possible to propose possible orientation spin axis for each individual CoO nanoparticles based on this data. The spin axis are determined at the azimuthal angles where the XMLD spectrum vanishes. Further, the azimuthal dependence of XMLD contrast is studied. The advantage of this method is that contrast image are formed by only using one x-ray polarization at the time. Recording orientation and polarization dependent XMLD contrast images allows to unambiguously determine the spin axis of individual CoO nanoparticles. The reconstruction of the spin axis suggest that the effective spin axis of some nanoparticles match well with the expected spin axes known from bulk CoO. Although, their are also cases where the spin axes display an orientation which is not consistent with bulk CoO. The spin axis of CoO nanoparticles do not display an obvious preferential orientation as those of goethite. However, one could argue that the misalignment of the spin axis of some of the nanoparticles with respect compared to bulk CoO, hints that the interface between the nanoparticles and the substrate can affect the orientation of the spin axes.

Lastly, potential uncompensated magnetic moments of CoO nanoparticles are investigated utilizing XMCD contrast imaging. The XMCD contrast images indicates uncompensated magnetic moments which behave superparamagnetically down to temperatures as low as 100 K. This is unexpected since no indications are found in the XMLD contrast data suggesting thermal switching of the spin axis of the very same nanoparticles. However, it shall be noted that the XMLD effect is inherently insensitive to 180 ° inversions of the sublattices. Evidence is found that the uncompensated magnetic moments are oriented perpendicularly to the spin axis of the nanoparticles. This potentially could be first experimental evidence for a recently proposed model on enhanced thermal switching in antiferromagnetic nanoparticles [16]. In goethite nanoparticles no uncompensated magnetic moments could be detected (not shown). However, this not necessarily means that no such magnetic moments exist but that those magnetic moments just switch to fast at room temperature to be seen by means of XPEEM.

In conclusion the studies of goethite and CoO/Co_3O_4 core-shell nanooctahedra demonstrates the possibility of determining the spin axis of individual antiferromagnetic nanoparticles. This is of profound interest since fields as antiferromagnetic spintronics has

a demand for a very fundamental understanding of nanoscale antiferromagnetic systems. Those systems are inherently difficult to probe since they exhibit usually no measurable magnetic moments or stray fields. Additionally, the work reported here indicates that interfaces can have a crucial impact on the properties of antiferromagnetic materials at the nanoscale. This could be of very profound interest for potential spintronics applications since only by choosing the right substrate for a certain system it could be possible to orient the spin axis along or perpendicular to the sample plane.

Chapter 8

Outlook

8.1 Different nanoparticles

8.1.1 Antiferromagnetic oxides

Antiferromagnetic materials will likely gain further significance over the next decades. Especially concerning antiferromagnetic spintronics it will be more and more important to understand antiferromagnetism at the nanoscale. In this context it might be interesting to perform similar experiments as demonstrated in this thesis on nickel oxide nanoparticles. NiO is a very well known material in bulk and thin film form. One of the advantages of NiO over CoO is the much higher chemical stability since nickel tends to exist predominantly as Ni^{2+} ion, which makes NiO a very stable material. Further NiO is already used in some AFM spintronics application. This makes NiO nanoparticles the optimal candidate to contribute actively to AFM spintronics.

8.1.2 Multiferroic nanoparticles

The investigation of antiferromagnetism at the nanoscale is actually only a first step towards nanoparticle based multiferroic systems. A material is multiferroic if it exhibits at least two correlated ordering parameters (e.g. antiferromagnetic-ferroelectric, antiferromagnetic-ferroelastic etc). Such systems are technologically interesting since they potentially allow to manipulate the magnetic properties by applying electric fields. Here it is important to point out that there are in principle two possible routes to obtain mul-

tiferroic systems. On one hand there are intrinsic multiferroics such as bismuth ferrite ($BiFeO_3$) exhibiting ferroelectric polarization and and antiferromagnetic order at room temperature [43]. On the other hand two materials can be coupled by an interface where one material has a magnetic and the other a ferroelectric ordering parameter. Recently the feasibility to synthesize core-shell nanoparticles with a $CoFe_2O_4/BaTiO_3$ with couples ordering parameters have been demonstrated [186]. In this case the $CoFe_2O_4$ core exhibits a ferrimagnetic and the $BaTiO_3$ shell a ferroelectric order.

From the perspective of characterization of individual nanoparticles by means of XPEEM or related soft x-ray techniques (STXM, soft x-ray ptychography) artificial multiferroics offer certain advantages. The two ordering parameters can be probed individually utilizing different absorption edges (Co and Fe $L_{2,3}$ for $CoFe_2O_4$ and Ti $L_{2,3}$ for $BaTiO_3$). However, also the splitting of the ferroelectric and ferromagnetic ordering parameter is technically possible utilizing that especially at the L_2 edges of $3d$ transition metal oxides often the magnetic contribution dominates the linear dichroism. In this case the ferroelectric ordering parameter could be probed using the O K edge. The reason for this is that the displacement of the Bi atoms in the unit cell in order to form the ferroelectric polarization should give rise to an structural linear dichroism which is expected to be visible at the O K edges.

8.2 Soft X-ray ptychography at room temperature

Presently, a new soft x-ray ptychography microscope is being developed at the Surface/Interface:Microscopy (SIM) beamline [187]. The instrument shall allow in the future to image samples with very high spatial resolution close to the wavelength limit, which is 1 - 2 nm. A spatial resolution of about 10 nm has already been demonstrated which is about the best resolution presently achieved by scanning transmission x-ray microscopy (STXM) and about five time better than that of XPEEM. While XPEEM and STXM measure only the absorption amplitude it is possible to reconstruct the phase and amplitude information using soft x-ray ptychography. The phase information could potentially be used in order to extract complementary information from samples.

Figures 8.1 (a) displays a reconstructed ptychography amplitude image and Fig. 8.1(b)

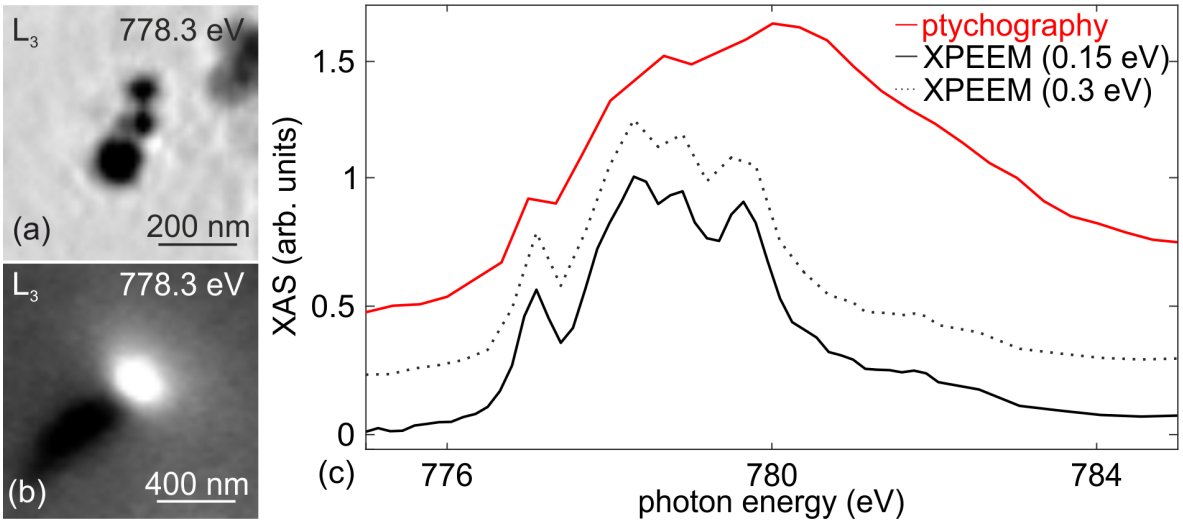

FIG. 8.1: (a) shows the reconstructed amplitude of a ptychography image at the Co L_3 edge and (b) a XPEEM image recorded at the same energy of CoO/Co_3O_4 core-shell nanooctahedra. In (c) the XA spectra of the ptychographic energy scan (red line) and of a XPEEM XA spectra with a energy resolution of 0.15 eV (solid black line) and 0.3 eV (dashed black line).

a XPEEM image of CoO/Co_3O_4 nanoparticles. The ptychography image it reveals that there are three individual nanoparticles with some space in between of them. Further, all three nanoparticles display sharp edges. In contrast in the XPEEM image the NP A [SEM image in Fig. 6.5 (a)] appears oval with no apparent sharp edges. While NP A in the XPEEM image has a size of about 195 nm, the size of the largest nanoparticle in the ptychography image is about 150 nm. Thus, it is clear that the resolution of those ptychography images is already a lot better. Even more since the nanoparticle in the XPEEM image appears about 1.4 times larger than it is found to be by means of SEM. Obviously ptychographic imaging will be able to improve the microscopic resolution significantly in the future. Thus, it will help eventually to investigate if the such relatively large antiferromagnetic nanoparticles actually exhibit magnetic single or multi domain states. Further, one could potentially investigate if uncompensated magnetic moments as found in this thesis couple over the whole particle or if the coupling is broken at the relatively sharp edges of the octahedra. Those investigations could be done using XMCD and XMLD contrast imaging with ultra high resolution as it has not been possible so far.

At the moment the ptychography microscopy only works at normal incidence and thus is only able to probe out of plane XMCD and in-plane XMLD. In order to make the

microscope more versatile, the possibilities of ptychography in reflection are also explored. Reflection soft x-ray ptychography would the allow to measure non transparent samples. Further, the grazing incident of the x-rays in such geometry would again allow to also probe in-plane XMCD and out-of-plane XMLD as it is possible in XPEEM but with a resolution which might be between one and two orders of magnitude higher.

Further, first spectroscopic measurements have been performed with the ptychography microscope. In Fig. 8.1 (c) XA spectra recorded using soft x-ray ptychography (red line) and XPEEM (black line) are shown. The dashed line displays the spectrum recorded by XPEEM with a reduced energy resolution, in order to match the chosen resolution of the ptychographically obtained spectrum. Apparent differences of the spectra have to be investigated further ind the future.

However, the data demonstrate that soft x-ray ptychography could become an important tool in order to investigate the properties of individual $3d$ transition metal oxide nanoparticles. Still some development is necessary until the full potential of the method can be utilized. Especially in order to study the properties of antiferromagnetic nanoparticles, it will be important to implement the microscope into a high vacuum chamber and being able to measure the samples in various geometries.

References

[1] Néel, L. Magnetism and the local molecular field. URL `http://www.nobelprize.org/nobelprizes/physics/laureates/1970/neellecture.pdf`.

[2] Baltz, V. *et al.* Antiferromagnetic spintronics. *Rev. Mod. Phys.* **90**, 015005 (2018).

[3] Wadley, P. *et al.* Electrical switching of an antiferromagnet. *Science* **351**, 587 (2016).

[4] Jungwirth, T., Marti, X., Wadley, P. & Wunderlich, J. Antiferromagnetic spintronics. *Nat. Nannotechnol.* **11**, 231 (2016).

[5] Jungwirth, T. *et al.* The multiple directions of antiferromagnetic spintronics. *Nat. Phys.* **14**, 200 (2018).

[6] Béa, H., Gajek, M., Bibes, M. & Barthélémy, A. Spintronics with multiferroics. *J. Phys. Condens. Matter* **20**, 434221 (2008).

[7] Saidl, V. *et al.* Optical determination of the Néel vector in a CuMnAs thin-film antiferromagnet. *Nat. Photonics* **11**, 91 (2017).

[8] Kosub, T. *et al.* Purely antiferromagnetic magnetoelectric random access memory. *Nat. Commun.* **8**, 13985 (2017).

[9] Park, B. G. *et al.* A spin-valve-like magnetoresistance of an antiferromagnet-based tunnel junction. *Nat. Mater.* **10**, 347 (2011).

[10] Hamakawa, Y. *et al.* Spin-valve heads utilizing antiferromagnetic NiO layers. *IEEE Trans. Magn.* **32**, 149 (1996).

[11] Železný, J. *et al.* Relativistic Néel-order fields induced by electrical current in antiferromagnets. *Phys. Rev. Lett.* **113**, 157201 (2014).

[12] Olejník, K. *et al.* Terahertz electrical writing speed in an antiferromagnetic memory. *Sci. Adv.* **4**, eaar3566 (2018).

[13] Almeida, T. P. *et al.* Visualized effect of oxidation on magnetic recording fidelity in pseudo-single-domain magnetite particles. *Nat. Commun.* **5**, 5154 (2014).

[14] Bhatti, S. *et al.* Spintronics based random access memory: a review. *Mater. Today* **20**, 530 (2017).

[15] Kimel, A. V. *et al.* Inertia-driven spin switching in antiferromagnets. *Nat. Phys.* **5**, 727 (2009).

[16] Rózsa, L., Selzer, S., Birk, T., Atxitia, U. & Nowak, U. Reduced thermal stability of antiferromagnetic nanostructures. *Phys. Rev. B* **100**, 064422 (2019).

[17] Roth, W. L. Magnetic structures of MnO, FeO, CoO, and NiO. *Phys. Rev.* **110**, 1333 (1958).

[18] Stöhr, J., Padmore, H. A., Anders, S., Stammler, T. & Scheinfein, M. R. Principles of x-ray magnetic dichroism spectromicroscopy. *Surf. Rev. Lett.* **05**, 1297 (1998).

[19] van der Laan, G., Telling, N. D., Potenza, A., Dhesi, S. S. & Arenholz, E. Anisotropic x-ray magnetic linear dichroism and spectromicroscopy of interfacial Co/NiO(001). *Phys. Rev. B* **83**, 064409 (2011).

[20] Moriyama, T., Oda, K., Ohkochi, T., Kimata, M. & Ono, T. Spin torque control of antiferromagnetic moments in NiO. *Sci. Rep.* **8**, 14167 (2018).

[21] Baldrati, L. *et al.* Full angular dependence of the spin Hall and ordinary magnetoresistance in epitaxial antiferromagnetic NiO(001)/Pt thin films. *Phys. Rev. B* **98**, 024422 (2018).

[22] Arenholz, E., van der Laan, G., Chopdekar, R. V. & Suzuki, Y. Anisotropic x-ray magnetic linear dichroism at the Fe $L_{2,3}$ edges in Fe_3O_4. *Phys. Rev. B* **74**, 094407 (2006).

[23] Gong, G. Q., Gupta, A., Xiao, G., Qian, W. & Dravid, V. P. Magnetoresistance and magnetic properties of epitaxial magnetite thin films. *Phys. Rev. B* **56**, 5096 (1997).

[24] Li, X. W., Gupta, A., Xiao, G. & Gong, G. Q. Transport and magnetic properties of epitaxial and polycrystalline magnetite thin films. *J. Appl. Phys.* **83**, 7049 (2019).

[25] Alexe, M. *et al.* Ferroelectric switching in multiferroic magnetite Fe_3O_4 thin films. *Adv. Mater.* **21**, 4452 (2009).

[26] Rodríguez-Fernandez, A. *et al.* Chiral properties of hematite α-Fe_2O_3 inferred from resonant Bragg diffraction using circularly polarized X-rays. *Phys. Rev. B* **88**, 094437 (2013).

[27] Martin-Hernandez, F. & Guerrero-Suárez, S. Magnetic anisotropy of hematite natural crystals: high field experiments. *Int. J. Earth Sci.* **101**, 637 (2012).

[28] Wu, J. *et al.* Direct observation of imprinted antiferromagnetic vortex states in CoO/Fe/Ag(001) discs. *Nat. Phys.* **7**, 303 (2011).

[29] Negi, D. S. *et al.* Robust room temperature ferromagnetism in epitaxial CoO thin film. *Appl. Phys. Lett.* **103**, 242407 (2013).

[30] Csiszar, S. I. *et al.* Controlling orbital moment and spin orientation in CoO layers by strain. *Phys. Rev. Lett.* **95**, 187205 (2005).

[31] van der Laan, G., Arenholz, E., Chopdekar, R. V. & Suzuki, Y. Influence of crystal field on anisotropic x-ray magnetic linear dichroism at the Co^{2+} $L_{2,3}$ edges. *Phys. Rev. B* **77**, 064407 (2008).

[32] Czekaj, S., Nolting, F., Heyderman, L. J., Willmott, P. R. & van der Laan, G. Sign dependence of the x-ray magnetic linear dichroism on the antiferromagnetic spin axis in $LaFeO_3$ thin films. *Phys. Rev. B* **73**, 020401 (2006).

[33] Seo, J. W. *et al.* Antiferromagnetic $LaFeO_3$ thin films and their effect on exchange bias. *J. Phys. Condens. Matter* **20**, 264014 (2008).

[34] Scholl, A. *et al.* Observation of antiferromagnetic domains in epitaxial thin films. *Science* **287**, 1014 (2000).

[35] Scholl, A. *et al.* Domain-size-dependent exchange bias in CoO/$LaFeO_3$. *Appl. Phys. Lett.* **85**, 4085 (2019).

[36] Folven, E. *et al.* Antiferromagnetic domain reconfiguration in embedded $LaFeO_3$ thin film nanostructures. *Nano Lett.* **10**, 4578 (2010).

[37] Luening, J. *et al.* Determination of the antiferromagnetic spin axis in epitaxial $LaFeO_3$ films by X-ray magnetic linear dichroism spectroscopy. *Phys. Rev. B* **67**, 214433 (2003).

[38] Folven, E. *et al.* Effects of nanostructuring and substrate symmetry on antiferromagnetic domain structure in $LaFeO_3$ thin films. *Phys. Rev. B* **84**, 220410 (2011).

[39] Takamura, Y. *et al.* Spin-flop coupling and exchange bias in embedded complex oxide micromagnets. *Phys. Rev. Lett.* **111**, 107201 (2013).

[40] Folven, E., Takamura, Y. & Grepstad, J. K. X-PEEM study of antiferromagnetic domain patterns in $LaFeO_3$ thin films and embedded nanostructures. *J. Electron Spectrosc. Relat. Phenom.* **185**, 381 (2012).

[41] Folven, E. *et al.* Crossover from spin-flop coupling to collinear spin alignment in antiferromagnetic/ferromagnetic nanostructures. *Nano Lett.* **12**, 2386 (2012).

[42] Bang, A. D. *et al.* Magnetic domain formation in ultrathin complex oxide ferromagnetic/antiferromagnetic bilayers. *Appl. Phys. Lett.* **113**, 132402 (2019).

[43] Zhao, T. *et al.* Electrical control of antiferromagnetic domains in multiferroic $BiFeO_3$ films at room temperature. *Nat. Mater.* **5**, 823 (2006).

[44] Yun, K. Y. *et al.* Structural and multiferroic properties of $BiFeO_3$ thin films at room temperature. *J. Appl. Phys.* **96**, 3399 (2019).

[45] Wang, J. *et al.* Epitaxial $BiFeO_3$ multiferroic thin film heterostructures. *Science* **299**, 1719 (2003).

[46] Zheng, R. Y., Wang, J. & Ramakrishna, S. Electrical and magnetic properties of multiferroic $BiFeO_3/CoFe_2O_4$ heterostructure. *J. Appl. Phys.* **104**, 034106 (2018).

[47] Skumryev, V. *et al.* Beating the superparamagnetic limit with exchange bias. *Nature* **423**, 850 (2003).

[48] Schlickeiser, F., Ritzmann, U., Hinzke, D. & Nowak, U. Role of entropy in domain wall motion in thermal gradients. *Phys. Rev. Lett.* **113**, 097201 (2014).

[49] Yan, Z. *et al.* Brownian motion and entropic torque driven motion of domain walls in antiferromagnets. *Phys. Rev. B* **97**, 054308 (2018).

[50] Weber, N. B., Ohldag, H., Gomonaj, H. & Hillebrecht, F. U. Magnetostrictive domain walls in antiferromagnetic NiO. *Phys. Rev. Lett.* **91**, 237205 (2003).

[51] Bode, M. *et al.* Atomic spin structure of antiferromagnetic domain walls. *Nature Materials* **5**, 477–481 (2006).

[52] Fontaíña-Troitiño, N. *et al.* Room-temperature ferromagnetism in antiferromagnetic cobalt oxide nanooctahedra. *Nano Lett.* **14**, 640 (2014).

[53] Fontaíña-Toitiño, N., Rivas-Murias, B., Rodríguez-González, B. & Salgueiriño, V. Exchange bias effect in $CoO@Fe_3O_4$ core-shell octahedron-shaped nanoparticles. *Chem. Mater.* **26**, 5566 (2014).

[54] Guardia, P., Perez, N., Labarta, A. & Batlle, X. Controlled synthesis of iron oxide nanoparticles over a wide size range. *Langmuir* **26**, 5843 (2010).

[55] Guardia, P., Labarta, A. & Batlle, X. Tuning the size, the shape, and the magnetic properties of iron oxide nanoparticles. *J. Phys. Chem. C* **115**, 390 (2011).

[56] Jana, N. R., Chen, Y. & Peng, X. Size- and shape-controlled magnetic (Cr, Mn, Fe, Co, Ni) oxide nanocrystals via a simple and general approach. *Chem. Mater.* **16**, 3931 (2004).

[57] Hyeon, T. Chemical synthesis of magnetic nanoparticles. *Chem. Commun.* 927 (2003).

[58] Woo, K. *et al.* Easy synthesis and magnetic properties of iron oxide nanoparticles. *Chem. Mater.* **16**, 2814 (2004).

[59] Koo, Y. S. *et al.* Strain-induced magnetoelectric coupling in $BaTiO_3/Fe_3O_4$ core/shell nanoparticles. *Appl. Phys. Lett.* **94**, 032903 (2019).

[60] Du, Y., Cheng, Z. X., Xue Dou, S., Attard, D. J. & Lin Wang, X. Fabrication, magnetic, and ferroelectric properties of multiferroic $BiFeO_3$ hollow nanoparticles. *J. Appl. Phys.* **109**, 073903 (2011).

[61] Kumar, A. S. *et al.* Multiferroic and magnetoelectric properties of $Ba_{0.85}Ca_{0.15}Zr_{0.1}Ti_{0.9}O_3 - CoFe_2O_4$ core-shell nanocomposite. *J. Magn. Magn. Mater.* **418**, 294 (2016).

[62] Rodríguez-González, B., Prieto-Troitiño, A., Mariño-Fernández, R., Ramos-Dacampo, M. A. & Salgueiriño, V. $CoO@MnFe_2O_4$ octahedron-shaped nanocages. *Microsc. Microanal.* **22**, 48 (2016).

[63] Chaturvedi, S. *et al.* Coercivity and exchange bias of bismuth ferrite nanoparticles isolated by polymer coating. *J. Appl. Phys.* **115**, 123906 (2019).

[64] Lv, P., Zhang, Y., Xu, R., Nie, J.-C. & He, L. Anomalous magnetic properties of 7 nm single-crystal Co_3O_4 nanowires. *J. Appl. Phys.* **111**, 013910 (2019).

[65] Hansen, M. F., Koch, C. B. & Mørup, S. Magnetic dynamics of weakly and strongly interacting hematite nanoparticles. *Phys. Rev. B* **62**, 1124 (2000).

[66] Theil Kuhn, L. *et al.* Neutron study of magnetic excitations in 8-nm α-Fe_2O_3 nanoparticles. *Phys. Rev. B* **74**, 184406 (2006).

[67] Frandsen, C. & Mørup, S. Inter-particle interactions in composites of antiferromagnetic nanoparticles. *J. Magn. Magn. Mater.* **266**, 36 (2003).

[68] Madsen, D. E., Hansen, M. F., Koch, C. B. & Mørup, S. Interactions between goethite particles subjected to heat treatment. *J. Phys. Condens. Matter* **20**, 135215 (2008).

[69] Brok, E. *et al.* Magnetic properties of ultra-small goethite nanoparticles. *J. Phys. D: Appl. Phys.* **47**, 365003 (2014).

[70] Valezi, D. P. *et al.* Goethite ($\alpha - \mathrm{FeOOH}$) magnetic transition by ESR, magnetometry and Mössbauer. *Mater. Chem. Phys.* **173**, 179 (2016).

[71] Brok, E., Lefmann, K., Nilsen, G. J., Kure, M. & Frandsen, C. Off-axis spin orientation in goethite nanoparticles. *Phys. Rev. B* **96**, 104426 (2017).

[72] Coey, J. M. D. *et al.* Spin flop in goethite. *J. Phys. Condens. Matter* **7**, 759 (1995).

[73] Pankhurst, Q. A., Barquín, L. F., Lord, J. S., Amato, A. & Zimmermann, U. Intrinsic magnetic relaxation in goethite. *Phys. Rev. B* **85**, 174437 (2012).

[74] Nedelkoski, Z. *et al.* Origin of reduced magnetization and domain formation in small magnetite nanoparticles. *Sci. Rep.* **7**, 45997 (2017).

[75] Balan, A. *Studying individual magnetic nanoparticles with X-ray PEEM.* Ph.D. thesis, University of Basel (2014).

[76] Balan, A. *et al.* Direct observation of magnetic metastability in individual iron nanoparticles. *Phys. Rev. Lett.* **112**, 107201 (2014).

[77] Balan, A., Fraile Rodríguez, A., Vaz, C. A. F., Kleibert, A. & Nolting, F. Effect of substrate interface on the magnetism of supported iron nanoparticles. *Ultramicroscopy* **159**, 513 (2015).

[78] Kleibert, A. *et al.* Direct observation of enhanced magnetism in individual size- and shape-selected 3*d* transition metal nanoparticles. *Phys. Rev. B* **95**, 195404 (2017).

[79] Kleibert, A., Rosellen, W., Getzlaff, M. & Bansmann, J. Structure, morphology, and magnetic properties of Fe nanoparticles deposited onto single-crystalline surfaces. *Beilstein J. Nannotechnol.* **2**, 47 (2011).

[80] Stöhr, J. *et al.* Images of the antiferromagnetic structure of a NiO(100) surface by means of X-ray magnetic linear dichroism spectromicroscopy. *Phys. Rev. Lett.* **83**, 1862 (1999).

[81] Nolting, F. *et al.* Direct observation of the alignment of ferromagnetic spins by antiferromagnetic spins. *Nature* **405**, 767 (2000).

[82] van der Laan, G. Magnetic linear X-ray dichroism as a probe of the magnetocrystalline anisotropy. *Phys. Rev. Lett.* **82**, 640 (1999).

[83] van der Laan, G., Schofield, P. F., Cressey, G. & Henderson, C. M. B. Natural linear dichroism at the Fe 2p absorption edge of gillespite. *Chem. Phys. Lett.* **252**, 272 (1996).

[84] Kuneš, J. & Oppeneer, P. M. Anisotropic x-ray magnetic linear dichroism at the $L_{2,3}$ edges of cubic Fe, Co, and Ni: *Ab initio* calculations and model theory. *Phys. Rev. B* **67**, 024431 (2003).

[85] Li, Z. A. *et al.* Electrostatic doping as a source for robust ferromagnetism at the interface between antiferromagnetic cobalt oxides. *Sci. Rep.* **5**, 7997 (2015).

[86] Cornell, R. M. & Schwertmann, U. *The Iron Oxides: Strucutre, Properties, Reactions, Occurence and Uses*, chap. 2. Crystal structure, 9–38 (Wiley-VCH, 2004), 2nd edition edn.

[87] Cornell, R. M. & Schwertmann, U. *The Iron Oxides: Strucutre, Properties, Reactions, Occurence and Uses*, chap. 4. Crystal morphology and size, 59–94 (Wiley-VCH, 2004).

[88] Cornell, R. M. & Schwertmann, U. *The Iron Oxides: Strucutre, Properties, Reactions, Occurence and Uses*, chap. Snthesis, 525–540 (Wiley-VCH, 2004).

[89] Frandsen, C., Madsen, D. E., Boothroyd, C. B. & Mørup, S. Anomalous particle size dependence of magnetic relaxation phenomena in goethite nanoparticles. *Croat. Chem. Acta* **88**, 481 (2015).

[90] Bocquet, S., Pollard, R. J. & Cashion, J. D. Dynamic magnetic phenomena in fine-particle goethite. *Phys. Rev. B* **46**, 11657 (1992).

[91] Brož, D. & Sedlàk, B. Surface ferrimagnetism of synthetic goethite. *J. Magn. Magn. Mater* **102**, 103 (1991).

[92] Bocquet, S. & Hill, A. J. Correlation of Néel temperature and vacancy defects in fine-particle goethites. *Phys. Chem. Miner* **22**, 524 (1995).

[93] Madsen, D. E. *et al.* Magnetic fluctuations in nanosized goethite ($\alpha - \mathrm{FeOOH}$) grains. *J. Phys. Condens. Matter* **21**, 016007 (2009).

[94] Cornell, R. M. & Schwertmann, U. *The Iron Oxides: Strucutre, Properties, Reactions, Occurence and Uses*, chap. 14. Transformations, 365–407 (Wiley-VCH, 2004).

[95] Özdemir, Ö. & Dunlop, D. J. Intermediate magnetite formation during dehydration of goethite. *Earth and Planetary Science Letters* **177**, 59 (2000).

[96] Gualtieri, A. F. & Venturelli, P. In situ study of the goethite-hematite phase transformation by real time synchrotron powder diffraction. *Amer. Miner.* **84**, 895 (1999).

[97] Pérez-Maqueda, L., Criado, J., Subrt, J. & Real, C. Synthesis of acicular hematite catalysts with tailored porosity. *Catal. Lett.* **60**, 151 (1999).

[98] Cornell, R. M. & Schwertmann, U. *The Iron Oxides: Strucutre, Properties, Reactions, Occurence and Uses*, chap. 6. Electronic, electrical and magnetic properties and colour, 111–137 (Wiley-VCH, 2004).

[99] Jauch, W., Reehuis, M., Bleif, H. J., Kubanek, F. & Pattison, P. Crystallographic symmetry and magnetic structure of CoO. *Phys. Rev. B* **64**, 052102 (2001).

[100] Greenwald, S. The antiferromagnetic structure deformations in CoO and MnTe. *Acta Crystallogr.* **6**, 396 (1953).

[101] Clendenen, R. L. & Drickamer, H. G. Lattice parameters of nine oxides and sulfides as a function of pressure. *J. Chem. Phys.* **44**, 4223 (1966).

[102] Saito, S., Nakahigashi, K. & Shimomura, Y. X-ray diffraction study on CoO. *J. Phys. Soc. Jpn.* **21**, 850 (1966).

[103] Herrmann-Ronzaud, D., Bwebet, P. & Rossat-Mignod, J. Equivalent type-II magnetic structures: CoO, a collinear antiferromagnet. *J. Phys. C: Solid State Phys.* **11**, 2123 (1978).

[104] Kanamori, J. Theory of the Magnetic Properties of Ferrous and Cobaltous Oxides, I. *Prog. Theor. Phys.* **17**, 177 (1957).

[105] Kanamori, J. Theory of the Magnetic Properties of Ferrous and Cobaltous Oxides, II. *Prog. Theor. Phys.* **17**, 197 (1957).

[106] Zhang, L., Xue, D. & Gao, C. Anomalous magnetic properties of antiferromagnetic CoO nanoparticles. *Journal of Magnetism and Magnetic Materials* **267**, 111 (2003).

[107] Dutta, D. P., Sharma, G., Manna, P. K., Tyagi, A. K. & Yusuf, S. M. Room temperature ferromagnetism in CoO nanoparticles obtained from sonochemically synthesized precursors. *Nanotechnol* **19**, 245609 (2008).

[108] Yang, G. *et al.* Room temperature ferromagnetism in vacuum-annealed CoO nanospheres. *The Journal of Physical Chemistry C* **114**, 21989 (2010).

[109] Kodama, R. H., Makhlouf, S. A. & Berkowitz, A. E. Finite size effects in antiferromagnetic nio nanoparticles. *Phys. Rev. Lett.* **79**, 1393 (1997).

[110] Flipse, C. F. J., Rouwelaar, C. B. & de Groot, F. M. F. Magnetic properties of CoO nanoparticles. *The European Physical Journal D - Atomic, Molecular, Optical and Plasma Physics* **9**, 479 (1999).

[111] Han, M. J., Kim, H.-S., Kim, D. G. & Yu, J. Collinear and noncollinear spin ground state of wurtzite CoO. *Phys. Rev. B* **87**, 184432 (2013).

[112] Alaria, J., Cheval, N., Rode, K., Venkatesan, M. & Coey, J. M. D. Structural and magnetic properties of wurtzite CoO thin films. *J. Phys. D: Appl. Phys.* **41**, 135004 (2008).

[113] Risbud, A. S., Snedeker, L. P., Elcombe, M. M., Cheetham, A. K. & Seshadri, R. Wurtzite CoO. *Chem. Mater.* **17**, 834 (2005).

[114] Buck, M. R., Biacchi, A. J. & Schaak, R. E. Insights into the thermal decomposition of Co(II) oleate for the shape-controlled synthesis of wurtzite-type CoO nanocrystals. *Chem. Mater.* **26**, 1492 (2014).

[115] He, X. *et al.* Transition temperature of wurtzite CoO nanocrystals as revealed in comprehensive magnetic characterization. *The Journal of Physical Chemistry C* **118**, 13898 (2014).

[116] Roca, A. G. *et al.* Unravelling the elusive antiferromagnetic order in wurtzite and zinc blende CoO polymorph nanoparticles. *Small* **14**, 1703963 (2018).

[117] Gao, D. *et al.* Room temperature ferromagnetism of pure ZnO nanoparticles. *Journal of Applied Physics* **105**, 113928 (2019).

[118] Straumal, B. B. *et al.* Magnetization study of nanograined pure and Mn-doped ZnO films: Formation of a ferromagnetic grain-boundary foam. *Phys. Rev. B* **79**, 205206 (2009).

[119] Potzger, K., Zhou, S., Grenzer, J., Helm, M. & Fassbender, J. An easy mechanical way to create ferromagnetic defective ZnO. *Appl. Phys. Lett.* **92**, 182504 (2019).

[120] Roth, W. The magnetic structure of Co_3O_4. *Journal of Physics and Chemistry of Solids* **25**, 1 (1964).

[121] Makhlouf, S. A. Magnetic properties of Co_3O_4 nanoparticles. *J. Magn. Magn. Mater.* **246**, 184 (2002).

[122] Zhang, Y., Chen, Y., Wang, T., Zhou, J. & Zhao, Y. Synthesis and magnetic properties of nanoporous Co_3O_4 nanoflowers. *Microporous and Mesoporous Materials* **114**, 257 (2008).

[123] Ichiyanagi, Y. & Yamada, S. The size-dependent magnetic properties of Co_3O_4 nanoparticles. *Polyhedron* **24**, 2813 (2005).

[124] He, L., Chen, C., Wang, N., Zhou, W. & Guo, L. Finite size effect on Néel temperature with Co_3O_4 nanoparticles. *J Appl. Phys* **102**, 103911 (2007).

[125] Ichiyanagi, Y., Kimishima, Y. & Yamada, S. Magnetic study on Co_3O_4 nanoparticles. *Journal of Magnetism and Magnetic Materials* **272-276**, E1245 (2004). Proceedings of the International Conference on Magnetism (ICM 2003).

[126] Zhu, H. *et al.* Synthesis and magnetic properties of antiferromagnetic Co_3O_4 nanoparticles. *Physica B: Condensed Matter* **403**, 3141 (2008).

[127] Steglich, M., Knopp, G. & Hemberger, P. How the methyl group position influences the ultrafast deactivation in aromatic radicals. *Phys. Chem. Chem. Phys.* **21**, 581 (2019).

[128] Antoshvili, M., Caspy, I., Hippler, M. & Nelson, N. Structure and function of photosystem I in cyanidioschyzon merolae. *Photosynthesis Research* **139**, 499 (2019).

[129] Janssens, K. *et al.* The use of synchrotron radiation for the characterization of artists' pigments and paintings. *Annual Review of Analytical Chemistry* **6**, 399 (2013).

[130] Smith, G. D. Infrared microspectroscopy using a synchrotron source for arts-science research. *Journal of the American Institute for Conservation* **42**, 399 (2003).

[131] Stöhr, J. & Samant, M. Liquid crystal alignment by rubbed polymer surfaces: a microscopic bond orientation model. *Journal of Electron Spectroscopy and Related Phenomena* **98-99**, 189 (1999).

[132] Lüdeke, A. *et al.* Status of the Swiss Light Source. *Proceedings of EPAC 2006* (2006).

[133] Mobilio, S. & Boscherini, F. *Synchrotron Radiation: Basics, Methods and Applications*, chap. 1-30, 1–784 (Springer, 2015).

[134] Chen, C. T., Sette, F., Ma, Y. & Modesti, S. Soft-x-ray magnetic circular dichroism at the $L_{2,3}$ edges of nickel. *Phys. Rev. B* **42**, 7262 (1990).

[135] Kuch, W. *et al.* Magnetic-circular-dichroism microspectroscopy at the spin reorientation transition in Ni(001) films. *Phys. Rev. B* **62**, 3824 (2000).

[136] van der Laan, G. *et al.* Orbital polarization in $NiFe_2O_3$ measured by Ni $-2p$ x-ray magnetic circular dichroism. *Phys. Rev. B* **59**, 4314 (1999).

[137] Cheng, X. M. & Keavney, D. J. Studies of nanomagnetism using synchrotron-based x-ray photoemission electron microscopy (X-PEEM). *Rep. Prog. Phys.* **75**, 026501 (2012).

[138] Stöhr, J. & Siegmann, H. C. *Magnetism From Fundamentals to Nanoscale Dynamics*, chap. 9. Interactions of Polarized Photons with Matter, 351–430 (Springer, 2006).

[139] Chen, C. T. *et al.* Out-of-plane orbital characters of intrinsic and doped holes in $La_{(2-x)}Sr_xCuO_4$. *Phys. Rev. Lett.* **68**, 2543 (1992).

[140] Chmiel, F. P. *et al.* Observation of magnetic vortex pairs at room temperature in a planar α-Fe_2O_3/Co heterostructure. *Nat. Mater* **17**, 581 (2018).

[141] Zhou, W., Apkarian, R., Wang, Z. L. & Joy, D. *Fundamentals of Scanning Electron Microscopy (SEM)* (Springer New York, New York, NY, 2007).

[142] Williams, D. B. & Carter, C. B. *Transmission electron microscopy* (Springer, 2009).

[143] Larsen, P. K. & Dobson, P. J. *Reflection High-Energy Electron Diffraction and Reflection Electron Imaging of Surfaces* (Springer).

[144] Pecharsky, V. & Zavalij, P. *Fundamentals of Powder Diffraction and Structural Characterization of Materials* (Springer, 2009).

[145] Ramos-Docampo, M. A., Rivas-Murias, B., Rodríguez-González, B. & Salgueiriño, V. Thermodynamically driven oxidation-induced kirkendall effect in octahedron-shaped cobalt oxide nanocrystals. *CrystEngComm* **19**, 5542 (2017).

[146] Joshi, N. *et al.* Microbial reduction of natural Fe(III) minerals; toward the sustainable production of functional magnetic nanoparticles. *Front. Env. Sci. Eng.* **6**, 1 (2018).

[147] Hodych, J. P., Pätzold, R. R. & Buchnan, K. L. Paleomagnetic dating of the transformation of oolitic goethite to hematite in iron ore. *Can. J. Earth Sci* **21**, 127 (1984).

[148] Rochette, P. & Fillion, G. Field and temperature behavior of remanence in synthetic goethite: Paleomagnetic implications. *Geophys. Res. Lett* **16**, 851 (1989).

[149] Cornell, R. M., Mann, S. & Skarnulis, A. J. A high-resolution electron microscopy examination of domain boundaries in crystals of synthetic goethite. *J. Chem. Soc. Faraday T* **79**, 2679 (1983).

[150] Kaur, N., Singh, B., Kennedy, B. J. & Gräfe, M. The preparation and characterization of vanadium-substituted goethite: The importance of temperature. *Geochim. Cosmochim. Ac* **73**, 582 (2009).

[151] de Grave, E. & Vandenberghe, R. E. 57Fe Mössbauer effect study of well-crystallized goethite (α-FeOOH). *Hyperfine Interact* **28**, 643 (1986).

[152] Zepeda-Alarcon, E. *et al.* Magnetic and nuclear structure of goethite (α-FeOOH): a neutron diffraction study. *J. Appl. Crystallogr* **47**, 1983 (2014).

[153] Li, J. *et al.* Continuous spin reorientation transition in epitaxial antiferromagnetic NiO thin films. *Phys. Rev. B* **84**, 012406 (2011).

[154] Zhu, J. *et al.* Strain-modulated antiferromagnetic spin orientation and exchange coupling in Fe/CoO(001). *Journal of Applied Physics* **115**, 193903 (2014).

[155] Souza, T. G. F., Ciminelli, V. S. T. & Mohallem, N. D. S. A comparison of TEM and DLS methods to characterize size distribution of ceramic nanoparticles. *Journal of Physics: Conference Series* **733**, 012039 (2016).

[156] Momma, K. & Izumi, F. *VESTA3* for three-dimensional visualization of crystal, volumetric and morphology data. *J. Appl. Crystalogr* **44**, 1272 (2011).

[157] ICDS 163341 (2009).

[158] Patterson, A. L. The Scherrer Formula for X-Ray Particle Size Determination. *Phys. Rev.* **56**, 978 (1939).

[159] Kleibert, A., Voitkans, A. & Meiwes-Broer, K.-H. Size-dependent alignment of Fe nanoparticles upon deposition onto W(110). *Phys. Rev. B* **81**, 073412 (2010).

[160] ICDS 15840 (2013).

[161] Blake, R. L., Hessevick, R. E., Zoltai, T. & Finger, L. W. Refinement of the hematite structure. *Amer. Miner.* **51**, 123 (1966).

[162] AMCSD 0020517 (2014).

[163] Solano, E. *et al.* Neutron and X-ray diffraction study of ferrite nanocrystals obtained by microwave-assisted growth. A structural comparison with the thermal synthetic route. Corrigendum. *J. Appl. Crystallogr* **47**, 1478 (2014).

[164] Bartling, S., Pohl, M.-M., Meiwes-Broer, K.-H. & Barke, I. Morphological impact on the reaction kinetics of size-selected cobalt oxide nanoparticles. *J. Chem. Phys* **143**, 114301 (2015).

[165] Kocks, U. F., Tomé, C. N. & Wenk, H.-R. *Texture and anisotropy: Preferred orientation in polycrystals and their effects on materials properties* (Camebridge University Press, Camebridge, 2000).

[166] von der Heyden, B. P., Roychoudhury, A. N., Tyliszczak, T. & Myneni, S. C. B. Investigating nanoscale mineral compositions: Iron L_3-edge spectroscopic evaluation of iron oxide and oxy-hydroxide coordination. *Amer. Miner.* **102**, 674 (2017).

[167] van Aken, P. A., Liebscher, B. & Styrsa, V. J. Quantitative determination of iron oxidation states in minerals using Fe $L_{2,3}$-edge electron energy-loss near-edge structure spectroscopy. *Phys. Chem. Miner.* **25**, 323 (1998).

[168] Cressey, G., Henderson, C. M. B. & van der Laan, G. Use of L-edge X-ray absorption spectroscopy to characterize multiple valence states of 3d transition metals; a new probe for mineralogical and geochemical research. *Phys. Chem. Miner* **20**, 111 (1993).

[169] Miedema, P. S. & de Groot, F. M. The iron l edges: Fe 2p X-ray absorption and electron energy loss spectroscopy. *J. Electron Spectrosc* **187**, 32 (2013).

[170] Calvert, C. C., Brown, A. & Brydson, R. Determination of the local chemistry of iron in inorganic and organic materials. *J. Electron Spctrosc* **143**, 173 (2005). Electron Energy Loss Spectroscopy in the Electron Microscope.

[171] Gota, S., Gautier-Soyer, M. & Sacchi, M. Fe $2p$ absorption in magnetic oxides: Quantifying angular-dependent saturation effects. *Phys. Rev. B* **62**, 4187 (2000).

[172] Regan, T. J. *et al.* Chemical effects at metal/oxide interfaces studied by x-ray-absorption spectroscopy. *Phys. Rev. B* **64**, 214422 (2001).

[173] Nakajima, R., Stöhr, J. & Idzerda, Y. U. Electron-yield saturation effects in l-edge x-ray magnetic circular dichroism spectra of Fe, Co, and Ni. *Phys. Rev. B* **59**, 6421 (1999).

[174] Fauth, K. How well does total electron yield measure x-ray absorption in nanoparticles? *Applied Physics Letters* **85**, 3271 (2004).

[175] Kleibert, A., Meiwes-Broer, K.-H. & Bansmann, J. Size-dependent magnetic spin and orbital moments of fe nanoparticles deposited onto Co/W(110). *Phys. Rev. B* **79**, 125423 (2009).

[176] Hallsteinsen, I. *et al.* Magnetic domain configuration of (111)-oriented $LaFeO_3$ epitaxial thin films. *APL Materials* **5**, 086107 (2017).

[177] Gota, S., Gautier-Soyer, M. & Sacchi, M. Magnetic properties of Fe_2O_3(0001) thin layers studied by soft x-ray linear dichroism. *Phys. Rev. B* **64**, 224407 (2001).

[178] Czekaj, S. M. *Ferromagnetic and antiferromagnetic domain configurations in thin films and multilayers towards a patterned exchange bias.* Ph.D. thesis, ETH Zürich (2007).

[179] Yamamoto, A., Honmyo, T., Hosoito, N., Kiyama, M. & Shinjo, T. Surface magnetism of -feooh by mössbauer spectroscopy. *Nucl. Instrum. Methods B* **76**, 202 (1993).

[180] Bansmann, J. *et al.* Magnetic and structural properties of isolated and assembled clusters. *Surf. Sci. Rep* **56**, 189 (2005).

[181] Martins, M. & Wurth, W. Magnetic properties of supported metal atoms and clusters. *J. Phys. Condens. Matter* **28**, 503002 (2016).

[182] Morales, F. *et al.* In situ x-ray absorption of $Co/Mn/TiO_2$ catalysts for Fischer-Tropsch synthesis. *J. Phys. Chem. B* **108**, 16201 (2004).

[183] Bergmann, A. *et al.* Reversible amorphization and the catalytically active state of crystalline Co_3O_4 during oxygen evolution. *Nat. Commun* **6**, 8625 (2015).

[184] Wu, J. *et al.* Direct measurement of rotatable and frozen CoO spins in exchange bias system of CoO/Fe/Ag(001). *Phys. Rev. Lett.* **104**, 217204 (2010).

[185] Kampfrath, T. *et al.* Coherent terahertz control of antiferromagnetic spin waves. *Nature Photonics* **5**, 31–34 (2011).

[186] Nagesetti, A. *et al.* Multiferroic coreshell magnetoelectric nanoparticles as nmr sensitive nanoprobes for cancer cell detection. *Scientific Reports* **7**, 1610 (2017).

[187] Langer, M. *et al.* Development of a new soft x-ray ptychography spectro-microscope at the swiss light source (sls). *Microscopy and Microanalysis* **24**, 54 (2018).

List of Figures

Appendix A

RHEED

In Fig. A.1 (a) the geometry of the RHEED setup is shown. It can be seen that the electron with an energy of 30 kV impinges in a very grazing angle ($\Theta < 1°$) on the sample. The diffracted electrons then are collected by an fluorescence screen. In order to get a digital image of the screen a CCD camera is used. In the schematic drawing the distance between the center of the sample and the screen (L = 341.6 mm) and the width of pipe in which the fluorescence screen is mounted (l = 164 mm). In Fig. A.1 (b) an image of the fluorescence screen as obtain by the CCD camera is shown. The width of the screen l is indicated again by the outer white circle. The inner white circle displays shows the active area of the fluorescence screen. Here the width of the detector ($l' = 138.6$ mm, and p = 524 px) is indicated in pixels and in mm. The ratio of the two yields R = 0.2645 mm/px. Determining R was important to calculate the diffraction angles and consequently the values in q space.

An individual RHEED pattern is recorded for 1 s and this was repeated 1000 times. The final RHEED data set is the average of those 1000 individual images. To obtain the RHEED curves one had to extract radial profiles. In order to get the diffraction pattern with respect to the scattering vector the pixel scale (s) was transformed into units of $Å^{-1}$. This was straight forwardly done by the following equations:

$$2\Theta = atan\Big(\frac{s * [px] * R}{L}\Big) \tag{A.1}$$

$$q = \frac{4\pi sin(\Theta)}{\lambda} \tag{A.2}$$

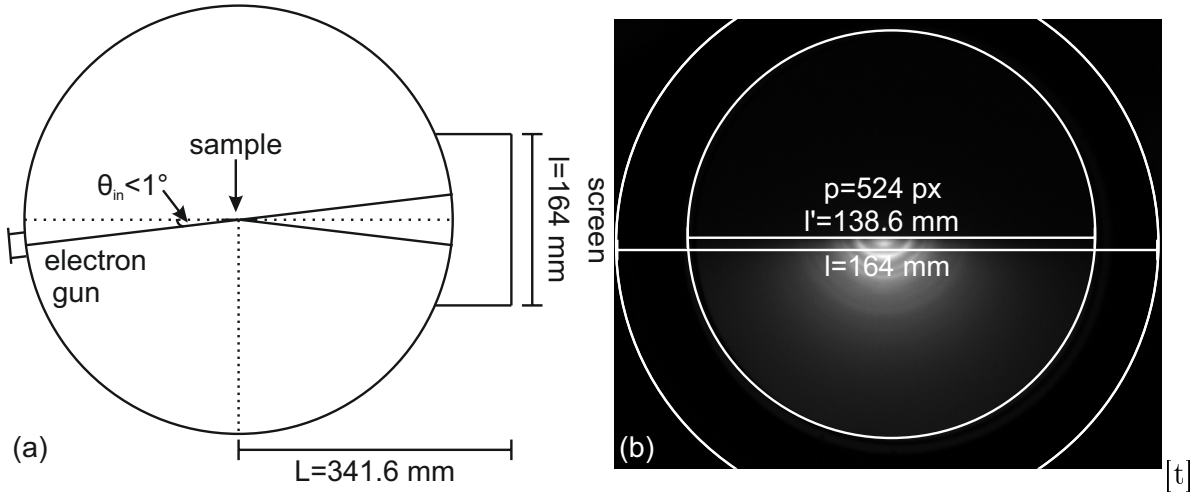

[t]

FIG. A.1: (a) displays the experimental geometry of the RHEED measurements. The location of the electron gun, the sample, and the fluorescence screen are shown. Further the very grazing incident angle ($\Theta < 1°$) of the electron gun as well as the distance between the sample location and the fluorescence screen (L) and the size of the screen (l) are shown. (b) shows an image of the screen as experimentally obtained with l drawn in as well as l' in mm and px. All the numerical values in (a) and (b) are needed to transfer the scale from pixels to units of q in the end.

Where 2Θ the scattering angle and λ the relativistic de Broglie wavelength ($\lambda = 6.88 * 10^{-12}$ m) of the electrons.

Appendix B

Spin axis of individual nanoparticles

Figure B.1 displays the possible spin axis of NP C, E, and F. In panels (a), (d), and (g) the SEM images are shown as already discussed in the main part of the thesis. The panels (b)-(c), (e)-(f), and (h)-(i) display the orientations which theoretically are possible. The axis are colored to point out the main direction the spin axis along the [001] (red), [010] (green), and [100] (blue), respectively. It seems obvious that the measured spin axis can only be possibly consistent with the red set of spin axis. The reason for this is that the by convention the [001] of the individual crystals is chosen as the direction which matches the spin axis the closest. This convention is set since the in literature the spin axis is usually described to follow the z-direction of the crystal forms the tetragonal distortion axis of CoO [17, 104, 105] if it is cooled through the Néel temperature. Thus, in the main part of the work only the red set of spin axis is displayed in Fig. 6.9.

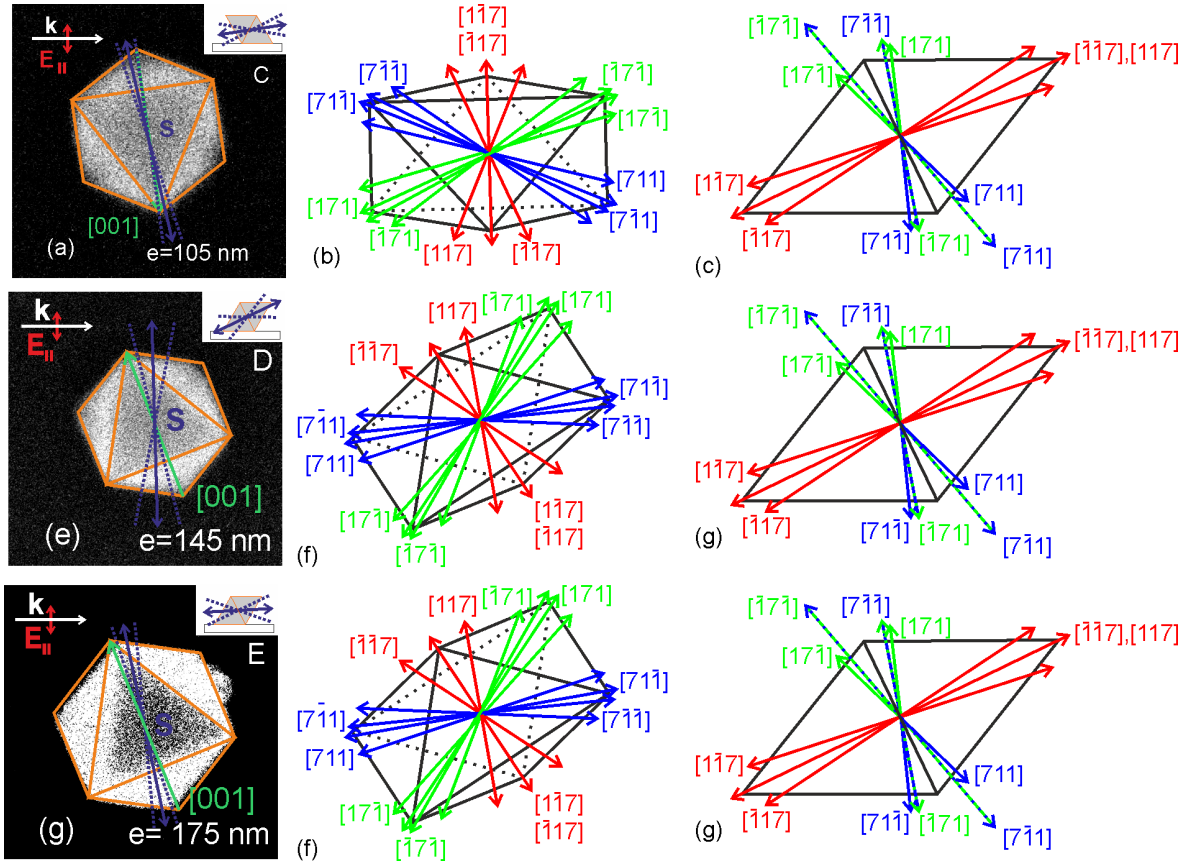

FIG. B.1: (a) SEM image of NP C, the possible spin axis orientation parallel and perpendicular to the sample plane in (b) and (c), respectively. For better visibility the spin axis which dominantly follow the [001],[010], and [100] directions are colored red, green, and blue. According to the same scheme the possible spin axis for NP D and E are displayed in the panels (d)-(f) and (g)-(i).

Appendix C

Publication list

- D. Bracher, *Determining the antiferromagnetic spin axis of individual* CoO/Co_3O_4 *core-shell nanoparticles.* (in preparation)
- D. Bracher, T. M. Savchenko, M. Wyss, P. Üresin, A. Goel, G. Olivieri, M. A. Brown, F. Nolting, C. A. F. Vaz, M. Poggio, and A. Kleibert, *'Room temperature antiferromagnetic order in individual and agglomerated goethite nanoparticles.'* (in preparation)
- Jaianth Vijayakumar, Yu Li, David Bracher, Craig W. Barton, Michael Horisberger, Thomas Thomson, Jim Miles, Christoforos Moutafis, Frithjof Nolting, and C.A.F. Vaz, Phys. Rev. Applied **14**, 054031 (2020)
- T. M. Savchenko, M. Buzzi, L. Howald, S. Ruta, J. Vijayakumar, M. Timm, D. Bracher, S. Saha, L. J. Heydermann, U. Nowak, P. M. Derlet, R. W. Chantrell, C. A. F. Vaz, F. Nolting, and A. Kleibert, Phys. Rev. B **102**, 205418 (2020)
- M. Saccone, K. Hofhuis, D. Bracher, A. Kleibert, S. van Dijken, and A. Farhan, Nanoscale **12**, 189 (2020)
- V. N . Strocov, A. Chikina, M. Caputo, M.-A. Husanu, F. Bisti, D. Bracher, T. Schmitt, F. Miletto, C. A. F. Vaz, and F. Lechermann, Phys. Rev. Mater **3**, 106001 (2019).
- J. Mendil, M. Tassin. Q. Bu, J. Schaab, M. Baumgartner, C. Murer, P. T. Dao, J.

Vijayakumar, D. Bracher, C. Bouillet, C. A. F. Vaz, M. Fiebig, and P. Gambardella, Phys. Rev. Materials **3**, 034403 (2019).

- J. Vijayakumar, D. Bracher, T. M. Savchenko, M. Horisberger, F. Nolting, C. A. F. Vaz, J. Appl. Phys. **125**, 114101 (2019).

- S. Finizio, S. Wintz, D. Bracher, E. Kirk, A. S. Semisalova, J. Förster, K. Zeissler, T. Weissels, M. Weigand, K. Lenz, A. Kleibert, and J. Raabe, Phys. Rev. B **98**, 104415 (2018).

- K. Zeissler, S. Finizio, K. Shahbazi, J. Massey, F. A. Ma'Mari, D. Bracher, A. Kleibert, M. C. Rosamond, E. H. Linfield, T. A. Moore, J. Raabe, G. Bunell, and C. H. Marrows, Nat. Nanotechnol. **13**, 1161 (2018).

Appendix D

Conference/School contributions

2019

- **Antiferromagnetic order probed in individual 3d transition metal oxide nanoparticles.** (poster)
  D. Bracher, T. M. Savchenko, M. Testa Anta, M. Wyss, A. Goel, G. Olivieri, M. A. Brown, S. Sagueiriño, C. A. F. Vaz, M. Poggio, and A. Kleibert, *SNI Annual Meeting 2019*, 2019-09-12, Lenzerheide, Switzerland

- **Probing antiferromagnetic ordering in individual CoO/Co_3O_4 core shell nanopaticles.** (contributed talk)
  D. Bracher, T. M. Savchenko, M. Testa Anta, M. Wyss, F. Nolting, V. Salgueiriño,M. Poggio, and A. Kleibert, *ICFPM 2019*, 2019-05-29, Gijon, Spain

- **Towards determining the spin axis of individual CoO nanoparticles.** (contributed talk)
  D. Bracher, T. M. Savchenko, M. Testa Anta,V. Salgueiriño, F. Nolting, M. Poggio, and A. Kleibert, *DPG Frühjahrstagung 2019*, 2019-04-04, Regensburg, Germany

2018

- **Probing antiferromagnetic order in individual 3d transition metal oxide nanoparticles.** (poster)

D. Bracher, T. M. Savchenko, M. Testa Anta, M. Wyss, G. Olivieri, M. A. Brown, F. Nolting, C. A. F. Vaz, M. Poggio, and A. Kleibert, *Qunaty Workshop 2018*, 2018-09-26, Heidelberg, Germany

- **Antiferromagnetic properties of individual polycrystalline goethite nanoparticles studied by temperature and orientation dependent X-ray spectromicroscopy.** (contributed talk)
  D. Bracher, T. M. Bracher, M. Wyss, G. Olivieri, M. A. Brown, F. Nolting, M. Poggio, and A. Kleibert, *SNI Annual Meeting 2018*, 2018-09-14, Lenzerheide, Switzerland

- **Antiferromagnetic properties of individual goethite nanoparticles studied by temperature and azimuthal dependent XLD spectromicroscopy.** (contributed talk)
  D. Bracher, T. M. Savchenko, M. Wyss, G. Olivieri, M. A. Brown, F. Nolting, M. Poggio, and A. Kleibert, *SPS Annual Meeting 2018*, 2018-08-28, Lausanne, Switzerland

- **X-ray linear dichroism to probe the antiferromagnetic properties of individual polycrystalline goethite nanoparticles.** (poster)
  D. Bracher, T. M. Savchenko, M. Wyss, G. Olivieri, M. A. Brown, F. Nolting, M. Poggio, and A. Kleibert, *Swiss Nano Convention 2018*, 2018-06-06, Zürich, Switzerland

- **Antiferromagnetic order in individual goethite nanoparticles.** (poster)
  D. Bracher, T. M. Savchenko, M. Wyss, G. Olivieri, M. A. Brown, F. Nolting, M. Poggio, and A. Kleibert, *DPG Frühjahrstagung 2018*, 2018-03-12, Berlin, Germany

2017

- **Investigating the chemical and magnetic properties of individual goehtite nanoparticles.** (poster)
  D. Bracher, T. M. Savchenko, M. Wyss, G. Olivieri, M. A. Brown, F. Nolting, M.

Poggio, and A. Kleibert, *DPG School on Magnetism 2017*, 2017-09-19, Bad Honnef, Germany

- **Probing the chemical and magnetic properties of individual goethite nanoparticles.** (poster)
  D. Bracher, T. M. Savchenko, M. Wyss, G. Olivieri, M. A. Brown, F. Nolting, M. Poggio, A. Kleibert, *SNI Annual Meeting 2017*, 2017-09-14, Lenzerheide, Switzerland

- **Antiferromagnetic ordered probed in individual goethite nanoparticles.** (contributed talk)
  D. Bracher, T. M. Savchenko, M. Wyss, G. Olivieri, M. A. Brownm F. Nolting, M. Poggio, and A. Kleibert, *Joint Annual Meeting of SPS and ÖPG*, 2017-08-25, Geneva, Switzerland

- **Correlating magnetism and morphology of individual goehtite nanoparticles.** (poster)
  D. Bracher, T. M. Bracher, M. Wyss, G. Olivieri, M. A. Brown, F. Nolting, M. Poggio, and A. Kleibert, *Swiss Nano Convention*, 2017-06-01, Fribourg, Switzerland

- **Direct observation of room temperature antiferromagnetism in individual goethite nanoparticles.** (contributed talk)
  D. Bracher, T. M. Savchenko, M. Wyss, G. Olivieri, M. A. Brown, F. Nolting, M. Poggio, and A. Kleibert, *IEEE International Magnetics Conference INTERMAG Europe 2017*, 2017-04-27, Dublin, Ireland

- **Investigating magnetism in nano-sized goethite particles.** (contributed talk)
  D. Bracher, T. M. Savchenko, M. Wyss, G. Olivieri, M. A. Brown, F. Nolting, M. Poggio, and A. Kleibert, *DPG Frühjahrstagung 2017*, 2017-03-24, Dresden, Germany

2016

- **Chemical and magnetic characterization of goethite nanoparticles by means of X-ray photo emission electron microscopy** (poster)

D. Bracher, T. M. Savchenko, M. Wyss, F. Nolting, M. Poggio, and A. Kleibert, *SNI Annual Meeting 2016*, 2016-09-15, Lenzerheide, Switzerland

- **Investigating individual magnetic metal oxide nanoparticles using X-ray photo-emission electron microscopy.** (poster)
  D. Bracher, T. M. Savchenko, M. Wyss, F. Nolting, M. Poggio, and A. Kleibert, *SPS Annual Meeting 2016*, 2016-08-23, Lugano, Switzerland

- **Probing the magnetic and chemical properties of individual metal oxide nanoparticles by means of X-ray photo-emission electron microscopy.** (poster)
  D. Bracher, T. M. Bracher, M. Wyss, F. Nolting, M. Poggio, and A. Kleibert, *Swiss Nano Convention 2016*, 2016-06-31, Basel, Switzerland

- **Investigating individual bismuth ferrite, cobalt oxide and iron oxide nanoparticles by means of X-ray photo-emission electron microscopy.** (poster)
  D. Bracher, T. M. Savchenko, M. Wyss, F. Nolting, M. Poggio, and A. Kleibert, *39th International Conference on Ultraviolet and X-ray Physics*, 2016-06-03, Zürich, Switzerland

Curriculum vitae

Personal information:

Name:	David M. Bracher
Address:	Vorstadt 2, 5200 Brugg AG
Date of birth:	15th of July 1989
Nationality:	Swiss

RESEARCH EXPERIENCE & EDUCATION

2016 - 2020 **PhD in Nanoscience, Paul Scherrer Institut/University of Basel**

- Project title: 'Antiferromagnetic properties of 3d transition metal oxide nanoparticles'.
- Collaboration with University of Vigo, ES.
- Various presentation at international conferences.
- 2 publications in preparation.
- Methods used: x-ray photoemission electron microscopy, scanning transmission x-ray microscopy, scanning electron microscopy, transmission electron microscopy, x-ray diffraction, reflection high energy electron diffraction.
- Developed analysis scripts for automated processing x-ray magnetic circular/linear dichroism spectromicroscopic data in live time.
- User support at the Surface/Interface (SIM) beamline at the Swiss Light Source (SLS).

2013 - 2015 **MSc in Nanoscience, University of Basel, CH**

- Master thesis: 'Open loop Kelvin probe force microscopy on low density polyethylene surfaces'.
- Included stay at the Center of Nanophase Materials Sciences (CNMS) at the Oak Ridge National Laboratory (ORNL) in Oak Ridge, Tennessee, US.
- Invited talk at ABB Corporate Research, Dättwil, CH
- Methods used: atomic force microscopy, band excitation Kelvin probe force microscopy, Comsol Multiphysics.

2008 - 2012 **BSc in Nanoscience, University of Basel, CH**

- In the last year various practical classes including experiments performed with atomic force microscopy, scanning electron microscopy, scanning electron microscopy, Raman spectroscopy etc.